

CHARACTERIZING DRYLAND ECOSYSTEMS USING REMOTE SENSING AND
DYNAMIC GLOBAL VEGETATION MODELING

by

Abdolhamid Dashtiahangar



A dissertation

submitted in partial fulfillment

of the requirements for the degree of

Doctor of Philosophy in Geosciences

Boise State University

December 2019

© 2019

Abdolhamid Dashtiahangar

ALL RIGHTS RESERVED

BOISE STATE UNIVERSITY GRADUATE COLLEGE

DEFENSE COMMITTEE AND FINAL READING APPROVALS

of the dissertation submitted by

Abdolhamid Dashtiahangar

Dissertation Title: Characterizing dryland ecosystems using remote sensing and dynamic global vegetation modeling

Date of Final Oral Examination: 03 October 2019

The following individuals read and discussed the dissertation submitted by student Abdolhamid Dashtiahangar, and they evaluated his presentation and response to questions during the final oral examination. They found that the student passed the final oral examination.

Nancy F Glenn, Ph.D.	Chair, Supervisory Committee
Alejandro Flores, Ph.D.	Member, Supervisory Committee
Marie-Anne de Graaff, Ph.D.	Member, Supervisory Committee
Susan Ustin, Ph.D.	Member, Supervisory Committee

The final reading approval of the dissertation was granted by Nancy F Glenn, Ph.D., Chair of the Supervisory Committee. The dissertation was approved by the Graduate College.

DEDICATION

To my wonderful family

ACKNOWLEDGEMENTS

I would like to express my sincere gratitude and enormous appreciation to my advisor Dr. Nancy F Glenn for all her support, generosity and time in guiding me throughout this journey.

I would also like to thank my dissertation committee: Dr. Alejandro Flores, Dr. Susan Ustin and Dr. Marie-Anne de Graaff for all their support, constructive discussions and feedback during my PhD program and my dissertation.

I would like to thank all funding agencies for their generous support: NASA Terrestrial Ecology program (NASA TE; grant number NNX14AD81G), Department of the Interior Northwest Climate Adaptation Science Center graduate fellowship, US Forest Service Western Wildlands Environmental Threat Assessment Center (WWETAC) to Boise State University through Joint Venture Agreement (17-JV-11221633-130), and the Joint Fire Science Program Project ID: 15-1-03-23.

I would like to thank all BCAL group members for their friendly support, generosity and kindness.

I would like to thank Boise State Research Computing for their help with running different programs used in this study on cluster.

Finally, I wish to thank my Mom, Dad, Siblings and my lovely nephew, Salman, for their support during my PhD.

ABSTRACT

Drylands include all terrestrial regions where the production of crops, forage, wood and other ecosystem services are limited by water. These ecosystems cover approximately 40% of the earth terrestrial surface and accommodate more than 2 billion people (Millennium Ecosystem Assessment, 2005). Moreover, the interannual variability of the global carbon budget is strongly regulated by vegetation dynamics in drylands. Understanding the dynamics of such ecosystems is significant for assessing the potential for and impacts of natural or anthropogenic disturbances and mitigation planning, and a necessary step toward enhancing the economic and social well-being of dryland communities in a sustainable manner (Global Drylands: A UN system-wide response, 2011). In this research, a combination of remote sensing, field data collection, and ecosystem modeling were used to establish an integrated framework for semi-arid ecosystems dynamics monitoring.

Foliar nitrogen (N) plays an important role in vegetation processes such as photosynthesis and there is wide interest in retrieving this variable from hyperspectral remote sensing data. In this study, I used the theory of canopy spectral invariants (AKA p-theory) to understand the role of canopy structure and soil in the retrieval of foliar N from hyperspectral data and machine learning techniques. The results of this study showed the inconsistencies among different machine learning techniques used for estimating N. Using p-theory, I demonstrated that soil can contribute up to 95% to the total radiation budget of the canopy. I suggested an alternative approach to study photosynthesis is the use of

dynamic global vegetation models (DGVMs). Gross primary production (GPP) is the apparent ecosystem scale photosynthesis that can be estimated using DGVMs. In this study, I performed a thorough sensitivity analysis and calibrated the Ecosystem Demography (EDv2.2) model along an elevation gradient in a dryland study area. I investigated the GPP capacity and activity by comparing the EDv2.2 GPP with flux towers and remote sensing products. The overall results showed that EDv2.2 performed well in capturing GPP capacity and its long term trend at lower elevation sites within the study area; whereas the model performed worse at higher elevations likely due to the change in vegetation community. I discussed that adding more heterogeneity and modifying ecosystem processes such as phenology and plant hydraulics in ED.v2.2 will improve its application to higher elevation ecosystems where there is more vegetation production. And finally, I developed an integrated hyperspectral-lidar framework for regional mapping of xeric and mesic vegetation in the study area. I showed that by considering spectral shape and magnitude, canopy structure and landscape features (riparian zone), we can develop a straightforward algorithm for vegetation mapping in drylands. This framework is simple, easy to interpret and consistent with our ecological understanding of vegetation distribution in drylands over large areas. Collectively, the results I present in this dissertation demonstrate the potential for advanced remote sensing and modeling to help us better understand ecosystem processes in drylands.

TABLE OF CONTENTS

DEDICATION	iv
ACKNOWLEDGEMENTS	v
ABSTRACT	vi
LIST OF TABLES	xi
LIST OF FIGURES	xii
CHAPTER ONE: INTRODUCTION	1
CHAPTER TWO: EMPIRICAL METHODS FOR REMOTE SENSING OF CANOPY NITROGEN MAY LEAD TO UNRELIABLE INTERPRETATION OF ECOSYSTEM FUNCTION	5
Abstract	5
Introduction	6
Materials and methods	9
Results and discussion.....	15
Variable selection is sensitive to transformation and scale	15
Cross-validation is overoptimistic.....	21
Canopy structure and soil dominate the total canopy reflectance.....	23
Correlation and causation and the concept of counterfactual	27
Conclusion.....	30
CHAPTER THREE: PERFORMANCE OF ECOSYSTEM DEMOGRAPHY MODEL (EDv2.2) IN SIMULATING PHOTOSYNTHESIS CAPACITY AND ACTIVITY ALONG AN ELEVATION GRADIENT IN A DRYLANDS STUDY AREA	34

Abstract	34
Introduction	35
Material and methods.....	38
Study area and data.....	38
Ecosystem Demography model.....	41
Sensitivity analysis and model calibration.....	41
Evaluating GPP capacity and activity	44
Results	45
Discussion.....	50
Sensitivity analysis	50
GPP capacity	52
GPP activity	54
Conclusion.....	56
CHAPTER FOUR: REGIONAL SCALE DRYLAND VEGETATION CLASSIFICATION WITH AND INTEGRATED LIDAR HYPERSPCTERAL APPROACH	58
Abstract	58
Introduction	59
Materials and methods	65
Methods	68
Results	73
Classification.....	73
Discussion.....	76
Xeric classification	76

Mesic classification	77
Conclusion.....	81
CHAPTER FIVE: CONCLUSION	83
REFERENCES.....	88
APPENDIX A	120
Supplementary information for chapter 2	120
SI Text 1. Data collection	121
Additional data sets	135

LIST OF TABLES

Table 2.1	Empirical estimation of canopy N for shrubs corrected for the impact of soil and canopy structure.	29
Table 3.1.	Site descriptions of the three eddy covariance sites, WBS, LS, MBS.	40
Table 3.2.	PFT parameters within EDv2.2, their abbreviation, and initial, lower and upper boundaries selected for the Morris sensitivity analysis.	43
Table 3.3.	PEST++ results for SLA, STO_S, CUT_C, and VM0 and their uncertainty.....	47
Table 3.4.	Calibration and validation results for EDv2.2 for WBS and LS sites.	47
Table 4.1.	The number of ground validation points (represented by 1 m pixels) used for endmember (EM) derivation and classification accuracy assessment per class.....	70
Table 4.2	User's and producer's accuracy for multiple endmember spectral mixture analysis (MESMA) classification.....	74
Table 4.3	Confusion matrix for spectral angle mapper (SAM) results alone and with lidar-derived information.	75
Table S1.	Summary of field data statistics.	129
Table S2.	Comparison of selected bands using Ensemble method and known N absorption bands.....	130
Table S3.	Prediction rate for foliar N at different scales using cross validation.	131
Table S4.	Prediction rate for LAI at different scales using cross validation.	132
Table S5.	Cross validation vs leave-one-dataset-out validation.	134

LIST OF FIGURES

Figure. 2.1	Performance of different empirical models on an ideal synthetic dataset. 16
Figure. 2.2	Variable selection using different methods at the leaf scale for four different spectral transformations for nitrogen estimation.18
Figure. 2.3	Scaling up band selection for N from leaf (left) to canopy (middle) and plot (right). Data are shown for log transformation.19
Figure. 2.4	Variable selection for LAI and N at canopy (top) and plot (bottom) scales (data shown for log transformation).21
Figure. 2.5	Spectral invariant parameters at canopy (left) and plot (right) scales.24
Figure. 2.6	Comparison of simulations between a dry shrub (left) located in California and green shrub (right) located in Idaho.25
Figure. 2.7	Simulation of different components of total reflectance of canopy (left) and plot (right) samples.26
Figure. 2.8	Relationship between DASF and BRDF in the NIR region.26
Figure. 2.9	Canopy scattering correction for soil and canopy structure.27
Figure 3.1.	Location of EC towers in Reynolds Creek Experimental Watershed, Idaho.40
Figure 3.2.	Sensitivity analysis based on Morris for WBS, LS, and MBS, μ^* and σ are the mean and standard deviation. At all three sites, SLA, STO_S, CUT_C, and VM0 are identified based on this analysis as the most important parameters to estimate GPP.46
Figure 3.3.	Model simulations vs. tower observation for WBS.48
Figure 3.4.	Phenometrics estimated from MODIS GPP and simulated GPP using EDv2.2.48
Figure 3.5.	One-to-one plot between SOS and EOS estimated from MODIS and EDv2.2 GPP for WBS site (2000-2017).49

Figure 3.6.	Estimated seasonal and trend components for MODIS (top row) and EDv2.2 GPP (bottom row) for years 2000-2017.....	50
Figure 3.7.	Precipitation seasonal and trend components and their confidence interval for WBS site (2000-2017). The precipitation data comes from WRF model.	50
Figure 3.8.	Contribution of shrub and grass PFTs in total GPP for WS site.....	54
Figure 4.1	Elevation range and location of plots at Reynolds Creek Experimental Watershed, Idaho, U.S.....	66
Figure 4.2	The classification framework using both hyperspectral and lidar data.	69
Figure 4.3	(a) Canopy maximum height distribution extracted from lidar and (b) probability density function for aspen and riparian classes.....	72
Figure 4.4	Distribution of xeric percent cover over the region.	75
Figure 4.5	Final vegetation cover map of RCEW using SAM, MESMA, and lidar-derived products; (left) mesic classes and (right) xeric classes.	76
Figure S1.	Study area, the Great Basin.....	125
Figure S2.	Mean spectra of the dry leaves, canopy and plot-level measurements, and soil.	126
Figure S3.	Variable selection for N at leaf (first row), canopy (second row) and plot (third row) scales.....	127
Figure S4.	Variable selection for LAI at canopy (first row) and plot (second row) scales.....	128
Figure	S5. Cross validated predictions before (left column) and after (right column) correction for canopy structure and soil.....	133

CHAPTER ONE: INTRODUCTION

Dryland ecosystems serve important carbon cycling functions and provide a host of ecosystem services across the globe. Human activities such as land use/landcover change have led to substantial changes in semi-arid ecosystems (Gao et al., 2010; Georgescu et al., 2009; Huang et al., 2016; Scanlon et al., 2006). These fragile ecosystems are prone to the ecological disturbances that are within the range of conditions naturally experienced by the ecosystem (e.g. fire, extreme climatic events), as well as stressors from anthropogenic origins (e.g. fire regime alteration, land use change). Moreover, semi-arid ecosystems serve important roles in regulating the global carbon cycle. New evidence shows that at a global scale, the land carbon uptake interannual variability strongly linked to vegetation dynamics in semi-arid ecosystems (Ahlström et al., 2015; Poulter et al., 2014; Smith et al., 2018). Thus, one might conclude that monitoring the status of semi-arid ecosystems is fundamental to address the interactions that links biotic systems, of which people are an integral part, with the physical system on which they depend. Throughout the dissertation, I refer to semi-arid ecosystems interchangeable as drylands and sometimes shrublands. In fact, semi-arid ecosystems is one of several dryland ecosystem types (Kottek et al., 2006).

Remote sensing and process-based modeling are two common tools for ecosystem studies. As it is highlighted in (Schimel et al., 2019), satellite vegetation measurements are central in many ecosystem ecology studies. Recent advances in optical (400 – 2500 nm) sensors such as high spectral (i.e. hyperspectral) and spatial resolutions enable scientists to go beyond using vegetation greenness for analysis and retrieve a wide range of ecosystem

characteristics. Upcoming imaging spectroscopy sensors that are satellite-based (e.g., PRISMA (recently launched), EnMAP, SBG, and CHIME) or currently or planned to be on the International Space Station (ISS) (e.g., DESIS, HISUI, and EMIT) will provide an unprecedented amount of data for ecosystem monitoring. Moreover, other remote sensing sources such Light Detection and Ranging (lidar) provides additional information that can improve our understanding of vegetation in drylands. Complementary to remote sensing, Dynamic Global Vegetation Models (DGVMs) represent vegetation processes at individual scales (e.g. photosynthesis) and ecosystem scales (e.g. competition). These models also incorporate other forcing processes such as anthropogenic (e.g. land use, land cover change) and natural disturbances (e.g. wildfire). These models are great tools for understanding ecosystem processes and making forecasts which may ultimately help facilitate the process of decision making and ecosystem management.

There are challenges associated with the application of both optical remote sensing and DGVMs in semi-arid ecosystems. First, semi-arid vegetation is heterogeneous. For example, within a pixel or an eddy covariance flux tower (EC towers) footprint, there may be multiple plant functional types (PFTs) such as shrub, grass and tree and non-vegetative components including soil and litter which collectively contribute to the signal recorded by remote sensing sensors or EC towers. Secondly, vegetation cover is typically sparse and canopy structure can be short with a significant amount of woody compared to green biomass. This is particularly important in remote sensing applications because a low amount of leaves can result in a larger contribution of the understory to the total radiation budget. Moreover, there is a decoupling between vegetation greenness and its optical properties in drylands. For example, water stress forces stomatal closure in plants due to

plant hydraulics (Novick et al., 2016) while vegetation greenness remains almost constant during this period (Smith et al., 2019). Thus, while environmental stressors (e.g. water stress) may change the function of plants, detecting plant function using remote sensing data (based on greenness) can be challenging. And, finally, changes in environmental conditions lead to rapid changes in vegetation structure and composition. For example we can observe rapid changes in vegetation function such as gross primary production (GPP) due to precipitation and temperature changes along an elevation gradient.

The main goals of this study are to further advance the use of remote sensing and DGVMs in semi-arid ecosystems. The main research questions I address are: **1) What is the role of confounding factors in empirical estimation of canopy nitrogen content from hyperspectral data? 2) How does the Ecosystem Demography (ED.v.2.2) model perform in simulating GPP along an elevation gradient? and 3) What is the accuracy of vegetation classification using an integrated hyperspectral-lidar framework?** These questions are addressed in subsequent chapters of the dissertation.

Canopy N is one of the most important elements in enzymes such as Rubisco, amino acids, and chlorophyll, and is a key factor in photosynthesis and the terrestrial carbon cycle (Bonan, 2019; Schimel et al., 2019). I discuss the retrieval of N from hyperspectral remote sensing in shrublands in chapter 2. Specifically, we focus on the effects of confounding factors such as soil and canopy structure on the accuracy and stability of N retrieval using machine learning techniques. In chapter 3 I investigate the capability of the ED.v.2 demographic model in simulating GPP along a sharp elevation gradient. I use a Parameter Estimation and Uncertainty Analysis (PEST++) to a perform sensitivity analysis and calibration of ED.v.2.2. The model simulation is compared with data collected from eddy

covariance flux towers and remote sensing products. In chapter 4 I present a framework for integrated hyperspectral-lidar vegetation classification including mesic and xeric vegetation classes. And finally, in chapter 5, I discuss the contribution of this dissertation in studying vegetation in drylands and possible directions for future studies.

CHAPTER TWO: EMPIRICAL METHODS FOR REMOTE SENSING OF CANOPY
NITROGEN MAY LEAD TO UNRELIABLE INTERPRETATION OF ECOSYSTEM
FUNCTION

This chapter has been published as:

**H. Dashti, N. F. Glenn, S. Ustin, J. J. Mitchell, Y. Qi, N. T. Ilangakoon, A. N. Flores,
J. L. Silván-Cárdenas, K. Zhao, L. P. Spaete, and M. de Graaff, “Empirical
Methods for Remote Sensing of Nitrogen in Drylands May Lead to
Unreliable Interpretation of Ecosystem Function,” *IEEE Trans. Geosci.
Remote Sens.*, pp. 1–12, 2019.**

Abstract

Nitrogen (N) has been linked to different ecosystem processes, and retrieving this important foliar biochemical constituent from remote sensing observations is of widespread interest. Since N is not explicitly represented in physically based radiative transfer models, empirical methods have been used as an alternative. The spectral bands selected during the calibration of empirical methods have been interpreted in the context of light-N interactions and consequently, ecosystem function. The low amount of leaves on shrubs and their sparse distribution in drylands create an environment in which canopy structure and the bright background soil play an important role in the canopy total radiation budget. In this study, we examine the assumption that removing the impact of canopy structure and soil will result in improved N retrieval using empirical methods. We report inconsistencies in the selection of spectral bands among the empirical approaches.

Moreover, these methods are sensitive to the scale of the study and band transformations. Using the generalized theory of canopy spectral invariants, we found that at the canopy scale a combination of canopy structure and soil dominate the total canopy radiation. At the plot scale, soil contributes up to 95% of the total reflectance. Correction for these two confounding factors leads to no correlation between N and vegetation reflectance at both scales. We conclude that while cross-validated predictive models may be statistically achievable, caution should be taken when interpreting their results in the context of N-light interactions and ecosystem function. Our approach can be extended to all terrestrial ecosystems with multiple layers of canopy and understory.

Introduction

Terrestrial ecosystem processes have been interpreted from remote sensing estimates of foliar nitrogen and other leaf biochemicals. Canopy N has been related to forest albedo and linked to climate change (Ollinger et al., 2008), nutrient limitation (Asner et al., 2015a), Amazonian functional biodiversity (Asner et al., 2014), and the role of the plant community in controlling canopy biochemistry (Dahlin et al., 2013).

There are two general approaches for remote sensing of canopy chemistry: physical methods based on the concept of radiative transfer models (RTMs) and empirical/statistical methods based on regression analysis. A combination of these two approaches, known as hybrid methods, can also be used (Liang, 2003). Since there are no reliable RTMs that include leaf N, this foliar variable is mostly identified by empirical methods. Acceptable estimates of N have been reported using a range of empirical methods (average R^2 and RMSE of 0.72 and ± 0.16 , respectively, (Homolová et al., 2013a)). These include multiple linear regression (Feng et al., 2014; Pacheco-Labrador et al., 2014), partial least squares

(PLS) regression (Feng et al., 2014; Lepine et al., 2016; Mitchell et al., 2012; Ramoelo et al., 2012), stepwise multiple linear (SML) regression (Miphokasap et al., 2012) and more recently popular methods such as neural networks (Huang et al., 2004; Kalacska et al., 2015), support vector machines (SVM) (Karimi et al., 2006; Sun et al., 2017), Bayesian regression (BR) (Zhao et al., 2013) and Random Forest (RF) (X. Li et al., 2014).

The goal of statistical analysis is to fit a model between N and the feature space (i.e., spectral bands) or a transformation of the feature space. The developed model is then tested for its predictive power using cross-validation. The most influential variables on the model fit are then discussed in the context of light-N interactions. There are three issues related to this type of study. First, it is known that multiple chemical, physical and structural properties of vegetation and background soil control the spectral signal received at leaf, canopy and plot scales. In many cases, such as in sparse vegetation cover, N does not dominate the spectra (Asner, 1998; Asner et al., 2000). Ideal empirical studies usually include relevant predictor and response variables. It is thus essential to consider whether empirical relationships between reflectance spectra and N are suitable. Another consideration is that there is limited consistency between empirical studies in the selected bands for N prediction (Grossman et al., 1996; Homolová et al., 2013a). More importantly, in some cases, the selected bands are not consistent with the concepts of radiative transfer of N absorption, but rather driven by canopy structure or other factors that may or may not covary with N. For example, in dense forests with the assumption of a zero canopy background contribution (i.e. black soil) to the total canopy bidirectional reflectance factor (BRF), it has been shown that canopy structure derives positive correlation between the near-infrared (NIR, 800-850 nm) and N (Yuri Knyazikhin et al., 2013c). In fact, multiple

studies have identified NIR as important predictors of N (Martin et al., 2008; Ollinger et al., 2008; Wang et al., 2016). Finally, further investigation of the generalizability of empirical studies with cross-validation is needed. The number of successful N retrieval studies using statistical methods has been used as affirmation for the replicability of these models (Townsend et al., 2013). There is an urgent need to examine the interpretability of empirical methods and their fundamental meaning to the remote sensing and ecology community.

One way to study the interpretation of empirical methods is to investigate their link to underlying light-canopy physical processes. Knyazikhin (Yuri Knyazikhin et al., 2013c) used the theory of spectral invariants (Huang et al., 2007), which is based on radiative transfer (Knyazikhin. et al., 1998), and introduced a directional area scattering factor (DASF) as a new measure of canopy structure. DASF, in concept, is an estimate of the ratio of the leaf area that forms the canopy boundary, as seen along a given direction, to the total leaf area. Normalization of BRF to DASF results in canopy scattering coefficients (W) which are insensitive to canopy structure. In contrast to empirical findings, W exhibits either negative or no correlation with N (Yuri Knyazikhin et al., 2013c; Latorre-Carmona et al., 2014). A complicating factor is that while the DASF approach assumes a black soil background, in many ecosystems this assumption is violated and indeed impacts of soil can be larger than those from the canopy structure itself.

While empirical methods are widely used for canopy N retrieval, comprehensive studies linking these results to physical processes such as canopy radiative transfer are lacking. Our goal is to examine empirical methods used for more than two decades in the remote sensing community to answer the fundamental question of whether we can rely on

these methods to predict N in the context of the confounding factors of canopy structure and soil. Our null hypothesis is that correcting for confounding factors will improve N predictions using empirical methods. To test our hypothesis, we implement a range of empirical models and physical analyses based on the generalized theory of canopy spectral invariants (Yuri Knyazikhin et al., 2013c; Silván-Cárdenas and Corona-Romero, 2017). Our study advances the community discussion of light-N interactions beyond dense forests to include ecosystems with multiple layers of canopy and understory.

Materials and methods

Five sites were selected across the western US in the semi-arid ecosystem known as the Great Basin (GB) for the field study and data collection (Figure. S1). The Reynolds Creek Experimental Watershed (RCEW), Birds of Prey (BoP) and Hollister sites are located in Idaho and the Big Pine (BP) and Lone Pine (LP) sites are located in California on the eastern side of the Sierra Mountains. The dominant vegetation cover in the GB is sparsely distributed shrubs. These dryland study sites provide the opportunity to study the impact of canopy structure and soil on remote sensing of N, and extend previous work in dense forests to xeric ecosystems. Most of the ecosystems follow the same pattern in which an understory layer (e.g. soil, grass etc.) contribute to the total pixel radiation budget. Field data sampling was conducted during 2014 and 2015 (Table S1 and dataset S1). Considering the dominance of sagebrush (*Artemisia tridentata*) and bitterbrush (*Purshia tridentata*) in the study sites, plots were selected based on the dominant cover of one of these two species. We define three scales for the study: at the leaf scale the spectra were collected from dry leaves, at canopy scale, the spectrometer was held above the top of the canopy, and at plot scale (10 m × 10 m), the spectra are acquired from the AVIRIS-NG (dataset S2) airborne

hyperspectral sensor. An extended version of data collection can be found in supplementary information (SI; Text1). Four different types of spectral transformations were applied to the spectra, the smoothed dataset using the Savitzky-Golay filter (Savitzky and Golay, 1964) with a frame size of 11, and second-degree polynomial, logarithmic transformation, first derivative of smoothed dataset and logarithm of the first derivative. These transformations are widely used in remote sensing of canopy chemistry and are known to enhance the absorption features (Axelsson et al., 2013; Curran et al., 2001; Xinchuan Li et al., 2014). For the statistical analysis we implemented PLS (Wold et al., 2001), SVM (Smola and Schölkopf, 2004), RF (Breiman, 2001), and BR regression (Zhao et al., 2013) methods and a newly developed multi-method ensemble variable selection based on the integration of PLS, SVM and RF (Feilhauer et al., 2015). In this Ensemble approach, a spectral band is important if it is identified as important by all three methods. Each method returns band importance which will be weighted by the explained variance of selected model for each method according to equation 1:

$$I_{iw} = (I_i * R^2) / \sigma_I \quad (1)$$

Where I_{iw} is the weighted importance of band i , I_i is the raw measure of the band importance of the regression method and R^2 is the explained variance of the model in cross-validation or out-of-the-bag testing and σ_I is the standard deviation across the raw measures of importance of each model. The product of the three weighted importance values is considered as Ensemble importance. As a base method, we calculate the variable importance in projection (VIP) by developing 1000 PLS models (Feilhauer et al., 2015), (Singh et al., 2015). VIP is the most common approach for variable selection based on PLS outputs. In our approach, a band was considered important when its average VIP value

along with one standard deviation (derived from 1000 iterations) was above one. We refer to the mean of the 1000 PLS models as the PLS_{Ref} model. The reported R² and coefficient of variation (CV) for PLS_{ref} is the mean of all 1000 model runs. K-fold cross-validation and also leave-one-dataset-out validation has been used to assess the model's performance. In the leave-one-dataset-out approach a complete dataset that has been collected in a given year and site was kept out of calibration step. A synthetic dataset was created to test the performance of all methods in an ideal case. This dataset contained 200 observations with 500 correlated predictors. Ten of the predictors were set to have a coefficient value of one (i.e., relevant predictors), and all other predictors are zero (unrelated predictors). A complete description of a similar dataset construction is presented in (Zhao et al., 2013). The purpose of the statistical analysis is not to test a comprehensive list of the algorithms but to implement the most common ones.

The physical analysis is based on the theory of canopy spectral invariants. According to this theory, under the assumption of black soil, canopy scattering $s(\lambda)$ and absorption $a(\lambda)$ are expressed in equations 2 and 3:

$$s(\lambda) = \frac{(1-p)\omega_l(\lambda)}{1-p\omega_l(\lambda)} i_0 \quad (2)$$

$$a(\lambda) = \frac{1-\omega_l(\lambda)}{1-p\omega_l(\lambda)} i_0 \quad (3)$$

Where i_0 is the probability of canopy interception, ω_l is the single scattering albedo of an average phytoelement at any wavelength and p is the recollision probability (Smolander and Stenberg, 2005). The recollision probability can be interpreted as the probability that a photon interacted with canopy elements will interact within the canopy again (Vanhatalo et al., 2014). This theory can be generalized to the situation with multiple endmembers and the interaction between photons and endmembers can be treated as an

infinite-state Markov chain (Silván-Cárdenas and Corona-Romero, 2017). Then equations 2 and 3 have the form:

$$s(\lambda) = \mathbf{q}^T \mathbf{\Omega}(\lambda) \mathbf{i}(\lambda) \quad (4)$$

$$a(\lambda) = \alpha^T \mathbf{i}(\lambda) \quad (5)$$

Where $\mathbf{q} = (\mathbf{I} - \mathbf{P}_n) \mathbf{1}$ is the vector of escape probability after n interactions, $\mathbf{\Omega}(\lambda) = \mathbf{diag}[\omega_1(\lambda) \dots \omega_m(\lambda)]$ is a diagonal matrix of single scattering albedo associated with endmembers and $\alpha(\lambda) = (\mathbf{I} - \mathbf{\Omega}(\lambda)) \mathbf{1}$ is the vector of the endmember's absorptance. The quantity \mathbf{q} defines the probability that a photon scattered by phytoelements will escape vegetation toward a given direction (Knyazikhin et al., 2011). This generalization includes both photons from the canopy endmembers r_c and background endmembers r_B or $s = r_c + r_B$. Furthermore, based on the principle of energy conservation, we can calculate the canopy radiation budget (CRB) and quantify canopy and surface contribution to the CRB. We assume there are two layers consisting of a canopy layer on top of a flat soil layer. The solution of CRB with reflective surface is built by integrating the black soil solution (BS) problem, which soil impact is negligible and the second solution where soil is considered as the source of illumination (S problem). Then CRB can be expressed in equations 6 to 8:

$$r_c(\lambda) = r_{BS}(\lambda) + \frac{\rho_s(\lambda)t_{BS}(\lambda)}{1-\rho_s(\lambda)r_s(\lambda)} (t_s(\lambda) - q_s) \quad (6)$$

$$a_c(\lambda) = a_{BS}(\lambda) + \frac{\rho_s(\lambda)t_{BS}(\lambda)}{1-\rho_s(\lambda)r_s(\lambda)} a_s(\lambda) \quad (7)$$

$$t_c(\lambda) = t_{BS}(\lambda) + \frac{\rho_s(\lambda)t_{BS}(\lambda)}{1-\rho_s(\lambda)r_s(\lambda)} (r_s(\lambda) - p_{sl}) \quad (8)$$

Where r_c , a_c , t_c , ρ_s and q_s are canopy reflectance, canopy absorptance, canopy transmittance, soil reflectance, and photon escape probability from soil, respectively. The BS and S reflectance, absorptance and transmittance are defined in equation 9-14:

$$r_{BS}(\lambda) = \frac{q_l \omega_l(\lambda)}{1 - p_{\{LL\}} \omega_l(\lambda)} i_0 \quad (9)$$

$$a_{BS}(\lambda) = \frac{1 - \omega_l(\lambda)}{1 - p_{\{LL\}} \omega_l(\lambda)} i_0 \quad (10)$$

$$t_{BS}(\lambda) = t_0 + \frac{p_{\{LS\}} - \omega_l(\lambda)}{1 - p_{\{LL\}} \omega_l(\lambda)} i_0 \quad (11)$$

And

$$r_s = \frac{(t_{BS} - t_0) p_{\{SL\}}}{i_0} \quad (12)$$

$$a_s = \frac{a_{BS} p_{\{SL\}}}{i_0} \quad (13)$$

$$t_s = \frac{r_{BS} p_{\{SL\}}}{i_0} + q_s \quad (14)$$

Where q_l , i_0 and t_0 are canopy escape probability and canopy interceptance and uncollided transmittance of the BS problem, respectively. $p_{\{LL\}}$, $p_{\{LS\}}$ and $p_{\{SL\}}$ and $p_{\{SS\}}$ are the leaf-leaf, leaf-soil, soil-leaf and soil-soil recollision probabilities. The second term in Equation 6 accounts for the influence of soil to the CRB. Photons that escape directly from the surface are not part of the canopy reflectance even if they interact with canopy before reaching the surface. Subtracting these term from r_c , leave us with r_{BS} which has the form noted in Equation 9. Not surprisingly, the r_{BS} is similar to the model developed for the black soil problem (Equation 2, (Smolander and Stenberg, 2005)) with recollision probability $p = p_{\{LL\}}$. Thus, one should note that the contribution of soil to the total reflectance is the sum of the photons that escape from soil (r_B) and reach the sensor and the portion of photons that escape from soil and influence the canopy reflectance (r_c). We refer to the first component as soil contribution to the total reflectance and second component as the soil contribution to the reflectance of CRB. A complete derivation and description of the terms in Equations 4-14 are provided in (Silván-Cárdenas and Corona-Romero, 2017; Silván-Cárdenas and Wang, 2010). With the assumption that soil is flat (no interaction between soil endmembers) $p_{\{SS\}}$ is much lower than the other recollision

probabilities and can be neglected ($p_{\{SS\}} = 0$). In order to estimate $p_{\{LL\}}$, $p_{\{LS\}}$, $p_{\{SL\}}$ and i_0 , we fit the spectra at each scale to Equation 4 using the covariance matrix adaptation evolution strategy (CMAES) optimization approach (Hansen, 2016). The mean RMSE between simulated and measured total canopy spectra at the canopy scale is 0.01 and at the plot scale is 0.02. CMAES is a state-of-the-art evolutionary algorithm developed for non-linear, non-convex black-box optimization problems. We added 4% Gaussian noise to the spectrums and performed inversion. Our preliminary analysis (not shown) using 100 different random initial points and a noisy objective function showed that CMAES is not sensitive to the initial points or noise and consistently returns the global minima. Using the recollision probabilities and equations 6-8, CRB was calculated. The r_{BS} was used for the retrieval of DASF. The DASF was calculated using the algorithm developed by (Yuri Knyazikhin et al., 2013c), the only modification was, instead of using a reference leaf albedo we used measured green leaf reflectance of sagebrush and bitterbrush (Roberts et al., 1998). In order to calculate leaf albedo, leaf transmittance was acquired by inversion of PROSPECT-5 leaf model (Ferret et al., 2008) using the measured leaves reflectance. In summary the steps of our physical analysis is as follows:

- Fit the spectrum to Equation 4 to estimate recollision probabilities.
- Use estimated recollision probabilities to calculate r_{BS} using Equations 6-14.
- Use r_{BS} to calculate DASF and calculate canopy scattering.
- Canopy scattering is then used for statistical analysis.

Results and discussion

Variable selection is sensitive to transformation and scale

Using an ideal dataset (materials and method), Figure. 2.1 shows the performance of an Ensemble model and its sub-models (PLS, SVM, RF), variable importance in projection (VIP) and Bayesian regression variable selection techniques. We start by discussing the VIP results. Between methods, VIP performs the worst in variable selection by identifying numerous unrelated bands as important. In cases where there is high co-variation between variables (e.g., spectral bands) but small correlation to the target (e.g., N), the standardization used by PLS can address the latter, but at the cost of increasing the weight of minor variables with low signal-to-noise ratios (Kvalheim et al., 2014). This directly impacts the VIP as it is a filter method and uses the PLS output with no further post-processing. This behavior can also be seen at the leaf scale (Figure. 2.2), though to a lesser degree than the canopy and plot scales. Our first observation shows that the VIP is sensitive to the type of transformation. Across all transformations, the VIP identified the NIR region (~800-1350 nm) as important predictors of leaf N. This is controversial since most of the incident radiation is reflected and transmitted (~ 50% each) in the NIR region by the leaf mesophyll (Walter-Shea and J. M. Norsman, 1991) and it is extremely difficult to identify weak N absorption bands (e.g., 910 and 1020 nm; (Curran, 1989)) using variable selection techniques. While many hyperspectral studies use VIP for band selection (Castaldi et al., 2016; Herrmann et al., 2011; Xinchuan Li et al., 2014) and specifically in foliar N estimation (Ewald et al., 2018a; Lepine et al., 2016; Pellissier et al., 2015; Wang et al., 2016), the selection of unrelated bands may require further examination of VIP.

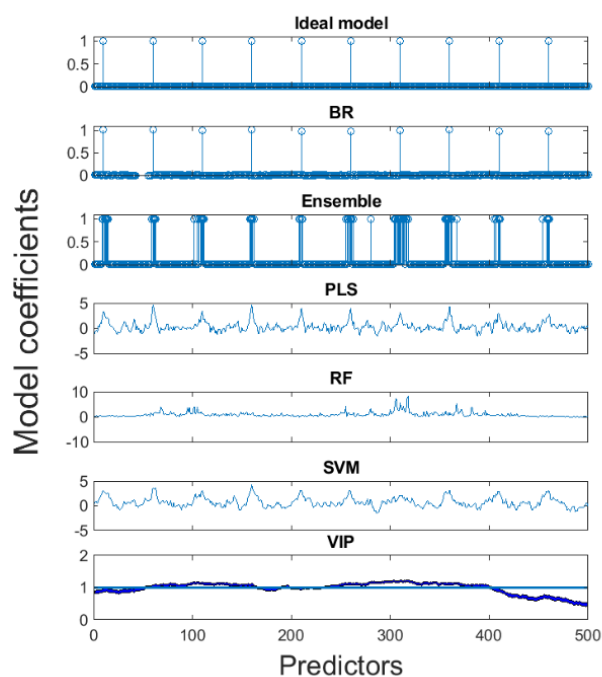


Figure. 2.1 Performance of different empirical models on an ideal synthetic dataset.

Figure. 2.1 shows that the BR produced the closest results to the ideal model for band selection, and the Ensemble approach follows with less ideal, but comparable results. In the Ensemble approach, a spectral band is important if it is considered important by all three regression methods (PLS, RF, and SVM). The peaks in the PLS match the coefficients of the ideal model, but PLS assigned weights to many unrelated variables. RF is more restrictive and consequently many unrelated bands are close to zero. This restrictive behavior, however, caused RF to miss some of the important variables. The SVM results are similar to PLS, which has been observed in other studies (Feilhauer et al., 2015). The improved performance of the BR and Ensemble methods can be attributed to the fact that both methods are ensembles of competing models. BR is based on Bayesian model averaging and has theoretical advantages over standard regression analysis (Zhao et al., 2013). The Ensemble method, on the other hand, uses the relative merits of PLS, SVM,

and RF. For example, the restrictive variable selection method of RF is balanced with the more inclusive PLS and SVM in the Ensemble approach.

When we used field data at the leaf scale, both the Ensemble and RF methods show less sensitivity to the transformations. However, the individual models of the Ensemble in isolation show sensitivity to the transformation. These transformations have been accepted as a standard preprocessing method for remote sensing of foliar biochemistry. Thus, two studies with the same dataset but different spectral transformation for predicting N can suggest different spectral bands as important predictors. At the leaf scale, our findings show that the log transformed dataset leads to more meaningful bands when compared with known N absorption regions (Table S2). If assuming the leaf reflectance spectrum has the same shape as leaf transmittance, then the log-transformation is an approximation of the foliar absorption spectra and is consistent with the Beer's law absorption coefficient (Dawson et al., 1999).

Using the log transformation and Ensemble approach for interpretation, most of the selected bands at the leaf scale are in the visible and mid-infrared (MIR; $1350 > \text{nm}$), with no bands selected in the NIR region. Selection of the visible spectrum can be attributed more explicitly to chlorophyll content (Ustin et al., 2009). Moderate correlation is reported between chlorophyll and N (Homolová et al., 2013b). In the shortwave infrared (SWIR) region identified bands centered near 1655, 1715, 1900 and 2200 nm can be attributed to N absorption at 1690, 1940, and 2240 nm. Among them the bands near 2240 and 2300 nm are more directly related to the N or proteins which carry N, while other bands can be associated with absorption by biochemicals such as lignin, cellulose, and starch. The complex interactions between N and these biochemicals may result in misinterpretation of

the selected bands and consequently unreliable statistical estimates of N. The Ensemble method is a VS method and does not provide predictions. Since the VS performance of BR and Ensemble are close, BR can be used for both variable selection and model fitting at the leaf scale. We conclude that at the leaf scale, with the assumption of no confounding factors, robust empirical methods such as BR are likely to provide a meaningful model for N predictions. However, it is important to choose the appropriate spectral transformation (e.g., logarithmic transformation), and results of the VS should be checked with known absorption regions.

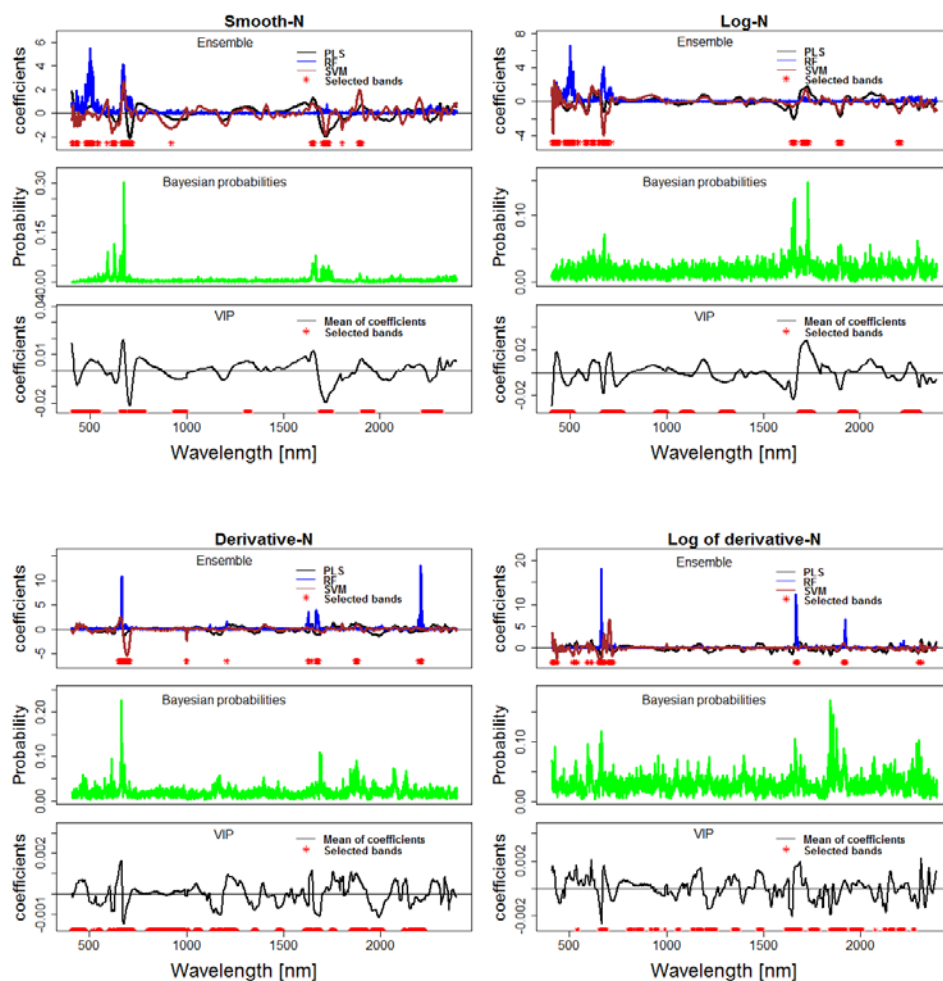


Figure. 2.2 Variable selection using different methods at the leaf scale for four different spectral transformations for nitrogen estimation.

Moving from the leaf to canopy and plot scales, the selected bands for N differ, regardless of the method used. Figure. 2.3 shows variable selection for the log transformed dataset. Other transformations can be found in Figure. S3. The fundamental assumption of empirical predictions is foliar N controls the reflectance (Disney, 2016; Verstraete et al., 1996) and thus we would expect consistency in the bands identified as important across scales. However, Figure. 2.3 indicates a lack of this consistency across scales. This is the first evidence that there are other elements that may have a more dominant role in controlling canopy radiation.

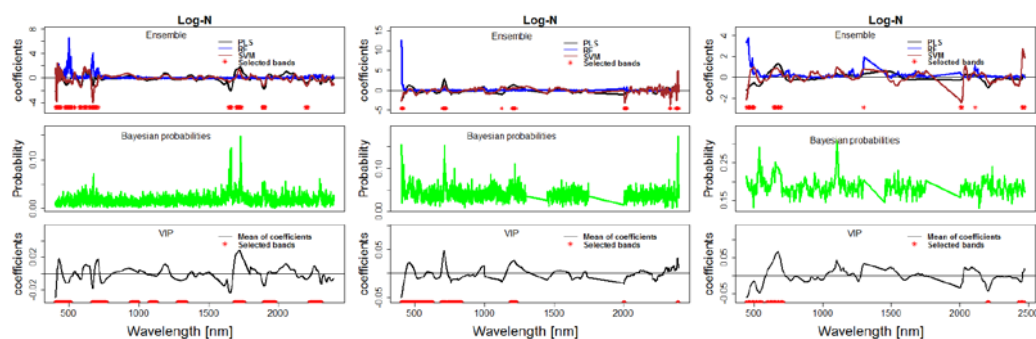


Figure. 2.3 Scaling up band selection for N from leaf (left) to canopy (middle) and plot (right). Data are shown for log transformation.

Using log transformed data and focusing on the Ensemble or BR methods, the spectral regions identified as important for N are similar to the regions identified as important for a similar analysis of leaf area index (LAI) at the canopy and plot scales (Figure. 2.4 and Figure. S4). Most of these bands lie in the red edge and NIR region. The NIR region in particular is known to be attributed to canopy structure (i.e., LAI). However, the predictive power of these bands for LAI is much less than N (Table S3 and S4). For example, the cross-validated mean R^2 and coefficient of variation (CV) of all methods for the log transformed prediction of N at the canopy scale are 0.61 and 16.67, respectively, while for LAI they are 0.26 and 35.39, respectively. It is tempting to discuss this in terms

of ecology and the association between canopy N and LAI, however it is more likely a statistical problem. An explanation is that statistically significant explanatory variables (e.g., spectral bands) that have an association with a target variable might not necessarily carry the most predictive power and the most predictive variables are not necessarily the most significant ones (Lo et al., 2016, 2015). A key distinction that makes a variable significant or predictive lies in the properties of their underlying distribution. This issue has been observed in different disciplines from genome-wide association studies (Gränsbo et al., 2013) for disease predictions to social studies predicting civil wars (Ward et al., 2010). Thus, the problem can be statistically framed by asking if the research goal is to find *highly significant* or *highly predictive* variables whereas searching for both significant and predictive variables can lead to conflicting directions (Lo et al., 2015). The notion of predictability and significance of variables has not been explored in remote sensing of canopy biochemistry. In the next section, we discuss the problem associated with cross-validation and demonstrate that these predictive variables for N lose their predictive power when applied to an external dataset, of which time or location are different from the calibration dataset.

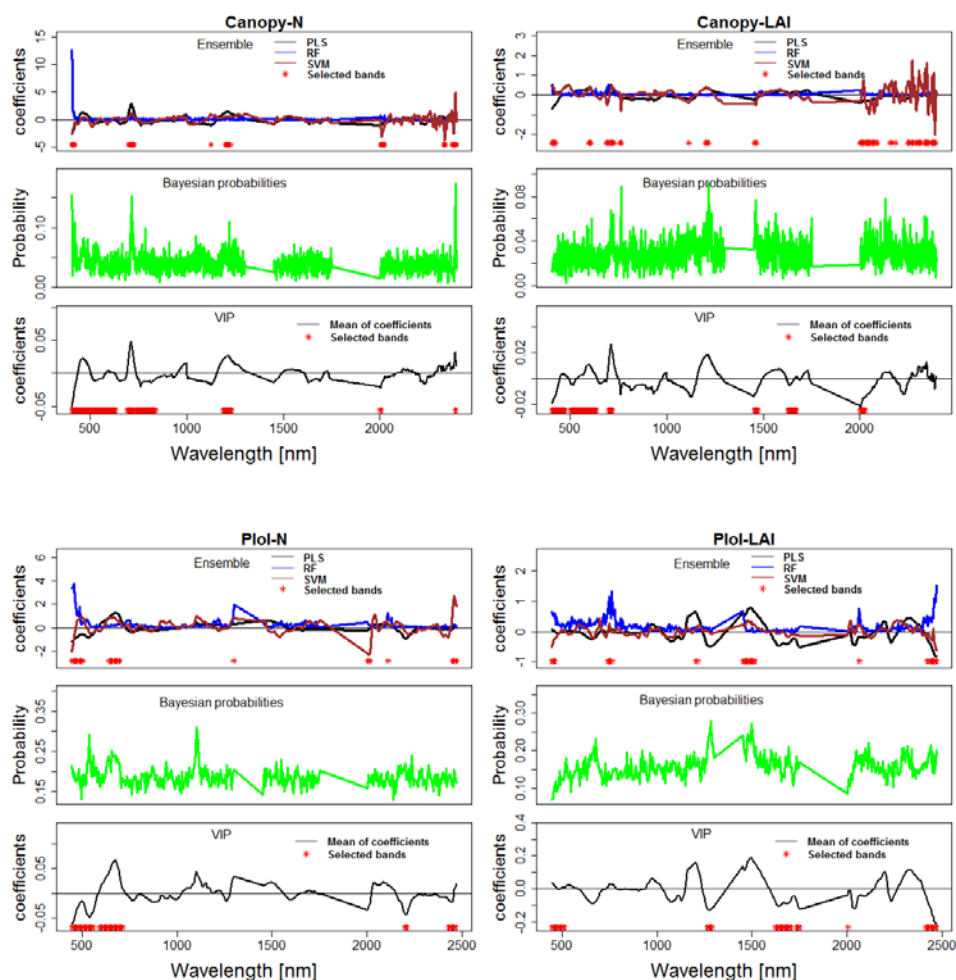


Figure. 2.4 Variable selection for LAI and N at canopy (top) and plot (bottom) scales (data shown for log transformation).

Cross-validation is overoptimistic

Generalization of a statistical method is a key concept and refers to applying a model based on a particular target population to other populations (Kenett and Shmueli, 2015). As discussed in the classical paper by Verstraete et al. (1996) (Verstraete et al., 1996), “a relation obtained by statistically correlating remote sensing measurements and field observations, is *useful* only for those locations and times other than those used to establish the correlation.” Otherwise, remote sensing provides no new information. Cross-validation is accepted as the *de facto* standard method used in remote sensing communities

to test for the generalization of the developed model. Table S5 shows results for normal cross-validation vs. validation results for the dataset that was kept out of calibration (Materials and Methods). The datasets are different in either time (year of data collection) or spatial location. While cross-validation shows *well enough* performance of different methods, when applying the same models to an independent dataset, the R^2 of at least one of the methods is close to zero. Similar results are reported in other disciplines (Castaldi et al., 2011; Huang et al.). Even strict cross validations may still be overoptimistic due to heterogeneity between datasets (Bernau et al., 2014). Thus, our results indicate that indeed these statistical methods are not replicable.

Changes in time and location change the distribution of feature space (Bareinboim and Pearl, 2016; Zhou et al., 2018) due to differences in measurements or state variables that control soil-plant-reflectance interactions. The state variables are those that are clearly represented in RTMs (Verstraete et al., 1996). The simplest statistical fix for the replicability of statistical methods is to seek models that perform well enough in the context of the leave-one-dataset-out test. None of the methods used in this study show strong overall performance with this test. More sophisticated solutions are based on methods that can compensate (or correct) for distributional shifts which may also be referred to as “domain adaptation” (Baktashmotlagh et al., 2013; Ganin et al., 2015). The recent framework developed by (Zhou et al., 2018) would enable us to identify and correct the distributional shift. The important point here is even if we correct for distribution shifting and we ignore the fact that we don’t have enough information about the vegetation to derive N , our model is still at best a predictive model and is not correlative. Because we are changing the distribution of features, as a consequence we might obtain a new set of

features which might have good predictive power, even for external datasets, but with limited correlative relation with N . Our conclusion is, if we ignore the impacts of canopy structure and soil on the total canopy reflectance and if the question at hand is just prediction not interpretation, then with some statistical manipulations we are able to produce predictive models. However, caution must be observed when interpreting these models, and in particular at scales larger than the leaf scale.

Canopy structure and soil dominate the total canopy reflectance

Figure. 2.5 shows the boxplot of estimated spectral invariants at the canopy and plot scales. Here we assume a two-layer system in which a layer of a canopy is on top of a layer of soil, an assumption similar to many open canopy ecosystems. However, this approach can be extended to layers of multiple canopies from different species and understories. The probability of a photon intercepted by the canopy and soil are i_0 and $1 - i_0$, respectively. $P_{\{LL\}}$, $P_{\{LS\}}$, and $P_{\{SL\}}$ are the probabilities of photon interactions between canopy-canopy, canopy-soil and soil-canopy, respectively. Figure. 2.5 shows changing scale from canopy to plot should affect $P_{\{SL\}}$ and i_0 , but not $P_{\{LL\}}$ and $P_{\{LS\}}$. This is because the probability that a photon escapes from the canopy ($1 - P_{\{LL\}} - P_{\{LS\}}$) should remain independent of soil condition (e.g., reflective vs. non-reflective). At the canopy scale the mean of i_0 is 0.17, and at the plot scale, it is 0.05. This low number simply shows the large impact of the soil on the total reflectance at both canopy and plot scales. For example, if we assume no additional interaction between photons from vegetation and soil, the total canopy reflectance is composed of 17% information from the shrub and 83% from the soil. At the plot scale, the contribution of soil can be represented in two forms, photons leaving the soil towards the sensor and photons leaving the soil and contributing to the CRB. Thus,

the impacts of the soil at the plot scale are more than the canopy. Figure. 2.6 compares the simulation for two shrubs. The contribution of canopy reflectance to total reflectance is much higher in the green shrub. If we remove the contribution of soil in the CRB for the dry shrub, then the residual (which is reflectance of the canopy itself) is close to zero. This is expected since there is no leaf on the canopy. Finally, Figure. 2.7 shows the simulations of different components of the total canopy and plot reflectance for all samples. Not surprisingly the greater impact of soil at the plot scale, compared to the canopy scale, is observable.

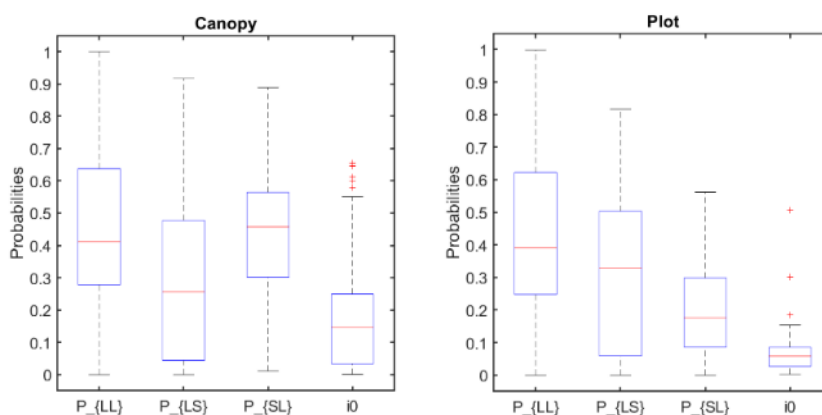


Figure. 2.5 Spectral invariant parameters at canopy (left) and plot (right) scales.

The next step is to estimate the impact of canopy structure on the total BRF. We removed the soil contribution in total BRF, and the residual was used to calculate the DASF (Materials and methods). Among 151 samples at the canopy scale, we could not calculate DASF for 49 samples. These shrubs are mostly located in California sites suffering drought that have few small leaves (e.g., Figure. 2.6 left). Thus, after removing the impact of soil, the residual is close to zero and calculating DASF is meaningless. As expected, this problem is worse at the plot scale. In fact, we could not calculate DASF for any of the plot samples after removing soil. This is another piece of evidence that supports the rejection

of using a cross-validated statistical N estimate at the plot scale (Table S3). In conclusion, the majority of the information contained in the plot reflectance is from the soil (up to 95%) and after removing it, there might not be enough information to infer canopy structure or N. Thus our statistical prediction of foliar N at the plot scale is unreliable.

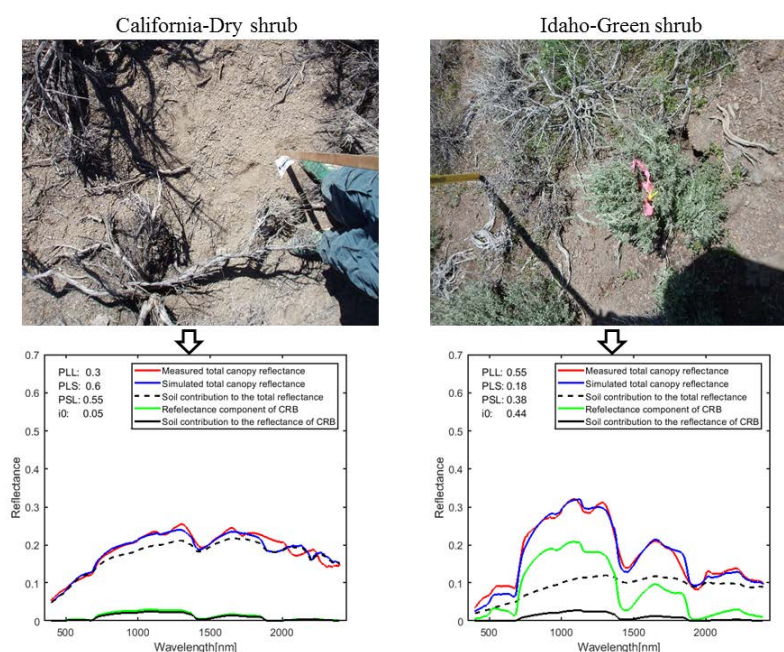


Figure. 2.6 Comparison of simulations between a dry shrub (left) located in California and green shrub (right) located in Idaho.

The R^2 of the BRF/leaf albedo ratio vs. BRF relationship is an estimate of the DASF quality retrieval. A note of caution is that, in theory, it is still possible to estimate DASF values with an R^2 close to one for small BRF. However, the estimated DASF is very small. Normalizing canopy BRF to a small DASF will result in large canopy scattering (W more than one) which is impossible. This is important since filtering sparse vegetation based on this R^2 has been recently suggested (Köhler et al., 2018), which may lead to incorrect canopy scattering. For green shrubs, DASF has a positive correlation (Figure. 2.8) with the shoulder of the NIR region (800-850 nm). This is in line with the radiative transfer process and Knyazikhin et al. (2013) (Yuri Knyazikhin et al., 2013c) findings.

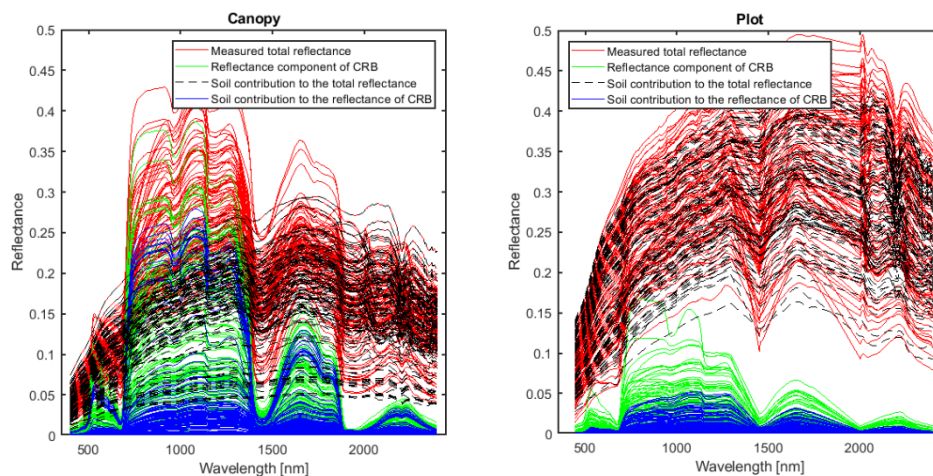


Figure. 2.7 Simulation of different components of total reflectance of canopy (left) and plot (right) samples.

Figure. 2.9 shows canopy scattering for the shrubs for which we were able to calculate DASF. Canopy scattering mimics a typical leaf albedo and is insensitive to canopy structure (Yuri Knyazikhin et al., 2013c), demonstrating success with the DASF approach. In the next section we experiment with using canopy scattering across all wavelengths to predict foliar N.

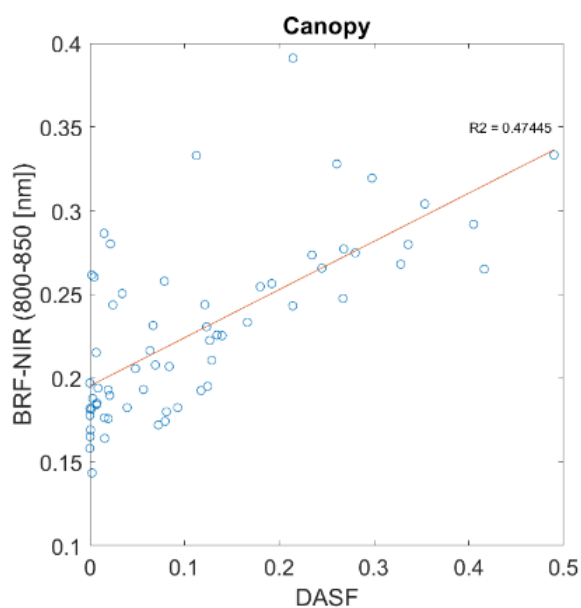


Figure. 2.8 Relationship between DASF and BRF in the NIR region.

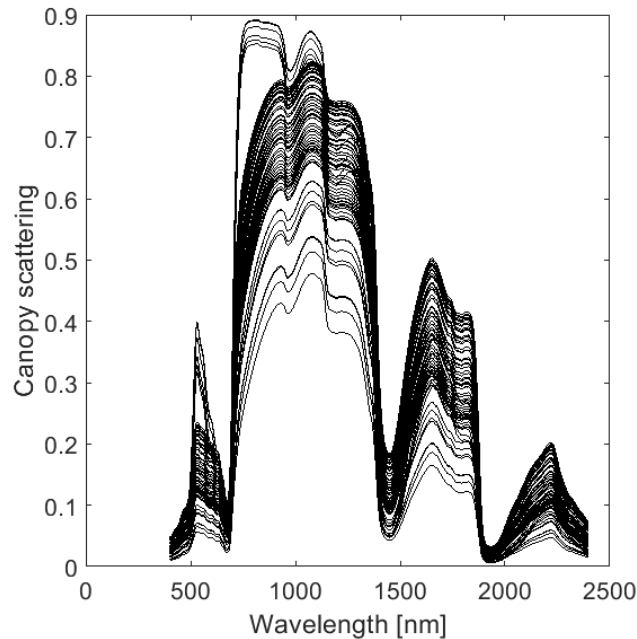


Figure. 2.9 Canopy scattering correction for soil and canopy structure.

Correlation and causation and the concept of counterfactual

Table 2.1 shows the results of corrected canopy samples versus their counterpart samples which were not corrected for soil and canopy structure. It can be seen that after correction for canopy structure and soil, none of the methods or transformations predict N for canopy-scale data. Since we selected the log transformation for our statistical analysis, we also provided its 1:1 plots between measured and predicted N before and after corrections (SI, Figure. S5). The correlation between N and reflectance implies association (dependence) rather than causation. Association can exist between two variables in the presence or absence of causality (Altman and Krzywinski, 2015). It is common to deduce a causal relationship from a correlation. For any causal claim to be verified, one should consider the *might be* condition. For example, what might be the case for the N-light relationship if canopy structure and soil did not exist? This is known as the theory of *counterfactual* (Lewis, 2000). Causality is the fundamental property of a system which

means a causal relationship would be *invariant* to the changes of the system. Our physical analysis provides the basis to test for counterfactual outcomes. Since the results of the N prediction before and after correction for soil and canopy structure have changed, a causal relationship between reflectance and N cannot be concluded. Consequently, we reject our null hypothesis that removing confounding factors improves predictions.

Table 2.1 Empirical estimation of canopy N for shrubs corrected for the impact of soil and canopy structure.

	Before correction for structure and soil					After correction for structure and soil				
	Ensemble			BR	PLS_ref	Ensemble			BR	PLS_ref
	PLS	SVM	RF			PLS	SVM	RF		
Smoothed										
R2	0.61	0.49	0.37	0.37	0.51	0.19	0.18	0.16	0.18	0.08
CV	16.87	1.90	2.66	8.32	9.17	6.54	6.75	0.32	23.73	27.38
Log transformation										
R2	0.60	0.62	0.37	0.47	0.52	0.18	0.19	0.16	0	0.08
CV	18.74	19.63	22.34	16.49	19.42	26.57	26.91	30.54	26.9	27.36
First derivative										
R2	0.57	0.54	0.61	0.35	0.42	0.17	0.16	0.15	0	0.07
CV	19.79	19.46	16.24	18.34	21.68	26.58	26.71	30.1	26.3	27.46
Log transformation of the first derivative										
R2	0.58	0.74	0.67	0.36	0.52	0.12	0.16	0.17	0	0.05
CV	18.27	14.21	15.45	16.13	19.28	26.52	26.59	30.33	27.06	27.41

One argument is that N-reflectance correlation implies a *functional association* (Ollinger et al., 2013), which is consistent with ecological understanding (i.e., plant physiology). From our analysis, correction for canopy structure and soil leads to no correlation. This does not, however, invalidate the functional association. Undoubtedly, N plays an important role in different canopy processes, however not all associations lead to

correlation (Altman and Krzywinski, 2015). The functional association can be translated into *a priori* information. Currently, remote sensing alone is not able to incorporate such *a priori* information into predictions of N. Dynamic vegetation models (DVMs) can be used to reconcile the theory of remote sensing and ecology. For example, these models incorporate both ecological processes (e.g., photosynthesis) and light-canopy interactions (e.g., radiative transfer models).

To account for the role of canopy structure -and to some extent soil- two solutions have been proposed. First, empirical models are applied to adjusted spectra that have been filtered with a normalized difference vegetation index (NDVI) and height and then adjusted with a brightness-normalization (Asner et al., 2015b). A second approach is to add lidar-derived canopy structural parameters such as canopy height or fractional cover to the feature space to construct the statistical model (Ewald et al., 2018b). In both approaches, multiple scattering is not explicitly solved. The impact of canopy geometry such as orientation and arrangement of leaves and branches, as well as multiple scattering between the canopy and different layers of understory, including soil, confound the N signal. Adding lidar variables to the feature space, makes the final model more complicated to interpret rather than simpler.

Conclusion

Due to the lack of inclusion of N in leaf radiative transfer models, N historically has been estimated with remote sensing data using statistical methods (Homolová et al., 2013a). The interpretation of the statistical models depends on the spectral bands selected during the process of model fitting. We have shown that different models can identify different important bands (Figure. 2.1). Moreover, each model is sensitive to the type of

transformation applied to the spectra before model fitting. These experiments show that common variable selection routines for foliar biochemistry studies at scales coarser than the leaf may be misleading. Strong prediction rates reported in remote sensing studies are often based on cross-validation which may be overoptimistic. None of our empirical methods could reproduce cross-validation results when applied to an external dataset. Thus, we concluded that these methods are not replicable.

We extended the physical work of (Yuri Knyazikhin et al., 2013c) to cases where vegetation is sparse, and soil cannot be ignored. At the plot scale, the impact of soil is a dominant confounding factor and in more extreme cases such as drylands, there might not be enough information to retrieve biochemistry or some canopy structure variables such as DASF. Recent developments using full-waveform lidar may solve the problem of canopy structure (Ilangakoon et al., 2018). Removing confounding factors at the canopy and plot scales lead to different statistical models that might or might not have prediction power. We discussed this against the theory of counterfactuals, leading to rejection of our null hypothesis that removing confounding factors will improve empirical predictions. The idea of functional association, which is used to justify statistical methods, is best suited for remote sensing coupled with DVMs.

Our overall conclusion is that if we are interested in predicting N with remote sensing, then we might be able to produce such empirical models, in particular with the growing body of machine learning algorithms. However, one must be cautious in interpreting these models, particularly in complex ecosystems, because they may be affected by the canopy structure, soil, spectral transformation, and the type of model implemented. With advancements in spaceborne hyperspectral and full-waveform lidar

observations and thus sophisticated measurements of ecological processes (e.g., photosynthesis, solar-induced fluorescence, etc.), there is strong potential to gain new insights of changing ecosystems (Stavros et al., 2017). Empirical methods serve an important role in analyzing the products of these newly developed sensors. Given the issues related to empirical methods, the remote sensing community should be cautious about the statistical tools they use. We encourage deeper discussions of these methods and the need to explore new fields in statistics for remote sensing, such as a rigorous investigation of causality and predictivity versus significance of variables.

Our results might imply that radiative transfer modeling is the best approach to estimate N. However, currently there is no reliable leaf scale RTM that incorporates N because of the lack of absorption coefficients and other information, due to the many different types of bonds N carries (Ustin, 2013). Moreover, RTMs at both the leaf and canopy scales carry multiple implicit and explicit assumptions that might cause relative error up to 70% (Stuckens et al., 2009). For example the assumption of considering canopy as turbid media in 1-D RTMs leads to the definition of *effective* LAI, which is different from true LAI measured (B. et al., 2006). Regardless, these deficiencies do not make RTMs useless. Most DVMs require RTMs to simulate the canopy radiation budget. Thus, a potentially better approach to solve the problem of N retrieval is to incorporate it with the DVMs (i.e., through data assimilation) rather than using remote sensing data in isolation. For example, The ED2 (Medvigy et al., 2009a; Moorcroft et al., 2001) and CLM (M et al., 2011) DVMs use a simple two-stream canopy RTM (Sellers, 1987). Incorporation of more sophisticated 3-D RTMs into these models might improve their performance (Fisher et al., 2018) and consequently facilitate better N predictions. Additionally, the canopy spectral

invariants theory has produced results close to 3-D RTMs (Yáñez-Rausell et al., 2015) with much faster performance and thus a logical next step is to incorporate the generalized canopy spectral invariants theory into DVMs.

CHAPTER THREE: PERFORMANCE OF ECOSYSTEM DEMOGRAPHY MODEL
(EDv2.2) IN SIMULATING PHOTOSYNTHESIS CAPACITY AND ACTIVITY
ALONG AN ELEVATION GRADIENT IN A DRYLANDS STUDY AREA

This chapter is currently under review for publication.

Abstract

Vegetation in dryland ecosystems plays an important role in the global carbon cycle such as regulating the global inter-annual carbon sink. Due to rapid changes of forcing variables such as precipitation and temperature along elevation gradients in drylands, the vegetation function and structure at lower elevations can be different from higher elevations. Gross primary production (GPP) is photosynthesis at the ecosystem scale and its capacity and activity are primary indicators of ecosystem state. In this study, we implement the Ecosystem Demography (ED. v2.2) model to simulate GPP over an elevation gradient in a watershed located in the Great Basin, western US. We performed a thorough sensitivity analysis using the Morris technique and calibrated the model with the Parameter Estimation and Uncertainty Analysis (PEST++) framework. The GPP capacity and activity were investigated by comparing model simulations with GPP estimated from eddy covariance data and remote sensing products. Our time series analysis was based on Bayesian model averaging for trend analysis and cross-correlogram spectral matching for phenometrics (start/end of the season) retrieval. Our preliminary results show good performance of EDv2.2 (validation monthly RMSE ≈ 0.38 [kgC/m²/year]) between simulated and measured GPP in lower elevations. Moreover, our time series analysis using

remote sensing data showed that EDv2.2 captures the long-term trend in this ecosystem, however it doesn't perform well in capturing phenometrics. The performance of the model degrades in higher elevations with greater GPP which requires introducing more diversity (e.g. more plant functional types) and modifying plant processes (e.g. plant hydraulics and phenology) to improve the model performance.

Introduction

Dryland vegetation plays an important role in the global carbon budget. The dominant role of dryland ecosystems in regulating interannual variability of the global land carbon sink has been highlighted in several studies (Ahlström et al., 2015; Metcalfe, 2014; Poulter et al., 2014). Vegetation dynamics in drylands is a function of forcing variables such as precipitation and temperature. Due to rapid changes in these forcing variables along elevation gradients, vegetation structure and function at lower elevations can be significantly different from higher elevations. Moreover, long term changes in forcing variables caused by climate change can drive trends in vegetation productivity. These drivers may not only impact vegetation processes such as photosynthesis but also vegetation composition (Dorji et al., 2014; Hawkins et al., 2003). For example, climate change in drylands of the Great Basin, US, may lead to a shift from snow to rain which itself favors the encroachment of invasive species such as cheatgrass (*Bromus tectorum*) that replace native shrubs (Concilio et al., 2013; Polley et al., 2013; Scott et al., 2015). Understanding the spatial and temporal dynamics of vegetation in drylands is essential for global-scale studies on carbon balance and atmospheric CO₂.

Gross primary production (GPP) is the ecosystem-scale apparent photosynthesis and is a primary indicator of ecosystem state (e.g., carbon sink/source). Direct

measurement of GPP is a challenging task (Ryu et al., 2019; Yan et al., 2019), and more common methods are based on data from eddy covariance (EC) towers, remote sensing, and dynamic global vegetation models (DGVMs) (for the latest review refer to Ryu et al., 2019). GPP (i.e., photosynthesis) can be discussed in terms of capacity and activity (Medvigy et al., 2013; Smith et al., 2018). GPP capacity refers to the absolute amount of carbon sequestered by plants (e.g., $\text{kgC/m}^2/\text{year}$), and GPP activity describes temporal dynamics of photosynthesis. While EC data may provide better estimates of GPP capacity at point locations compared to remote sensing, it is limited in terms of GPP activity due to the lack of long term (e.g., decadal) continuous data, especially in drylands (Smith et al., 2018). Remote sensing-based GPP from the MODerate Resolution Imaging Spectroradiometer MODIS sensor (Running et al., 2004) provides long term data that can be used for analysis of photosynthesis activity, however there is systematical under- or overestimation of GPP depending on the ecosystem (Stocker et al., 2019; Verma et al., 2014).

Process-based DGVMs are important tools in studies of GPP capacity and activity that can overcome the challenges associated with EC towers and remote sensing. However, an understanding of DGVM capabilities and limitations in an ecosystem is necessary to capture uncertainties. An evaluation of a DGVM should include model parametrization, sensitivity analysis (SA), calibration, and evaluation (Fer et al., 2018; Keenan et al., 2013; Kuppel et al., 2012; Pandit et al., 2019; Post et al., 2017; Renwick et al., 2019; Santaren et al., 2007; Wang et al., 2001). There is an information gap regarding DGVM evaluation in drylands and more specifically in regions where the drivers in ecosystem processes may vary across an elevation gradient. Renwick et al. (2019) implemented the LPJ-GUESS

DGVM (Smith et al., 2001) and modified the phenology routine in this model. They calibrated the model by minimizing the objective function of all sites along an elevation gradient simultaneously. This approach may be limiting in ecosystems in which GPP capacity and activity are controlled by different processes across a study area (Flerchinger et al., 2019). Many studies have investigated the correlation between simulated GPP and GPP estimated from EC towers or remote sensing (Antonarakis et al., 2014; Pandit et al., 2019; Renwick et al., 2019; Trugman et al., 2016), which is more applicable to GPP capacity rather than activity. More explicit metrics of GPP activity are required to fully capture the performance of models in terms of vegetation dynamics. Phenometrics, such as start of season (SOS) and end of season (EOS), and long-term trend analysis are examples of criteria that can be used for studying GPP activity (Chen et al., 2016; Forkel et al., 2015a; Zhao et al., 2019). The SOS and EOS are useful indicators of many ecosystem dynamics and their response to phenomena such as climate change (Myneni et al., 1997; Richardson et al., 2013; Tucker et al., 2001; Xu et al., 2013).

The focus of this paper is on the Ecosystem Demography model version 2 (EDv2.2; Medvigy et al., 2009; Moorcroft et al., 2001). Unlike most DGVMs, EDv2.2 represents the vertical and horizontal heterogeneity of terrestrial ecosystems (Longo et al., 2019a, 2019b). This model has been implemented with acceptable performance in different ecosystems (Antonarakis et al., 2014; Davidson et al., 2011; Kim et al., 2012; Levine et al., 2016; Lokupitiya et al., 2016; Medvigy et al., 2013, 2012; Trugman et al., 2016; Xu et al., 2016; Zhang et al., 2015) and has been recently incorporated into the widely used Community Land Model (CLM-ED) as the vegetation model (Fisher et al., 2015).

Here our objective is to evaluate the ability of ED.v2.2 to capture GPP capacity and activity along an elevation gradient in a dryland study area. To address this objective we perform a sensitivity analysis and calibrate the model. We investigated the GPP capacity by comparing the model output with EC tower data along an elevation gradient. The analysis of GPP activity is based on comparing the model simulations with remote sensing data. In particular, we are interested in the long term trends and the phenology observed in the model. We make two assumptions in this study. First, that the processes included in the EDv2.2 model are suitable for dryland GPP simulations across an elevation gradient. The implication of this assumption is that we do not seek model improvement through refinement of different processes. The second assumption is that remote sensing GPP products capture the dynamics of vegetation production in our study area. This work builds on lessons learned from previous efforts to estimate GPP in the same study area (Flerchinger et al., 2019; Pandit et al., 2019; Renwick et al., 2019), all of which recommend additional investigations into model development within drylands.

Material and methods

Study area and data

The study area is Reynolds Creek Experimental Watershed (RCEW), a NSF Critical Zone Observatory (CZO), and monitored by the USDA Agricultural Research Service since 1960. RCEW is located in the western US (Figure 3.1). The elevation gradient in RCEW is 900-2200 m. With increasing elevation, the mean annual precipitation increases and temperature decreases (Flerchinger et al., 2019; Renwick et al., 2019). In this study, we used three EC towers located at different elevations in RCEW (Figure 3.1, Table 3.1). The dominant vegetation cover of each site is a different species of sagebrush

(*Artemisia* spp.) including Wyoming big sagebrush (*Artemisia tridentata* ssp. *wyomingensis*), low sagebrush (*Artemisia arbuscula*) and mountain big sagebrush (*Artemisia tridentata* ssp. *vaseyana*). Our site with dominant Wyoming big sagebrush (WBS site) has the lowest elevation, the low sagebrush site (LS site) is in mid elevation and mountain big sagebrush site (MBS) has the highest elevation. Other vegetation at the WBS site includes green rabbitbrush (*Chrysothamnus viscidiflorus*), spineless horsebrush (*Tetradymia canescens*), cheatgrass and perennial graminoids including bluebunch wheatgrass (*Pseudoroegneria spicata*), squirreltail (*Elymus elymoides*), and Sandberg bluegrass (*Poa secunda*). The LS site includes predominantly Sandberg bluegrass, squirreltail (*Elymus elymoides*), and Idaho fescue (*Fescue idahoensis*). Mountain snowberry (*Symphoricarpos oreophilus*) is also a common shrub at the MBS site. Cheatgrass is less abundant at both LS and MBS compared to the WBS site, however at LS and MBS there is a strong presence of forbs including longleaf phlox (*Phlox longifolia*), pale agoseris (*Agoseris glauca*), and silvery lupine (*Lupinus argentius*). A full description of each of these sites is presented in Flerchinger et al. (2019).

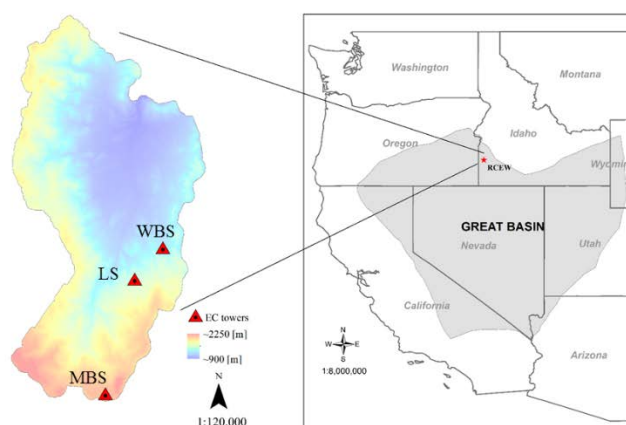


Figure 3.1. Location of EC towers in Reynolds Creek Experimental Watershed, Idaho.

Table 3.1. Site descriptions of the three eddy covariance sites, WBS, LS, MBS.

Site	Elevation [m]	Dominant vegetation cover	Mean annual precipitation [mm]	Mean annual temperature [°C]	Data availability (water year)
WBS	1187.9	Wyoming big sagebrush	307.94	9.75	2014-2016
LS	1618.4	Low sagebrush	367.42	9.02	2015-2016
MBS	2113	Mountain big sagebrush	586.15	4.58	2014-2016

Field inventory data were collected during September–November of 2014 and May and June of 2015 at 48 plots (10 × 10 m) distributed across a range of elevation, cover, and species (Glenn et al., 2014). Hourly meteorological forcing variables for the years 1988–2017 were based on high resolution (1 km²) downscaled reanalysis data obtained from the Weather Research and Forecast (WRF) model recently developed for portions of the western US (Flores et al., 2016). The partitioning of Net Ecosystem Exchange (NEE)

recorded at the EC towers into ecosystem respiration and production (GPP) is fully described in Fellows et al. (2017). The tower GPP data covers water years 2015-2017. We also used GPP products (MYD17A2H006) from the MODIS sensor (Running et al., 2004) from 2000-2017. The spatial and temporal resolutions of the MYD17A2H006 GPP product are 500 m and 8 days, respectively. Bad GPP values due to sensor noise or cloud cover were removed from the analysis.

Ecosystem Demography model

We implemented the EDv2.2 model at a point scale to correspond with the EC towers. A full description of the biophysical and biochemical cycles within the EDv2.2 model are described in Longo et al., 2019b. In this model, at the static level the study area is divided into different sites based on the meteorological and abiotic (e.g. soil type) conditions. At the dynamic level, each site is divided into patches based on the time since last disturbance. Within each patch, individuals are grouped into cohorts based on plant functional type (PFT) and height of the plant (Fisher et al., 2018). We utilize the shrub PFT developed by Pandit et al. (2019) specifically for the ecosystem we are studying.

Sensitivity analysis and model calibration

For the sensitivity analysis (SA) and model calibration, we utilized shrub PFT parameters with strong relationships to GPP simulation (Table 3.2). The initial and lower/upper values are based on literature review or derived from Pandit et al. (2019). A complete description of these parameters is presented in Pandit et al. (2019), and broader descriptions of PFT parameters for ED is available in Longo et al. (2019b). In this study, we implement a global sensitivity analyses method known as the Morris method (Morris, 1991). Morris sensitivity analysis (SA) returns the distribution of the elementary effect of

each parameter. The absolute value of the mean (μ^*) of this distribution represents the influence of each parameter on the outputs. The standard deviation (σ) is the variability of this influence, which is a function of model nonlinearity or parameter interactions (Campolongo and Saltelli, 1997; Saltelli et al., 2000; White et al., 2019). Although Morris SA provides μ^* and σ , it is generally considered a more qualitative SA rather than quantitative (Pappas et al., 2013; Saltelli et al., 2000). Users provide the number of times an elementary effect is to be calculated for each parameter (denoted as r). The number of model runs is then $r \times (m + 1)$ where m is the number of parameters. In this study, we set $r = 10$ as suggested in multiple studies (Campolongo et al., 2007; White et al., 2019), and thus the number of model runs for the Morris SA with 12 parameters is 130.

Table 3.2. PFT parameters within EDv2.2, their abbreviation, and initial, lower and upper boundaries selected for the Morris sensitivity analysis.

Parameter name	Abbreviation	Initial	Lower boundary	Upper boundary
Specific leaf area [m ² kg ⁻¹]	SLA	4.5	2.0	15.0
Carboxylase rate constant [μmolm ⁻² s ⁻¹]	VM0	16.5	4.0	30.0
Stomatal slope	STO_S	7.0	2.0	15.0
Ratio of fine root to leaf biomass.	Q_RATIO	3.2	0.4	12.0
Root turnover rate [a ⁻¹]	FTR	0.33	0.1	2.0
Leaf turnover rate [a ⁻¹]	LTR	1.0	0.1	2.0
Growth respiration factor	GRESP	0.33	0.11	0.66
Cuticular conductance [μmolm ⁻² s ⁻¹]	CUT_C	1000.0	100.0	10000.0
Water conductance	WAT_C	1.900000E-05	1.90E-06	1.90E-4
Seedling mortality	S-MOR	0.95	0.25	0.99

The SA was based on the effect of each parameter on the objective function defined as:

$$\Phi_m = \sum_{i=1}^n (y_{m,i} - y_{s,i})^2 \quad (3)$$

Where $y_{m,i}$ and $y_{s,i}$ are the daily GPP observed from EC data (water years of 2014-2016) and simulated using EDv2.2, respectively.

Calibration of EDv2.2 was done using the PEST++ package (White et al., 2019).

The calibration method is based on a Tikhonov regularization and truncated singular value

decomposition (SVD) regularization (Doherty, 2005; Fang et al., 2019). The idea of Tikhonov regularization is simply to add “expert knowledge” on the parameter’s values to the calibration processes. In this case the objective function has two components, one pertaining to model-to-measurement misfit (Φ_m , similar to Equation 3) and the other pertaining to Tikhonov constraints Φ_r (similar form as Φ_m but for parameters) which controls the distance between optimized parameters and expert’s knowledge during calibration. Thus, the total objective function is defined as:

$$\Phi = \Phi_m + \mu^2 \Phi_r \quad (4)$$

The μ^2 is the regularization weight factor which PEST++ iteratively estimates (White et al., 2019). In this study, we consider the initial values (Table 3.2) as the expert knowledge of the parameters. In order to reduce the number of free parameters in the calibration process, we performed the calibration for highly sensitive parameters obtained through a sensitivity analysis. EDv2.2 was calibrated using daily observations of the EC towers for each site (Table 3.1). In each iteration during calibration, the model was initialized with field inventory data and run for 10 years (2006-2016). In each site the last water year of observation (2016; Table 3.1) is considered as the validation set and the remaining years were used for calibration.

Evaluating GPP capacity and activity

In order to evaluate the model in terms of its performance to estimate photosynthetic capacity, we calculate the Root Mean Square Error (RMSE) between GPP simulated from EDv2.2 and GPP observed from the EC towers. Since the EC tower data are temporally limited (Table 3.1), a meaningful time series analysis is challenging. Thus, for model evaluation of long term photosynthetic activity we compare the start of season (SOS) and end of season (EOS) and trends retrieved from the calibrated model simulations

and MODIS GPP for the 2000-2017 time period. Estimation of SOS and EOS is based on a weighted cross-correlogram spectral matching-phenology (CCSM-P; Chen et al., 2016). The trend analysis is based on the recently developed Bayesian Estimator of Abrupt change, Seasonal change, and Trend algorithm (BEAST; Zhao et al., 2019). BEAST is able to decompose a time series into its seasonal and trend components; due to its Bayesian nature it returns confidence intervals on these components. For both phenology and trend analyses, we aggregated the daily simulated and MODIS GPP into monthly values based on the maximum composition approach (Forkel et al., 2015a; Holben, 1986).

Results

Figure 3.2 shows the results of the Morris sensitivity analysis (SA). Among all parameters, the SLA, STO_S, CUT_C, and VM0 show the highest individual influence (μ^*). These parameters also show the largest non-linear influence and interaction effect at all sites (σ). The other eight parameters are clustered at the lower left of the figures, indicating that EDv2.2 is less sensitive to them in simulating GPP. The sensitivity of the model to the four most important parameters is slightly different at each site. For example, SLA has the highest μ^* and σ for the WBS site, while at the MBS site STO-S replaces SLA. Following our framework, we used these four parameters for calibration analysis.

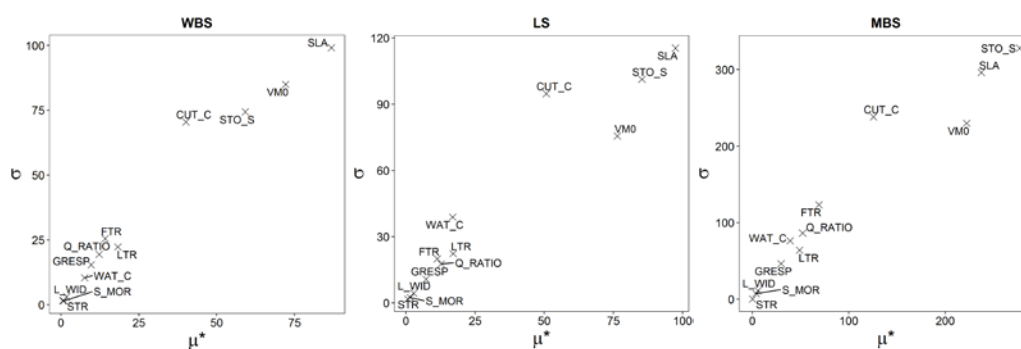


Figure 3.2. Sensitivity analysis based on Morris for WBS, LS, and MBS, μ^* and σ are the mean and standard deviation. At all three sites, SLA, STO_S, CUT_C, and VM0 are identified based on this analysis as the most important parameters to estimate GPP.

To evaluate the GPP capacity using the results from the Morris SA, we used SLA, STO_S, CUT_C, and VM0 for calibration with PEST++. Table 3.3 shows the corresponding standard deviation and confidence intervals. Table 3.4 shows the calibration/validation RMSE between simulated and estimated GPP from EDv2.2 and the EC towers, respectively. We exclude MBS (highest elevation site) from Table 3.4 because the EDv2.2 calibration process resulted in no vegetation growth (zero GPP) for this site. This is because PEST++ couldn't converge at the MBS site and the estimated best parameter values are incorrect. The wide confidence intervals (which sometimes included negative values) provide additional evidence that the estimated parameters for MBS site are not reliable. We also found a wider standard deviation and confidence interval for the LS site for all of the parameters in comparison to the WBS site (the lowest elevation). For example, the lower-upper STDV range of SLA [m^2/m^2] for the WBS site is 6.04-6.18 while for the LS site it is 6.55-845 (Table 3.3). With this information, we conclude that the best EDv2.2 performance in terms of GPP capacity is attained for the WBS site. Figure 3.3 shows the observed vs. EC tower GPP for this site. Subsequently, we base our time series analysis for evaluating long term performance of EDv2.2 on GPP activity on this site. The

mean annual observed and estimated GPP for this site is 0.38 [kgC/m²/year] and 0.30 [kgC/m²/year] respectively. Note that the model underestimated GPP for the 2017 water year, when observed GPP is higher than the average.

Table 3.3. PEST++ results for SLA, STO_S, CUT_C, and VM0 and their uncertainty.

Parameter	WBS		LS		MBS	
	Best	STDV (upper bound; lower bound)	Best	STDV (upper bound; lower bound)	Best	STDV (upper bound; lower bound)
SLA	6.14	0.03 (6.04;6.18)	7.50	0.47 (6.55;8.45)	2.82	3.25 (-3.67;9.32)
VM0	24.50	0.21 (24.06;24.93)	19.45	0.48 (18.48;20.43)	7.44	2.04 (3.33;11.51)
STO_S	13.97	0.03 (13.90;14.05)	9.85	0.53 (8.77;10.92)	7.82	1.98 (3.83;11.76)
CUT-C	999.51	112.184 (775.143;1223.88)	1000	462.68 (74.62;1925.37)	1000	267.44 (465.121;1534.89)
Number of model runs	166	---	56	----		

Table 3.4. Calibration and validation results for EDv2.2 for WBS and LS sites.

Site	Calibration	Validation
	RMSE (daily; monthly) [kgC/m ² /year]	RMSE (daily; monthly) [kgC/m ² /year]
WBS	0.22; 0.18	0.44; 0.38
LS	0.29; 0.24	0.47; 0.39

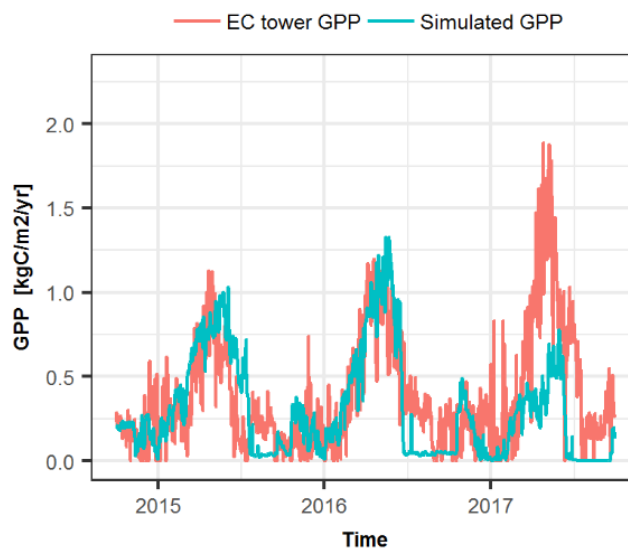


Figure 3.3. Model simulations vs. tower observation for WBS.

In order to evaluate GPP activity we estimated SOS and EOS for the MODIS GPP and simulated GPP (Figure 3.4). Visually there is a good agreement between MODIS and EDv2.2. However, the mean absolute deviation (MAD) of the SOS and EOS is 18.6 and 25.2 days, respectively. Figure 3.5 shows the one-to-one plot of the SOS and EOS. There is a low correlation between the EDv2.2 simulations and the MODIS phenometrics.

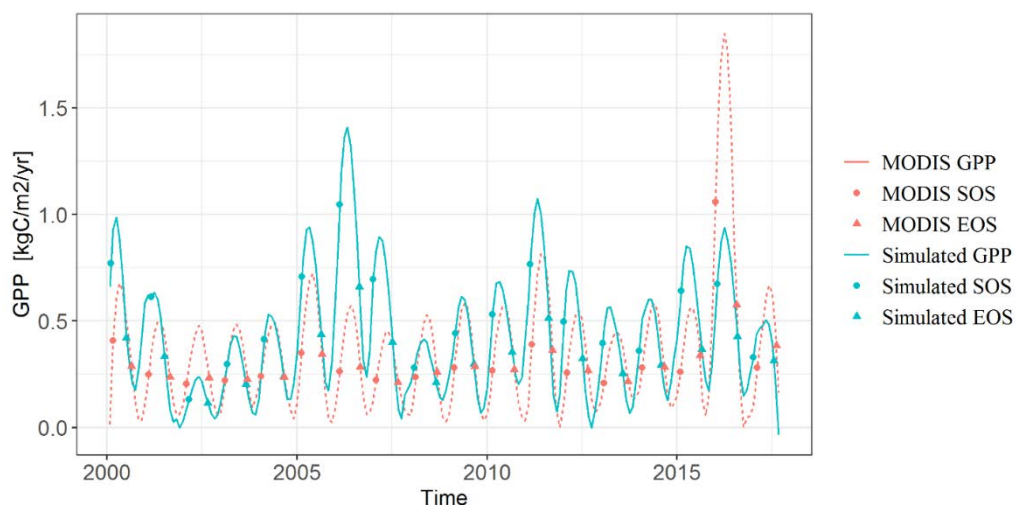


Figure 3.4. Phenometrics estimated from MODIS GPP and simulated GPP using EDv2.2.

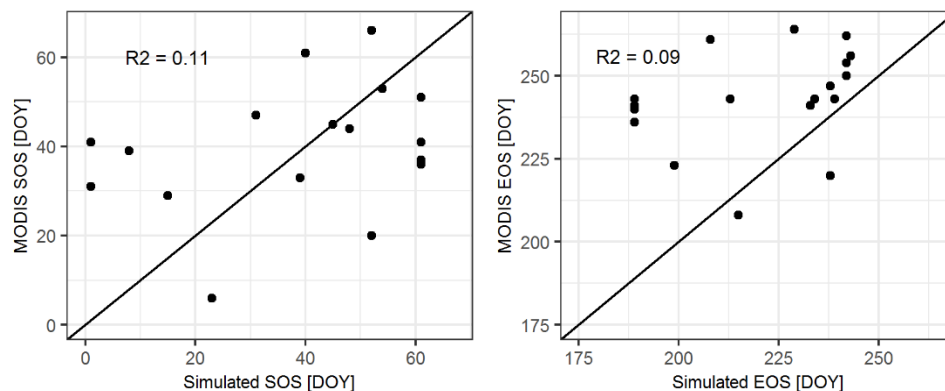


Figure 3.5. One-to-one plot between SOS and EOS estimated from MODIS and EDv2.2 GPP for WBS site (2000-2017).

The results of the trend analysis using the BEAST algorithm are shown in Figure 3.6. There is general agreement between MODIS and EDv2.2 during greening events, specifically in years 2011 and 2016. We also calculated the seasonal and trend components of precipitation for the WBS site (2000-2017) (Figure 3.7). The precipitation trend increases in years 2011 and 2017. This increase in precipitation leads to an increase in GPP in both the model and MODIS. However, there is a significant difference in the intensity of senescing events. For example between 2000 and 2004, MODIS shows no trend in GPP whereas the EDv2.2 shows a significant trend. In general the senescing and greening events are more intensified in the EDv2.2 simulations than in the MODIS GPP. Comparing seasonal components shows a similar pattern except for the year 2017, where MODIS GPP was higher and EDv2.2 shows no increase in seasonal GPP. Thus our main conclusion is that at lower elevations, precipitation drives the general trend of GPP which is captured by both MODIS and EDv2.2, however, the model generally exaggerates this trend in comparison to MODIS.

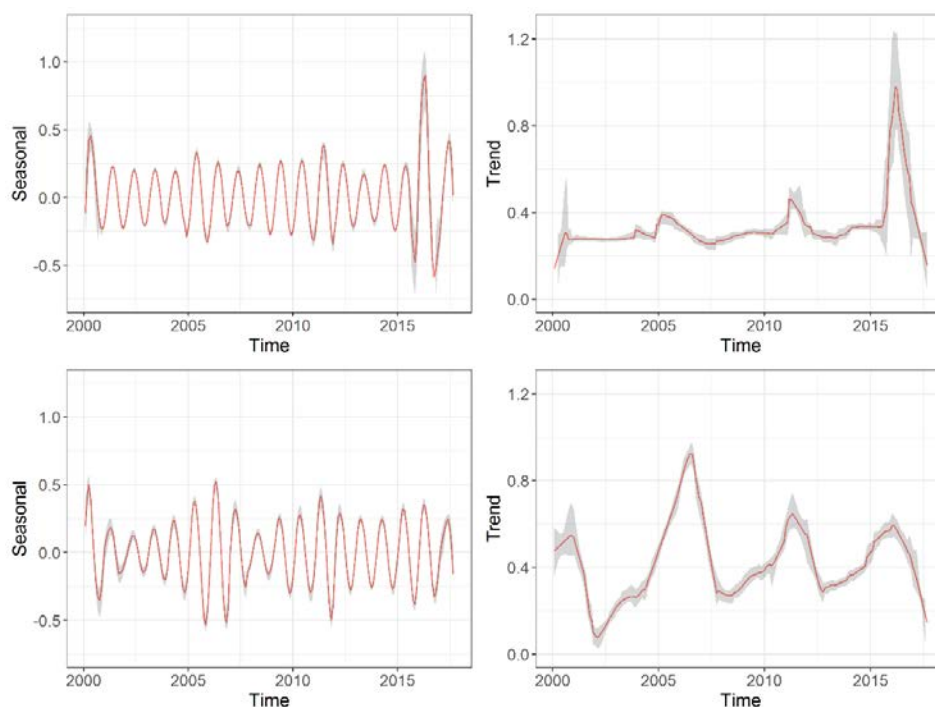


Figure 3.6. Estimated seasonal and trend components for MODIS (top row) and EDv2.2 GPP (bottom row) for years 2000-2017.

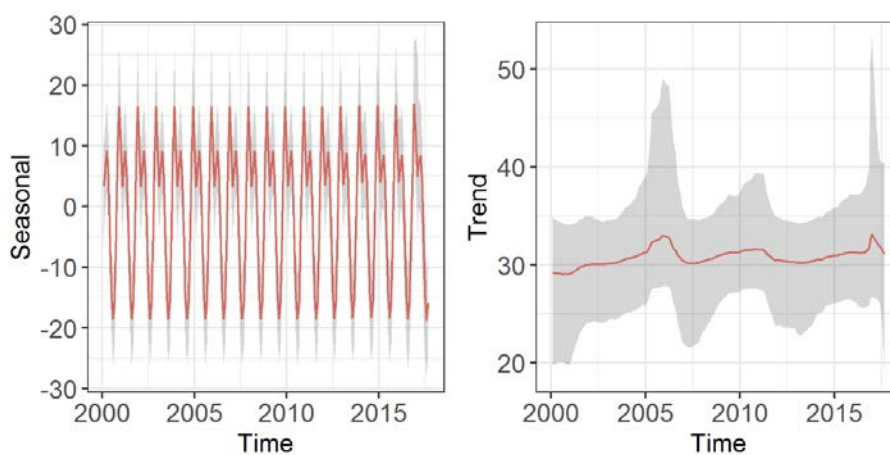


Figure 3.7. Precipitation seasonal and trend components and their confidence interval for WBS site (2000-2017). The precipitation data comes from WRF model.

Discussion

Sensitivity analysis

The main goal of the SA in this study was not to capture quantitative measures of model sensitivity to the parameters; rather, we intended to reduce the uncertainty of

calibration by excluding non-influential variables from the calibration process. This is in accordance with Pareto's principle in which a model includes a few influential parameters, and a majority of non-influential parameters (Pappas et al., 2013). Multiple studies show that results of the Morris SA can be trusted for calibration purposes (Hsieh et al., 2018; Janse et al., 2010; Tian et al., 2016). All four parameters indicated as influential are indeed used in the photosynthesis sub-model of EDv2.2 which is directly related to GPP. The stomatal slope is a fixed parameter in the stomatal conductance model (Leuning, 1995) which actively regulates the photosynthesis rate (Dietze et al., 2014). Cuticular conductance in EDv2.2 is equal to stomatal conductance when plants shutdown their stomata due to environmental stresses (Medvigy et al., 2009b; Moorcroft et al., 2001). The maximum carboxylation rate, VM_0 , is maximum photosynthesis at 15° C based on the photosynthesis model developed for C3 plants (Farquhar et al., 1980). Finally, SLA, scales leaf-level photosynthesis to the canopy-level (Dietze et al., 2014). We also compared our results with other studies in RCEW (Pandit et al., 2019; Renwick et al., 2019). Three of the four influential parameters in this study (SLA, STO_S and VM_0) are similar to those identified by Pandit et al. (2019). However, only SLA was identified as important by Renwick et al. (2019). These parameter discrepancies among studies may be due to the SA method or the DGVM structure. For example, in Pandit et al. (2019) a simple local SA was used in comparison to the Morris SA. In Renwick et al. (2019), the shrub PFT parameters for LPJ-GUESS model were analyzed using a ranked partial correlation coefficient. In addition to the methods, the structure of the LPJ-GUESS model is different from EDv2.2. The SA results might also change regarding different outputs of the model. For example the SA for net primary production (NPP) may yield different results than for GPP (e.g.

Dietze et al., 2014; Fer et al., 2018). Thus, differences in SA between studies is expected and one should consider the SA method, model structure, and target variables and ecosystems when evaluating any DGVM model performance.

GPP capacity

EDv2.2 performed well at the lower elevation WBS site, in terms of GPP capacity. The poor performance of EDv2.2 at the LS and MBS sites at higher elevation is probably best explained within the context of the calibration method used in this study (PEST++) and model structure. From a methodological point of view, PEST++ is a gradient-based method which mathematically searches for local minima in the objective function space (Doherty, 2005; White et al., 2019). Being trapped in local minima is one of the drawbacks of the gradient-based methods in cases where the model is highly nonlinear. It has been shown that the Gauss–Marquardt–Levenberg (GML) method and Tikhonov regularization algorithm used in PEST++ help with the local minima trapping issue. In general, global calibration methods such as Covariance Matrix Adaptation Evolution Strategy (CMAES; Hansen et al., 2003), Differential Evolution (DE; Storn and Price, 1997) and Bayesian approaches (e.g. Dietze et al., 2014; Fer et al., 2018) are preferable if their computational cost can be afforded. It is likely that some of the underestimation of GPP can be explained by the limited number of years used for calibration and validation of EDv2.2 in this study (Table 3.1). For example, the precipitation during years 2015-2016 used for the calibration is close to the average of the long term precipitation, however for year 2017, the precipitation was above average. Underestimation of GPP during 2017 may imply that the calibration time period is insufficient to properly parametrize these variables for application beyond the range of conditions encountered during 2015-2016. Thus,

increasing the calibration time period and introducing more anomalies (e.g. precipitation below or above long-term average) should improve the model performance.

For our particular study area, EDv2.2 performs more poorly when vegetation productivity is high. This can be observed by the model performance at the MBS site which has the highest GPP. Also, GPP was underestimated for the WBS site in 2017 when the EC data indicated that GPP was higher than during previous years (Figure 3.3). Currently there are several limitations in EDv2.2 that likely contribute to these results. One is the lack of ecosystem heterogeneity represented in the EDv2.2 model. Figure 3.8 shows the decomposition of total GPP into its PFT components for the WBS site. In this site the main vegetation cover types are shrub and grass, and EDv2.2 reasonably captured the contribution of these PFTs to GPP over time. As elevation increases at RCEW, the heterogeneity of the ecosystem also increases (Flerchinger et al., 2019). For example, the presence of grasses and forbs at MBS is noteworthy and can contribute up to ~50% to the carbon budget (Flerchinger et al., 2010). Thus, the lack of forbs and other PFTs common in drylands in EDv2.2 may partly explain the poor performance of the model in capturing photosynthesis capacity at higher elevations. The EDv2.2 model structure may also play an important role in its poor performance at more highly productive sites and years. For example, Flerchinger et al. (2019) found that the timing of complete snowmelt is a strong control on GPP at the MBS site. The snowmelt process is not included in EDv2.2. Recent advances in combining EDv2.2 with land surface models such as CLM-ED (Fisher et al., 2015) helps to mechanistically account for land surface processes such as snowmelt. Plant hydraulic traits control the water potential within the leaf which itself regulates processes such as photosynthesis and leaf shedding (Xu et al., 2016b). In EDv2.2, an empirical

method has been employed to represent plant hydraulic processes. For example, photosynthesis is regulated as a function of root water supply (Medvigy et al., 2009b). Recent advances in mechanistic representation of water hydraulics in EDv2.2 for tropical forests can be adopted for drylands.

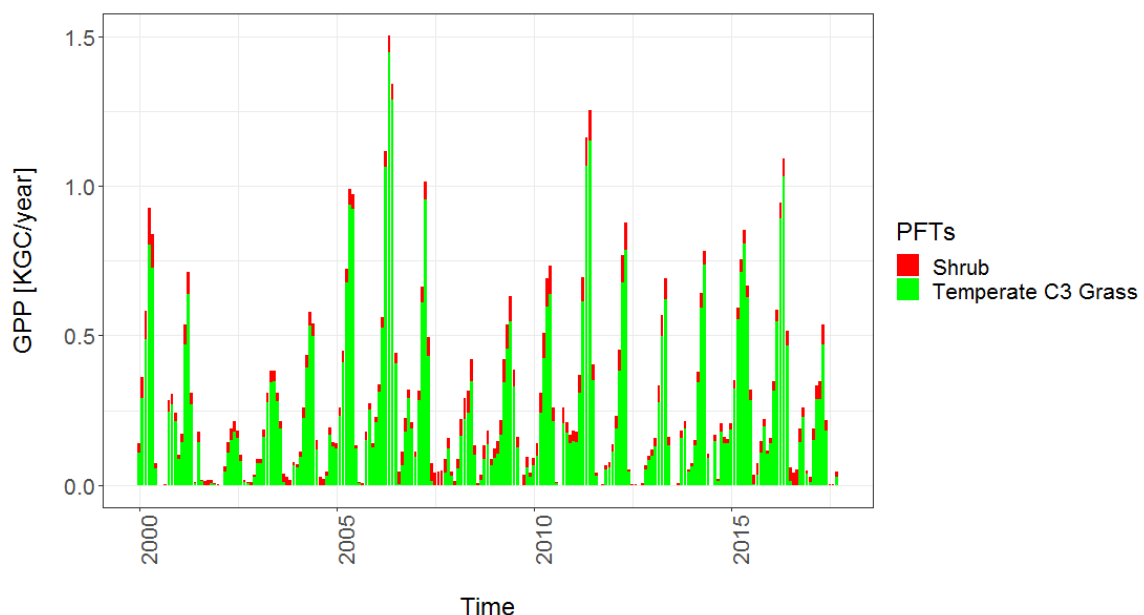


Figure 3.8. Contribution of shrub and grass PFTs in total GPP for WS site.

GPP activity

The difference between estimated phenometrics from MODIS and EDv2.2 may be due to a combination of uncertainty in remote sensing data, EDv2.2 model structure, and method used for the retrieval of SOS and EOS. In this study we used MODIS GPP for time series analysis. Analyses using Normalized Difference Vegetation Index (NDVI) and a newly developed vegetation index ($NIR_v = NDVI \times NIR$; Badgley et al., 2017) led to different results than the MODIS GPP (results not presented here). Which remote sensing dataset to use for phenological studies remains an open question. It has been shown that solar induced fluorescence (SIF) may better capture the dynamics of drylands (Smith et al.,

2018), and future studies could explore the potential of comparing SIF with EDv2.2 results (SIF data were not available for the 2000-2017 time frame assessed here). To our knowledge, the CCSM-P method for phenology analysis is the only method that can successfully detect phenological changes in a synthetic dataset (Chen et al., 2016). Testing any algorithm on a synthetic dataset is an essential part of the model algorithm evaluation (Zhao et al., 2019). Finally, the cold deciduous phenology sub-routine in EDv2.2 is based on changes in temperature (Botta et al., 2000), when deciduous plants drop their leaves. In reality, the phenology of sagebrush (dominant shrub in WBS site) is more complicated. Sagebrush is semi-deciduous and keeps some leaves during the cold season (Evans and Black, 1993; Williams et al., 1997). Renwick et al. (2019) recently developed a method to represent sagebrush phenology; however, the proposed method still needs empirical thresholds (e.g., percent of persistent leaves), which might be significantly different along an elevation gradient and dependent upon sagebrush species. In general, mechanistic modeling of phenology for any PFT is a challenging task (Forkel et al., 2015b; Migliavacca et al., 2012; Richardson et al., 2013).

Our results showed that, at lower elevations, the general decadal trend in GPP is coincident with the general trend of precipitation. This finding is consistent with an extensive analysis of the WBS site in Flerchinger et al. (2019) and other similar sites (Yan et al., 2019). However, the greening- senescing events are exaggerated by the EDv2.2 model. Since precipitation is the main driver of vegetation productivity and it shows more stable trends (Figure 3.7), we can conclude that EDv2.2 overestimates the greening-senescing events due to a model structural problem. EDv2.2 shows oversensitivity to precipitation at the WBS site, in which small changes in precipitation led to sharp changes

in the GPP trend. The WBS site is constantly under water stress (Flerchinger et al., 2019). A key ecosystem process that mitigates such stress is changing plant community composition in response to interannual variation in precipitation (La Pierre and Smith, 2015; Wilcox et al., 2015). The representation of dryland plant communities (PFTs) in EDv2.2 is limited, which may lead to increased sensitivity of the model to precipitation variability.

Conclusion

In this study, we evaluated the performance of EDv2.2 for simulating GPP across an elevation gradient in a dryland study area. The main goal was to assess the capability of EDv2.2 in terms of GPP capacity and activity. We showed that the model is correctly sensitive to photosynthetic parameters in simulating GPP, whereas the model performs more poorly at higher elevations where GPP is higher. Introducing additional PFTs common in drylands (e.g., forbs) and modifying key processes such as plant hydraulics may solve the model inaccuracies. In addition, comparing phenometrics derived from model simulations and MODIS GPP showed some inconsistencies. We suggest this is due to issues of uncertainty in the remote sensing data (2000-2017), the phenology routine in EDv2.2, and the methodology to derive phenometrics. We also showed that the model is able to capture the long term trend of GPP by comparing simulations with remote sensing observations. However, the model exaggerates the greening-senescing events.

In summary, our study shows the potential of EDv2.2. to capture both GPP capacity and long term trends in a dryland site, particularly at lower elevations. Including additional PFTs and making structural modification (e.g. plant hydraulics, phenology) should increase the model's applicability at higher elevations. Future studies should focus on

combining the capabilities of EDv2.2, remote sensing, and EC flux towers through a data assimilation framework. New satellite products such as SIF have great potential to be integrated with DGVMs. Considering the heterogeneity of drylands across elevation gradients, increasing the number of EC tower sites for calibration and validation would also improve our understanding of GPP capacity and activity.

CHAPTER FOUR: REGIONAL SCALE DRYLAND VEGETATION
CLASSIFICATION WITH AND INTEGRATED LIDAR HYPERSPECTRAL
APPROACH

This chapter has been published as:

**H. Dashti, A. Poley, N. F. Glenn, N. Ilangakoon, L. Spaete, D. Roberts, J. Enterkine,
A. N. Flores, S. L. Ustin, and J. J. Mitchell, “Regional Scale Dryland
Vegetation Classification with an Integrated Lidar-Hyperspectral
Approach,” *Remote Sensing* , vol. 11, no. 18. 2019.**

Abstract

The sparse canopy cover and large contribution of bright background soil, along with the heterogeneous vegetation types in close proximity, are common challenges for mapping dryland vegetation with remote sensing. Consequently, the results of a single classification algorithm or one type of sensor to characterize dryland vegetation typically show low accuracy and lack robustness. In our study, we improved classification accuracy in a semi-arid ecosystem based on the use of vegetation optical (hyperspectral) and structural (lidar) information combined with the environmental characteristics of the landscape. To accomplish this goal, we used both spectral angle mapper (SAM) and multiple endmember spectral mixture analysis (MESMA) for optical vegetation classification. Lidar-derived maximum vegetation height and delineated riparian zones were then used to modify the optical classification. Incorporating the lidar information into the classification scheme increased the overall accuracy from 60% to 89%. Canopy

structure can have a strong influence on spectral variability and the lidar provided complementary information for SAM's sensitivity to shape but not magnitude of the spectra. Similar approaches to map large regions of drylands with low uncertainty may be readily implemented with unmixing algorithms applied to upcoming space-based imaging spectroscopy and lidar. This study advances our understanding of the nuances associated with mapping xeric and mesic regions, and highlights the importance of incorporating complementary algorithms and sensors to accurately characterize the heterogeneity of dryland ecosystems.

Introduction

Vegetation in semi-arid ecosystems (i.e. drylands) plays an important role in regulating the global carbon balance. As an example, 51% of the global net C sink during 2011 was attributed to three Southern Hemisphere semi-arid regions, with Australia being a global hotspot (Ahlström et al., 2015; Poulter et al., 2014). Yet, differentiating vegetation species and their respective roles in regional scale carbon dynamics in semi-arid and other dryland ecosystem types remain challenging. In many drylands, large environmental gradients (e.g. elevation) and variability in climate over landscapes with complex topography create conditions for disparate biomes to exist within close proximity to each other (Dufour et al., 2006; Hofer et al., 2008). Wetter, higher elevation sites and riparian areas are populated with alpine and deciduous vegetation, respectively, while drier, lower elevation landscapes can be dominated by shrubland vegetation. This heterogeneity makes mapping and quantifying vegetation species and structure inherently difficult at regional scales in drylands.

Hyperspectral remote sensing has been used to classify vegetation species within different biomes across the globe (Adam et al., 2010; Asner and Heidebrecht, 2002; Ballanti et al., 2016; George et al., 2014; Roth et al., 2015). Upcoming imaging spectroscopy sensors that are satellite-based (e.g. PRISMA (recently launched), EnMAP, SBG, and CHIME) or on the International Space Station (ISS) (e.g. DESIS, HISUI, and EMIT) will allow large area mapping. While hyperspectral remote sensing provides the advantage of narrow spectral bands across important regions for vegetation analysis, optical classification over large areas of drylands faces several challenges (Burai et al., 2015; Mitchell et al., 2016). The first challenge is spectral mixing, which is the contribution of different endmembers (EMs) to the total optical signal of a pixel received by the sensor (H Dashti et al., 2019; Silván-Cárdenas and Wang, 2010). The spectral mixing problem can be severe in drylands, and in particular, xeric areas where the vegetation cover is typically a mix of shrubs, soil, and grasses. Further, soil can be a mixture of inorganic and organic matter including litter and cryptobiotic crust. The influence of one EM may make the detection of other contributing classes challenging. For example, a recent study shows soil can contribute up to 95% to the total radiation in shrublands in the Great Basin, U.S. (H Dashti et al., 2019). The second challenge is in the spectral heterogeneity of these complex ecosystems over a large spatial extent. The spectral variability of vegetation is mainly a function of canopy structure (e.g. height and leaf area) and biochemistry, such as chlorophyll content (Asner, 1998; Hakkenberg et al., 2018; Ollinger, 2011; Roberts et al., 2004; Ustin et al., 2004). For example, different tree and shrub species might have similar spectral signatures due to complex interactions between canopy structure, canopy biochemistry, and light (Yuri Knyazikhin et al., 2013c; Wang et al., 2018). Moreover,

drylands are typically subject to environmental (e.g. precipitation, temperature, soil moisture, etc.) gradients that occur over fine spatial and temporal scales. In particular, the spectral heterogeneity becomes more complex at finer spatial resolution (e.g. 1×1 m pixel size). These environmental changes are mostly a function of the topography of the watershed. For example, in Great Basin semi-arid ecosystems in the western U.S., higher elevations typically receive more precipitation than lower elevations which favor denser vegetation composition. Even a small change in environmental conditions can have a large influence on vegetation traits (i.e. biochemistry and structure) and composition, which ultimately affects the optical signature. Thus, to fully solve the classification problem in drylands we need to consider canopy biochemistry, structure, and environmental variables. Such a task cannot be addressed using a single method or sensor and requires a framework that incorporates multiple methods and sensors. The main goal of this study is to develop a framework to map vegetation in drylands over a large landscape. Due to different optical properties we break down the study area into xeric and mesic regions. Following that, we discuss different remote sensing techniques that inform approaches that can be used for the classification of different xeric and mesic vegetation and soil.

In xeric regions, traditional pixel-based approaches may result in unreliable classifications due to the mixed pixels (Okin et al., 2001; Roberts et al., 1998; Silván-Cárdenas and Wang, 2010). An alternative is to use sub-pixel classification techniques (for a review refer to (Bioucas-Dias et al., 2012)). The main idea behind the unmixing approaches is to retrieve the fractional contribution of each EM in the total radiation. There are three different approaches for sub-pixel classification: 1) spectral mixture analysis (SMA), 2) regression methods, and 3) soft classification methods based on fuzzy

algorithms (Silván-Cárdenas and Wang, 2010). In this study, our focus is on spectral mixture analysis. The SMA methods are based on the inversion of a mixture model to retrieve the relative abundance of each endmember present in a pixel. Depending on assumptions such as linear or nonlinear spectral mixture and algorithm constraints, different SMA methods have been proposed (Borel and Gerstl, 1994; Chang and Heinz, 2000; Heinz and Chein-I-Chang, 2001; Li et al., 2015; Ray and Murray, 1996; Silván-Cárdenas and Wang, 2010). One of the widely adopted unmixing methods is multiple endmember spectral mixture analysis (MESMA), developed as an approach to deal with complex systems (Roberts et al., 1998). MESMA is sensitive to changes in the spectral albedo of an EM rather than its shape. In other words, MESMA is able to detect small changes in the magnitude of the spectra. This property makes it a suitable choice for drylands where the spectral variability of xeric areas are generally low.

In mesic sites where vegetation is dense, the problem of spectral mixing is not as severe as in xeric regions and pixel-based methods can be used for classification. A common pixel-based classification approach is the spectral angle mapper (SAM). The SAM compares image spectra with reference spectra, or endmembers, by mapping each spectrum as a vector in an n-dimensional space and measuring the angle between the two vectors. SAM only considers the shape and is insensitive to the magnitude of the spectra (Shanmugam and SrinivasaPerumal, 2014). SAM has been successfully used to classify evergreen and deciduous forest (Cho et al., 2010), juniper expansion (Yang et al., 2009), and over mountainous terrain (George et al., 2014). However, mesic classification becomes increasingly challenging over larger landscapes (e.g. several hundred km²) in heterogeneous systems. For example, several species can coexist in close proximity in

riparian zones. Moreover, riparian vegetation along the same stream corridor can be significantly different dependent upon elevation. This environmental gradient leads to increased spectral variability when a sufficiently large study area is observed on a single acquisition date (e.g. large-swath airborne applications and satellite-based observations). The high spectral variability of mesic regions makes classification a challenging task using just optical information.

Discrete return small footprint lidar has been successfully used in various vegetation mapping studies (e.g. (Dalponte and Coomes, 2016; Heinzl and Koch, 2011; Neuenschwander et al., 2009; Vaughn et al., 2012)); however, the data are typically insufficient for characterizing sparse semi-arid vegetation cover at high spatial resolutions (Glenn et al., 2011; Mitchell et al., 2015). Most recently, full-waveform lidar features such as pulse width, rise time, and derived height have been shown to improve discrimination of dryland components such as bare ground, grasses, and shrubs, but may need to be resampled to a coarser spatial resolution (e.g., 10 m x 10 m cells; (Ilangakoon et al., 2018)). Moreover, techniques for deriving full-waveform features are generally sophisticated and computationally expensive which limits their practical applications. However, in paying attention to environmental variability of drylands and changes in vegetation structure, one can observe that some simple lidar metrics provide complimentary information that can improve optical classifications. For example, previous studies have demonstrated that canopy structure provides a distinguishing difference between vegetation cover in riparian zones and other dense vegetation (Laslier et al., 2019; Villarreal et al., 2012), and canopy height is a particularly influential variable (Dowling and Accad, 2003). The ability of lidar metrics such as canopy height to characterize three-dimensional canopy structure provides

complementary information that improves land cover classifications (Mielcarek et al., 2018; Roussel et al., 2017). Moreover, lidar data can be used to derive a high spatial resolution digital elevation model (DEM) of the terrain. Important environmental variables that influence vegetation distribution patterns can be derived from a DEM. These variables include slope, aspect, and elevation. In addition, DEMs support flow accumulation modeling that can be combined with topographical information to delineate riparian zones. Topographic-based riparian delineations can be integrated into classification schemes to improve the accuracy of riparian vegetation mapping (Solomons et al., 2015; Tompalski et al., 2017). In this study, we focus on the use of state-of-the-art airborne lidar for improving confusion between riparian and other mesic vegetation classes. A combination of sensors and methods is recommended to properly address the limitations of hyperspectral and lidar datasets and the challenges of mesic and xeric regions in drylands (Glenn et al., 2016; Jeong et al., 2016; Narine et al., 2019; Zhang et al., 2013).

The goal of this study is to develop a straightforward framework to classify vegetation cover at a watershed scale (several hundred km²) in a dryland ecosystem. Our primary objective is to develop two reliable mapping products for a watershed located in the drylands of the western U.S. One product is an abundance map for xeric area components (soil, grass, and shrub) and the second product is a hard classification map for mesic areas (aspen, Douglas fir, juniper, and riparian). The main assumptions are: 1) hyperspectral information is sufficient for classification of xeric areas and 2) canopy structural information and riparian zone delineation from lidar improves optical classification in mesic areas. To accomplish our goal, we integrate the optical classification techniques SAM and MESMA, and lidar-derived products, to map soil, grass, shrub, aspen,

Douglas fir, juniper, and riparian vegetation across a watershed with a significant environmental gradient. This work builds on previous remote sensing of vegetation studies in the study area where the focus was on local scales or species-specific analyses (e.g. (Glenn et al., 2011; Ilangakoon et al., 2018; Mitchell et al., 2015; Olsoy et al., 2016; Spaete et al., 2011)). This work also builds on lessons learned from previous efforts to map vegetation structure (e.g. shrub biomass; (Li et al., 2017)) and biochemical information (i.e., sagebrush foliar N content; (H Dashti et al., 2019)) across the watershed by developing a framework that combines the lidar-derived structural variable canopy height with a hyperspectral unmixing approach to addressing fine scale combinations of soil with upland grasses and shrubs.

Materials and methods

This study was conducted in the Reynolds Creek Experimental Watershed (RCEW), located in the Owyhee Mountains, Idaho, U.S. (Figure 4.1). The RCEW encompasses 23,900 ha of land in a semi-arid ecosystem with an elevation gradient of 900–2200 m. Annual mean precipitation ranges from 250–1100 mm and increases linearly with elevation. The RCEW can be divided into three major biomes with boundaries that are defined by both sharp and gradual ecotones. Alpine vegetation dominates higher elevations in the southern portion of the watershed and consists primarily of quaking aspen (*Populus tremuloides*), Douglas fir (*Pseudotsuga menziesii*), and western juniper (*Juniperus occidentalis*) (Seyfried et al., 2001). There is a gradual transition into the lower elevations in the northern portion of the watershed from alpine vegetation to primarily Wyoming big sagebrush (*Artemisia tridentata* ssp. *wyomingensis*), low sagebrush (*Artemisia arbuscula*), rabbitbrush (*Ericameria nauseosa*), and bitterbrush (*Pushia tridentata*). This ecotone

contains western juniper that is expanding into lower elevation shrub communities. Common species in lower elevation grass communities include bluebunch wheatgrass (*Pseudoroegneria spicata*), needle and thread (*Hesperostipa comata*), western wheatgrass (*Pascopyrum smithii*), tapertip hawksbeard (*Crepis acuminata*), and yarrow (*Achillea millefolium*) (Pyke et al., 2015). The third biome within RCEW is defined as the riparian areas of the watershed. Common riparian vegetation in the region includes black cottonwood (*Populus trichocarpa*), coyote willow (*Salix exigua*), and peachleaf willow (*Salix amygdaloides*) (Council, 2002). Riparian regions transition gradually into alpine vegetation in the higher elevation areas; whereas the transition between riparian regions and shrublands is much sharper in the lower elevations and is defined by mesic areas (e.g. streams).

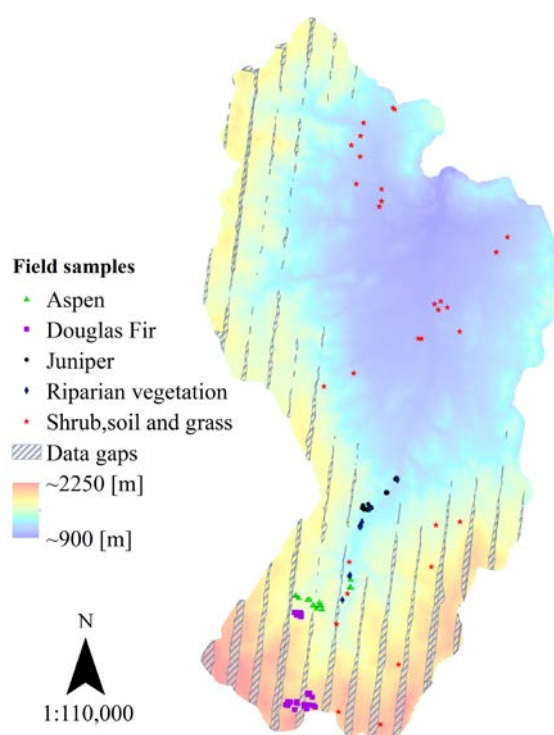


Figure 4.1 Elevation range and location of plots at Reynolds Creek Experimental Watershed, Idaho, U.S.

Field data were collected in 2014–2016 that support vegetation cover type mapping for RCEW. Shrub, grass, and soil cover was measured during September–November of 2014 and May and June of 2015 at 48 plots (10 × 10 m) distributed across a range of elevation, cover, and species. Sample point photo analysis (Booth et al., 2006) was used to classify each plot using a series of 20 photos taken every 2 m across each plot. We derived percent cover of soil and vegetation from the photo analysis, and used this information in endmember derivation and accuracy assessment for the xeric classification. A full description of the field data collection is presented in (H Dashti et al., 2019; Ilangakoon et al., 2018). Dominant vegetation cover for the collected plots included sagebrush, bitterbrush, rabbitbrush, mixed shrub, and grasses. In mesic regions where aspen, Douglas fir, juniper, and riparian classes dominated as patches in the landscape, we collected validation points during July of 2016 using a Topcon HiPer V Real Time Kinematic (RTK) GPS.

Imaging spectroscopy data were collected in June 2015 using NASA's Airborne Visible and Infrared Imaging Spectrometer Next Generation (AVIRIS-ng). AVIRIS-ng collects 432 spectral bands in the optical range (380–2500 nm) with a bandwidth of about 5 nm. The AVIRIS-ng Level 2 product, consisting of orthorectified surface reflectance atmospherically corrected with ATREM (Gao et al., 2009), was used for this study. A total of 15 AVIRIS-ng images were used to capture the full extent of RCEW. While maintaining a consistent spatial resolution during the data collection, approximately 17 km² (~6%) of the total watershed was not captured (Figure 3.1), resulting in data gaps between flight lines. These gaps were larger in the southern portion of the watershed where elevations are higher. Spectral bands were inspected for noise caused by atmospheric water absorption,

and 59 of the original bands were removed. These bands are located around the strong water absorption regions (1375 and 1875 nm). Bands less than 400 nm were also removed from the analysis due to low signal to noise in this region.

Full-waveform lidar data were acquired in August 2014, using the NASA Airborne Snow Observatory's Riegl LMS-Q1560 (Riegl Laser Measurement Systems GmbH, Horn, Austria). The scanner footprint is 20–60 cm with $\pm 30^\circ$ angle which results in 10–14 points/m². In total 40 lidar flight lines cover the study area. The hyperspectral data were resampled to 1×1 m pixels and co-registered to the lidar flightlines. The relative error of this registration is roughly half a pixel or 0.5 m.

Methods

Classification

Figure 4.2 shows the framework for classification of xeric and mesic vegetation in the study area. First, the mesic and xeric classes are classified using SAM and MESMA, respectively. We then use lidar to investigate the difference in canopy height among mesic classes and define a height threshold that can be used to separate mesic vegetation into aspen, Douglas fir, juniper, and riparian classes. We also use a DEM generated by lidar to map riparian zones. In the last step, we assign vegetation to mesic classes based on height thresholds and riparian zones.

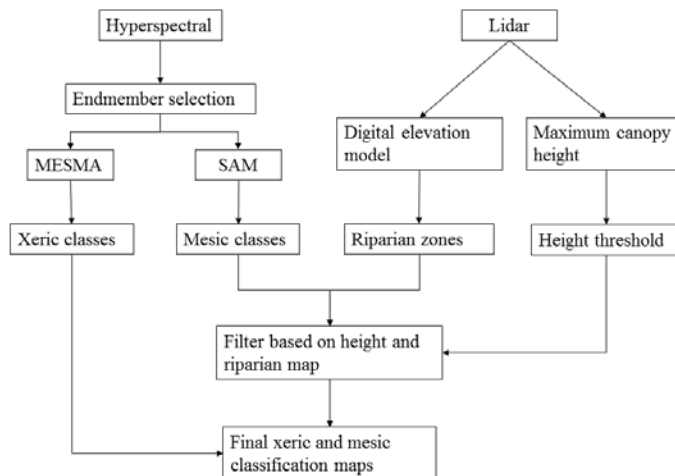


Figure 4.2 The classification framework using both hyperspectral and lidar data.

The open-source software Visualization and Image Processing for Environmental Research (VIPER) (Roberts et al., 2007) was used to compile and build EM bundles from the extracted spectra for each class from multiple images covering the study area. The VIPER toolbox calculates several statistical metrics including EM average root mean square error (EAR) and minimum average spectral angle (MASA) to highlight inter-class spectral variability and ultimately choose spectral bundles that best represent an entire class (for details, see (Dennison et al., 2004)). In general, smaller EAR and MASA values lead to endmembers that are better representative of the associated class (Dennison and Roberts, 2003). Spectral libraries were reduced to smaller subsets from the originally extracted spectra through an iterative process of taking the top spectra with the lowest EAR and MASA, running the classification process on several random validation plots, and removing spectra that performed poorly or were unused. This process was repeated until removing spectra decreased classification results. This procedure helped reduce computation time and the number of training samples used and maximized the number of validation samples. Table 4.1 shows the number of spectra per class that were delineated

in the initial spectral library, the number of samples used in the final classification, and the number of samples used for classification validation. EM bundle sizes ranged from 2–5 spectra per class. Field plots with spectra that were not used in the final spectral libraries were used to assess the classification accuracy.

Table 4.1. The number of ground validation points (represented by 1 m pixels) used for endmember (EM) derivation and classification accuracy assessment per class.

Classes	Image extracted EM	EM used in final classification	Validation samples
Aspen	1004	3	4816
Douglas fir	90	3	3947
Juniper	187	3	1409
Riparian	1316	5	3271
Shrub	328	7	3400
Grass	464	2	3400
Soil	100	3	3400

MESMA was used to map the xeric classes of shrub, grass, and soil. The output of MESMA is the relative abundance of each of these classes in each pixel. The MESMA parameters of minimum and maximum allowable EM fraction, minimum and maximum allowable shade fraction, and maximum allowable root mean square error (RMSE) were set as 0.0, 1.0, 0.0, 0.8, and 0.025, respectively. Model complexity, defined by the allowable number of EMs per pixel, was set to three; this includes the combination of two class EMs from the spectral library and a shade component, which was set to photometric (zero) for this study. Running MESMA with a three-EM model constraint was found to best represent the heterogeneity of the landscape that was observed in the field. The

absence of either grass or soil EM in the prediction of shrub abundance led to poor results in initial testing. A total of 56 models were used during the final unmixing process.

SAM was used to classify mesic classes: juniper, Douglas fir, aspen and riparian vegetation. Endmembers derived using VIPER were used for the SAM classification. The maximum allowable spectral angle for SAM was set to 0.1 radians. A post-classification 3×3-pixel moving average filter was performed to enhance spatial consistency of the SAM results.

Backscattered full waveform lidar signals were Gaussian decomposed to derive point clouds. A pulse width threshold was used to distinguish ground returns from vegetation returns. A thin plate smoothing function was applied to the ground returns to derive the DEM. The maximum height at each pixel (1 m×1 m) of the vegetation returns was used as the maximum vegetation height. The canopy height was extracted by subtracting the ground elevations from the maximum height using BCAL Lidar Tools (Streutker and Glenn, 2006). We used the method developed by (Montgomery and Dietrich, 1992) to extract the stream network from the DEM. Stream network extraction was implemented using the TauDEM toolbox in the ESRI ArcGIS software (Environmental Systems Research Institute, 2017). We delineated the riparian zone using the buffering technique based on the Strahler order of the stream (Salo et al., 2016). Following (Li and Nigh, 2011) for semi-arid ecosystems, we employed a buffer width of 15 m for stream order one, 35 m for stream orders two and three, and 70 m for stream orders larger than three. The canopy height distribution of each mesic class was extracted from the lidar data (Figure 4.3a) across the watershed. Results indicated that most misclassification was between riparian vegetation and aspen areas. Using the ksdensity

function in MATLAB (MathWorks, Inc; 2017), the probability density function (PDF) of height for these two classes was estimated and plotted (Figure 4.3b).

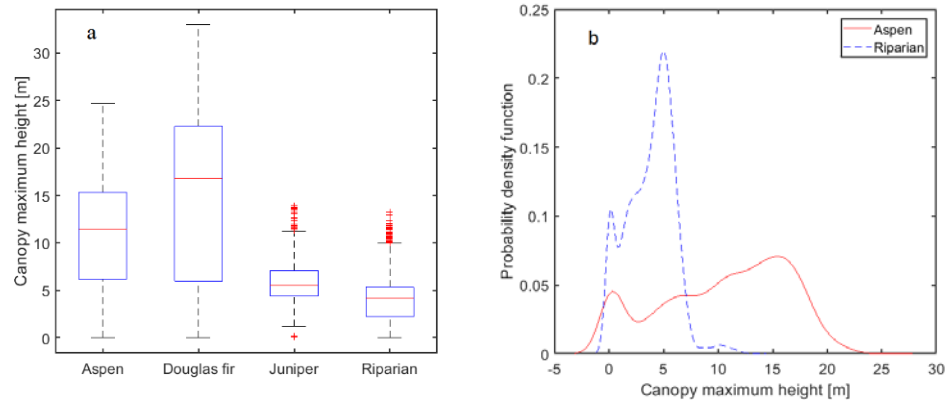


Figure 4.3 (a) Canopy maximum height distribution extracted from lidar and (b) probability density function for aspen and riparian classes.

The two classes can be reasonably distinguished using a ~ 7 m height threshold. Thus, in this study we determined the riparian class based on the SAM classification and locations within the riparian boundary and lower than 7 m height.

Classification accuracy assessment

MESMA produces abundances of multiple classes in a single pixel, a traditional confusion matrix cannot be directly applied to assess the accuracy. Silván-Cárdenas and Wang, 2008 (Silván-Cárdenas and Wang, 2008), developed a specialized confusion matrix that evaluates the performance of linear spectral unmixing techniques, termed sub-pixel confusion-uncertainty matrix (SCM). The SCM calculates the accuracy of sub-pixel estimates with the use of field measured class cover instead of determining if a location was correctly classified or not, as in a traditional confusion matrix. The method uses a composite operator, L_{njj} , to calculate the SCM:

$$L_{nij} = \begin{cases} \text{MIN}(c_{ni}, f_{nj}), & i = j \\ (c_{ni} - L_{nii}) \times \left[\frac{f_{nj} - L_{njj}}{\sum_{j=1}^k (f_{nj} - L_{njj})} \right], & i \neq j \end{cases} \quad (1)$$

where L is the specific cell in the SCM for pixel n, c is the class cover produced from the linear mixture model for pixel n, f is the field measure class cover for pixel n, k is the total number of classes, and i and j represent the row and column of the SCM, respectively. The SCM was calculated for each plot, then the resulting SCMs were averaged to produce a final SCM. Overall accuracy, user's and producer's accuracies were produced from the final SCM for the shrub, grass, and soil percent cover.

Accuracy assessment of the SAM classification was performed using the independent field validation data generated as part of the EM selection process in MESMA (Table 4.1). The SAM classification was evaluated using standard classification metrics from the confusion matrix (overall accuracy and user's and producer's accuracies). The producer's accuracy shows how often an observed class on the ground is correctly labeled in the final classification map and the user's accuracy indicates how often a class labeled on the map is found on the ground (Patel and Kaushal, 2010; Silván-Cárdenas and Wang, 2008).

Results

Classification

The final SCM for the MESMA accuracy results were produced using 44 field-measured cover estimates. Overall accuracy derived from the final SCM for the MESMA shrub, grass, and soil cover was 0.67 (Table 4.2). User's and producer's accuracies were primarily above roughly 60%. The producer's accuracy of the soil class was unusually low; whereas the shrub and grass classes were mapped with higher accuracy. Figure 4.4 shows the percent cover distribution of xeric classes over the region. The proportion of watershed

with dominant percent cover (class cover in pixel > 50%) for grass, shrub and soil is 22.4%, 38.2%, and 16.9%, respectively.

Table 4.2 User's and producer's accuracy for multiple endmember spectral mixture analysis (MESMA) classification.

Class	User's accuracy	Producer's accuracy
Shrub	0.59	0.99
Grass	0.76	0.79
Soil	0.99	0.35
Overall accuracy = 0.67		

The results for the mesic classification using the SAM method alone and with the lidar-derived information are presented in Table 4.3. The SAM classification without the lidar resulted in confusion between the aspen and riparian classes. However, incorporating the lidar-derived canopy height and riparian zones significantly improved the accuracy of these classes. The overall accuracy increased from 60% to 89%. The final mesic and xeric classification maps over the 23,900 ha region were then produced from the 1 m x 1 m pixels from our approach (Figure 4.5). The proportion of aspen, Douglas fir, juniper and riparian classes are respectively, 2.3%, 0.60%, 0.1%, and 1.5%, of the watershed.

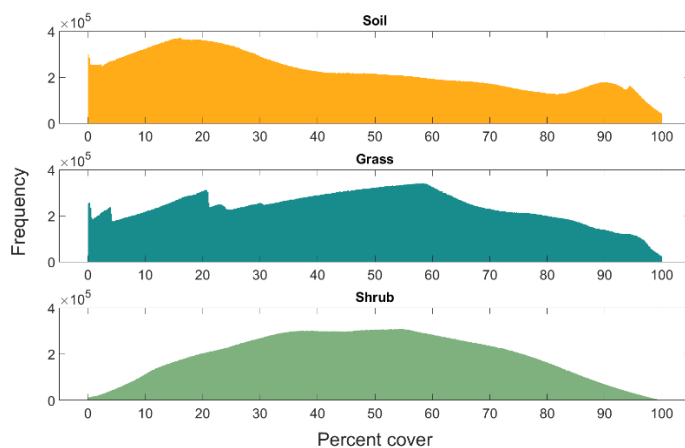


Figure 4.4 Distribution of xeric percent cover over the region.

Table 4.3 Confusion matrix for spectral angle mapper (SAM) results alone and with lidar-derived information.

		Ground Reference					Accuracy	
		Aspen	Riparian	Douglas fir	Juniper	Total	User's accuracy	Producer's accuracy
Classified	Aspen	2015	553	398	66	3032	0.66	0.44
	Riparian	2411	1806	130	5	4352	0.41	0.63
	Douglas fir	95	500	2014	100	2709	0.74	0.77
	Juniper	7	0	46	636	689	0.92	0.78
	Total	4528	2859	2588	807	10782	---	---
Overall accuracy = 0.60								
Classified incorporating lidar	Aspen	4298	128	398	66	4890	0.87	0.94
	Riparian	129	2718	130	5	2982	0.91	0.95
	Douglas fir	94	13	2014	100	2221	0.90	0.77
	Juniper	7	0	46	636	689	0.92	0.78
	Total	4528	2859	2588	807	10782	---	---
Overall accuracy = 0.89								

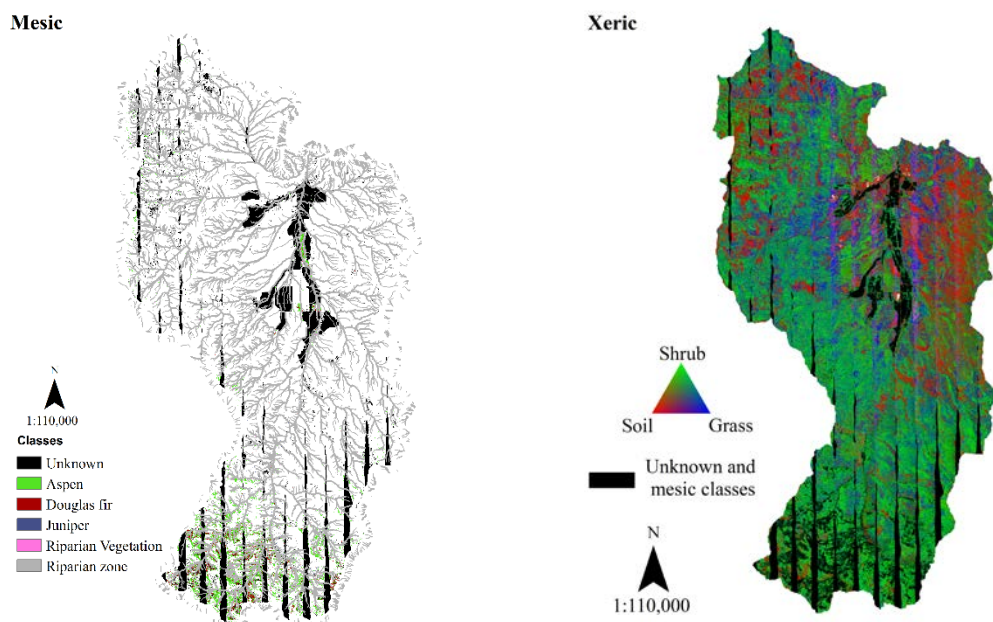


Figure 4.5 Final vegetation cover map of RCEW using SAM, MESMA, and lidar-derived products; (left) mesic classes and (right) xeric classes.

Discussion

Xeric classification

Using high spatial resolution imaging spectroscopy to classify tree and shrub species across ecotones in drylands is effective but has limitations where there is a complex intergrowth of spectrally-similar vegetation species and where there is significant soil exposure. The 67% overall accuracy of xeric classes shows that MESMA was successful in classifying sparse vegetation cover in this dryland watershed. The low producer's accuracy of the soil class indicates that MESMA did not perform well in classifying the reference soil class; whereas the high user's accuracy indicates that the majority of classified soil pixels are indeed soil on the ground. These results are likely representative of our high soil cover and the spectral confusion of soil that is often mixed with litter (non-photosynthetic vegetation). Regardless, our soil percent cover class can be dependably used. The high producer's accuracy and corresponding lower user's accuracy of the shrub

class indicates an over-classification of shrub within the study area. This may be attributed to the woody biomass of the shrubs, which results in a similar optical response to the mixture of litter and soil. Thus some soil plots with higher amounts of litter may be classified as shrub. This interpretation may also be used to understand the misclassification of the soil class (i.e. low producer's accuracy). We conclude that the misclassification in xeric areas likely occurs where shrubs have relatively lower photosynthetically-active biomass (i.e. higher woody biomass) and soil has high litter cover. This conclusion is consistent with a thorough physical analysis of the same area using physical radiative transfer modeling (H Dashti et al., 2019). Grasses were mapped surprisingly well at the sub-pixel level with the SCM accuracies. The strong results are likely due to the timing of the imagery (June) when grasses were still photosynthetically-active and thus differentiable from the litter and soil. Figure 3.4 demonstrates most pixels in the study area include shrub as an endmember, with a normal distribution and mean cover of ~45%. The latter is consistent with our overclassification of shrub cover. The distribution of soil and grass cover is more uniform than shrub cover in the classification, including pixels with low and high soil and grass cover.

Mesic classification

As expected, mesic classes cover a small portion of the watershed and are located mostly in higher elevations and along streams where environmental conditions such as precipitation, temperature, and soil moisture favor riparian and denser vegetation cover. SAM was able to distinguish classes that are both spectrally and structurally different (i.e., juniper and Douglas fir) but failed when vegetation is structurally different but spectrally similar (i.e., riparian vs. aspen). Consequently, the main source of classification error in

this study was the confusion between aspen trees and riparian vegetation in mesic areas. Vegetation species present within the riparian zones are driven by the surrounding environmental conditions including elevation, precipitation, and soil composition (Council, 2002; David et al., 2007; Patten, 1998). The favorable conditions of the riparian areas lead to the presence of multiple species in close proximity. Due to large environmental gradients observed within our study site, it is likely that the composition of vegetation species between riparian areas was also highly varied throughout the study area. At coarser scales (e.g. landscape scale) the influence of canopy structure on spectral variability may be greater than canopy biochemistry (Huang et al., 2007; Yuri Knyazikhin et al., 2013c; Wang et al., 2018). Thus, the complex structure of vegetation in riparian zones is the main reason for the spectral variability within this class in the region. Significant improvement of classifications using canopy height indicates that the structure of the riparian zone can be explained to a large extent by canopy height which is consistent with the findings of other studies as well (Arroyo et al., 2010; Hall et al., 2009; Wasser et al., 2013). Moreover, mapping riparian areas using lidar and incorporating it into classifications not only contributes to the improvement of the classification but also leads to ecologically meaningful results. For example, inspection of the SAM classification (alone) indicated that some pixels classified as riparian were distant from streams and on closer inspection were clearly not riparian vegetation. We should also note that there are multiple approaches for delineating riparian zones in semi-arid ecosystems (refer to (Salo et al., 2016) for a review), and the method and its performance should be evaluated with respect to the goals of the research. The buffering technique used in this study was appropriate for our mapping goals. Comparable results can be achieved using other lidar-

hyperspectral integration schemes such as the deep convolutional neural network (Ghamisi et al., 2017; Xu et al., 2018), support vector machines (Dalponte et al., 2008), or graph-based methods (Liao et al., 2015). However, these methods are not always straightforward and may need more calibration to build a robust classification model. There is no doubt that integrated lidar-hyperspectral classification leads to better results (Asner et al., 2008; Koetz et al., 2008; Liao et al., 2014; Xu et al., 2018). The framework and approach described here are straightforward to implement and interpret, and are consistent with our ecological understanding.

Lidar can also be used to improve spectral unmixing, such as in (Degerickx et al., 2019). This study demonstrated that lidar-derived height distributions used for endmember selection and as additional fractional constraints reduced the confusion between spectrally similar classes in an urban area. We did not use a similar approach because the main source of sub-pixel classification error was between shrub and soil classes, two classes that are not always easily distinguished in point cloud lidar data. In general, lidar do not provide the information to map sparse semi-arid vegetation cover at high spatial resolution. The point density (10–14 pts/m²) in this study was not able to fully distinguish ground from shrubs at 1×1 m grid sizes. Airborne lidar requires point aggregation to achieve sufficient density (e.g. 10×10 m cells in (Ilangakoon et al., 2018)) whereas spaceborne lidar (such as GEDI) require even larger cells to achieve point density for similar classification purposes. Thus, a combination of sensors and methods is recommended to properly address the limitations of hyperspectral and lidar datasets and the challenges of mesic and xeric regions in drylands (Glenn et al., 2016; Jeong et al., 2016; Narine et al., 2019; Zhang et al., 2013; Zhi et al., 2015).

We did not use MESMA for a mesic subpixel classification due to the high spectral variability in these regions. Our preliminary analysis indicated that one set of EMs selected for a tree class were very similar to another set of EMs for a different tree class (results not shown in this paper), which ultimately resulted in poor classification. Endmember variability is the main source of error in unmixing methods including MESMA (Bateson et al., 2000; Deng, 2015; Roberts et al., 1998). This problem is exacerbated at 1×1 m pixel sizes. Alternatively, the simple classification method of SAM informed by lidar produced accurate mesic maps. Due to the strong influence of canopy structure in the total reflected radiation, the spectral variability in dense vegetation cover is mostly in magnitude of the spectrum rather than its shape (Asner, 1998; Disney, 2016; Yuri Knyazikhin et al., 2013c; Ollinger, 2011). Thus lidar provides complementary information for SAM's sensitivity to shape (and insensitivity to magnitude) of the spectra.

The large number of AVIRIS-ng images used in this study is noteworthy. The 15 airborne images were collected over approximately two and a half hours to capture the full extent of the study area. During this time solar zenith angle changed from $\sim 22^\circ$ to $\sim 28^\circ$ for the first and last flight lines, respectively, and it is likely that illumination differences occurred. Hall et al. (Hall et al., 2008) reported changes in canopy reflectance due to solar illumination can occur during the sub-hourly scale. Additionally, illumination of vegetation was affected by shading caused by topographic features, surrounding vegetation and the distance of pixels from nadir. These shading factors would have also varied in intensity throughout the image collection. The sum of the soil, grass, and shrub fractions was more than unity in several pixels. The majority of which were located along flightline edges. While these issues are unavoidable when analyzing airborne imaging spectroscopy data at

the landscape scale, EM extraction from multiple images for a single class should be sufficient to capture the spectral variability present. In addition, in this study we assumed that the effect of the timing difference between imagery (lidar, imaging spectroscopy) was negligible in regards to changes in vegetation.

The framework developed in this study can be extended to the integration of new spaceborne hyperspectral (e.g. PRISMA) and laser altimetry (e.g. GEDI, ICESat-2). Furthermore, studies such as ours provides opportunities for precursor studies for new or proposed spaceborne hyperspectral sensors (e.g. DESIS, HISUI, EMIT on ISS or EnMAP, CHIME, SBG). The spatial resolution of these sensors are coarser, in comparison to data used in this study. For example, the PRISMA data are 30 m pixels and GEDI's footprint is roughly 25 m (Hancock et al., 2019). Thus, integration of these coarse resolution sensors using our framework is a promising approach for large scale (e.g. global scale) vegetation classification of drylands. The xeric and mesic vegetation maps may be used as baseline information for applications including restoration (Svejcar et al., 2017) and habitat suitability (Arkle et al., 2014) studies. Mesic vegetation mapping is particularly relevant for drylands where mesic resources drive habitat quality (Donnelly et al., 2016). Importantly, a significant use of vegetation maps in this study is expected from scientific communities seeking to understand carbon and water fluxes and storage within the study area (e.g. (Flerchinger et al., 2019; Renwick et al., 2019)).

Conclusion

Using a combination of optical and lidar data we were able to classify semi-arid vegetation types at high spatial resolution. The main source of misclassification was in mesic regions where riparian and aspen vegetation were confused. Incorporating canopy

height and riparian zone delineation significantly improved the mesic classification. MESMA classification of shrub-grass-soil mixed pixels leads to suitable accuracies; however, some misclassification between soil and shrub was observed. In order to reduce uncertainty in the classification of spectrally diverse areas such as drylands, an approach that employs spectral and structural observations along with requisite data processing methods is required. Different configurations of vegetation biochemical and biophysical characteristics may lead to similar spectrums across optical wavelengths. Our straightforward method provides accurate classification maps of xeric and mesic vegetation in drylands across large heterogeneous areas.

CHAPTER FIVE: CONCLUSION

In chapter two, I investigated the potential of hyperspectral remote sensing for estimating vegetation nitrogen. In my study, I linked the physical processes driving the canopy radiation budget to different machine learning techniques. My analysis showed that while cross-validated empirical estimations of N is possible, care should be taken in interpreting the results. I showed that in drylands, the influence of soil and canopy structure on the total canopy radiation budget is stronger than the N signal. My main contribution is in the debate over the role of confounding factors in retrieving foliar N from hyperspectral data (Fisher, 2009; Y Knyazikhin et al., 2013; Y Knyazikhin et al., 2013a, 2013b, Ollinger et al., 2009, 2008; Townsend et al., 2013). In this debate the focus is on the role of canopy structure in the radiation budget and consequently N estimation in a closed-canopy system. I added soil as another source of confounding factors in an open canopy system which, indeed, covers the majority of terrestrial ecosystems. These findings will enable us to robustly upscale different leaf scale processes to ecosystem-scales in different terrestrial ecosystems, which is one of the main goals of the NASA Terrestrial Ecology program. The results of this chapter is published in IEEE TGRS (H Dashti et al., 2019).

In chapter three I proposed an alternative method to remote sensing for photosynthesis studies based on DGVMs. In my study I calibrated the EDv2.2 model for drylands across an elevation gradient to estimate photosynthesis capacity and activity at the ecosystem scale (GPP). I showed that at low elevation sites, this model has great potential to capture GPP capacity and over long-term trends. Multiple contributions

resulted from this chapter. Calibrating these complex ecosystem models is a long-standing challenge in the community. PEST++ was recently introduced to the community as a calibration framework for EDv2.2. PEST++ is an efficient model-independent calibration method which returns the best parameter set with their confidence interval using mathematical regularization. I also discussed the potential pathways for improving model performance at higher elevations. The findings of this chapter directly contribute to another goal of the NASA Terrestrial Ecology program and project supporting this work, which is regional upscaling and predictive ecosystem modeling. This chapter is under review for a peer-reviewed journal.

And finally, in chapter three I showed that integrating hyperspectral and lidar data can improve vegetation mapping in drylands over large areas where both xeric and mesic vegetation exist. The main contribution of this study was the framework developed for such a task. Our framework is straightforward and easy to interpret, and consistent with our ecological understanding of vegetation in drylands. This framework can be easily adapted for mapping global scale vegetation in drylands. Significant use of vegetation maps produced in this study is expected from scientific communities seeking to understand carbon and water fluxes and storage within the study area. This chapter has been published in the journal *Remote Sensing* (Hamid Dashti et al., 2019).

The main products of my study advance the application of remote sensing to characterize dryland vegetation and model calibration in these ecosystems. As such, these studies have developed the foundation for exploring management scenarios of the sagebrush-steppe. Stakeholder agencies who may be interested in this work include the Bureau of Land Management, USDA Agricultural Research Service, United States

Department of Defense installations, and others working on the ecology of drylands. While the learning curve is steep for the EDv2.2 model, there are significant opportunities to pair scientists and land managers to develop meaningful scenarios for drylands. For example, the long- and short-term effects of wildfires or prescribed fires can be studied using GPP and other outputs. I should note that different ecosystem processes are mechanistically linked to each other in this model allowing long-term effects of disturbance.

Here I would like to discuss a theoretical and a practical line of research that my study provided the foundation for and subsequent studies can build upon. The theoretical component is related to the p-theory used in chapter two for physical analysis of the radiation budget. Under black soil conditions, p-theory is a function of canopy structure. Currently there is limited knowledge on estimating p-theory parameters such as recollision probability and escape factors from hyperspectral data. I suggest an alternative approach in estimating these parameters based on lidar data. Lidar is explicitly a function of canopy structure and, to my knowledge, its potential in p-theory has never been investigated. Integration of lidar and hyperspectral in the context of p-theory will improve our theoretical understanding of how light interacts with vegetation from leaf to canopy scales. Another important line of research is data assimilation. In this study we showed the potentials and limitations of both remote sensing and DGVMs. A proper data assimilation framework should overcome the majority of these limitations leading to better ecosystem-scale predictions. Recent advances in remote sensing technology such as solar-induced fluorescence, spaceborne hyperspectral and full-waveform lidar may provide more robust, continuous data which can be used for constraining DGVMs such as EDv2.2.

Below is a list of published peer-reviewed journal papers, conference presentations, and dataset produced fully or partially as a result of this study:

Peer-reviewed published manuscripts:

[1] H. Dashti, N. F. Glenn, S. Ustin, J. J. Mitchell, Y. Qi, N. T. Ilangakoon, A. N. Flores, J. L. Silván-Cárdenas, K. Zhao, L. P. Spaete, and M. de Graaff, “Empirical Methods for Remote Sensing of Nitrogen in Drylands May Lead to Unreliable Interpretation of Ecosystem Function,” *IEEE Trans. Geosci. Remote Sens.*, pp. 1–12, 2019.

[2] H. Dashti, A. Poley, N. F. Glenn, N. Ilangakoon, L. Spaete, D. Roberts, J. Enterkine, A. N. Flores, S. L. Ustin, and J. J. Mitchell, “Regional Scale Dryland Vegetation Classification with an Integrated Lidar-Hyperspectral Approach,” *Remote Sensing*, vol. 11, no. 18, 2019.

[3] K. Pandit, H. Dashti, N. F. Glenn, A. N. Flores, K. C. Maguire, D. J. Shinneman, G. N. Flerchinger, and A. W. Fellows, “Optimizing shrub (Sagebrush) parameters to estimate gross primary production of sagebrush-steppe ecosystem using Ecosystem Demography (ED2) model,” *Geosci. Model Dev.*, in press, 2019.

[4] N. T. Ilangakoon, N. F. Glenn, H. Dashti, T. H. Painter, T. D. Mikesell, L. P. Spaete, J. J. Mitchell, and K. Shannon, “Constraining plant functional types in a semi-arid ecosystem with waveform lidar,” *Remote Sens. Environ.*, vol. 209, pp. 497–509, 2018.

Manuscript in review:

[1] Hamid Dashti, Karun Pandit, Nancy F. Glenn, Douglas J. Shinneman, Gerald N. Flerchinger, Andrew A. Hudak, Marie Anne de Graaf, Alejandro

Flores, Susan Ustin, Nayani Ilangakoon, Aaron W. Fellows, “Performance of the Ecosystem Demography model (EDv2.2) in simulating photosynthesis capacity and activity along an elevation gradient in a dryland study area” In Review, 2019.

Book chapter:

[1] J. J. Mitchell, N. F. Glenn, K. M. Dahlin, N. T. Ilangakoon, H. Dashti, and M. C. Maloney, “Integrating Hyperspectral and LiDAR Data in the Study of Vegetation.,” in *Hyperspectral Remote Sensing of Vegetation (Volume I)*, II Ed., P. S. Thenkabail, J. G. Lyon, and A. Huete, Eds. London, New York: CRC Press-Taylor and Francis group, 2018, p. 449.

Datasets:

[1] N. F. Glenn, L. P. Spaete, R. Shrestha, A. Li, N. Ilangakoon, J. Mitchell, U. S. L, Y. Qi, H. Dashti, and K. Finan, “Shrubland Species Cover, Biometric, Carbon and Nitrogen Data, Southern Idaho, 2014.” ORNL Distributed Active Archive Center, 2017.

[2] H. Dashti, N. F. Glenn, L. P. Spaete, and N. Ilangakoon, “Hyperspectral Imagery from AVIRIS-NG for Sites in ID and CA, USA, 2014 and 2015.” ORNL Distributed Active Archive Center, 2018.

REFERENCES

- Adam, E., Mutanga, O., Rugege, D., 2010. Multispectral and hyperspectral remote sensing for identification and mapping of wetland vegetation: a review. *Wetl. Ecol. Manag.* 18, 281–296. doi:10.1007/s11273-009-9169-z
- Ahlström, A., Raupach, M.R., Schurgers, G., Smith, B., Arneeth, A., Jung, M., Reichstein, M., Canadell, J.G., Friedlingstein, P., Jain, A.K., Kato, E., Poulter, B., Sitch, S., Stocker, B.D., Viovy, N., Wang, Y.P., Wiltshire, A., Zaehle, S., Zeng, N., 2015. The dominant role of semi-arid ecosystems in the trend and variability of the land CO₂ sink. *Science* (80-.). 348, 895 LP-899.
- Altman, N., Krzywinski, M., 2015. Points of Significance: Association, correlation and causation. *Nat Meth* 12, 899–900.
- Antonarakis, A.S., Munger, J.W., Moorcroft, P.R., 2014. Imaging spectroscopy- and lidar-derived estimates of canopy composition and structure to improve predictions of forest carbon fluxes and ecosystem dynamics. *Geophys. Res. Lett.* 41, 2535–2542. doi:10.1002/2013GL058373
- Arkle, R.S., Pilliod, D.S., Hanser, S.E., Brooks, M.L., Chambers, J.C., Grace, J.B., Knutson, K.C., Pyke, D.A., Welty, J.L., Wirth, T.A., 2014. Quantifying restoration effectiveness using multi-scale habitat models: implications for sage-grouse in the Great Basin. *Ecosphere* 5, art31. doi:10.1890/ES13-00278.1
- Arroyo, L.A., Johansen, K., Armston, J., Phinn, S., 2010. Integration of LiDAR and QuickBird imagery for mapping riparian biophysical parameters and land cover types in Australian tropical savannas. *For. Ecol. Manage.* 259, 598–606. doi:https://doi.org/10.1016/j.foreco.2009.11.018
- Asner, G.P., 1998. Biophysical and Biochemical Sources of Variability in Canopy Reflectance. *Remote Sens. Environ.* 64, 234–253.

doi:[http://dx.doi.org/10.1016/S0034-4257\(98\)00014-5](http://dx.doi.org/10.1016/S0034-4257(98)00014-5)

- Asner, G.P., Anderson, C.B., Martin, R.E., Tupayachi, R., Knapp, D.E., Sinca, F., 2015a. Landscape biogeochemistry reflected in shifting distributions of chemical traits in the Amazon forest canopy. *Nat. Geosci.* 8, 567.
- Asner, G.P., Heidebrecht, K.B., 2002. Spectral unmixing of vegetation, soil and dry carbon cover in arid regions: Comparing multispectral and hyperspectral observations. *Int. J. Remote Sens.* 23, 3939–3958. doi:10.1080/01431160110115960
- Asner, G.P., Knapp, D.E., Kennedy-Bowdoin, T., Jones, M.O., Martin, R.E., Boardman, J., Hughes, R.F., 2008. Invasive species detection in Hawaiian rainforests using airborne imaging spectroscopy and LiDAR. *Remote Sens. Environ.* 112, 1942–1955. doi:<https://doi.org/10.1016/j.rse.2007.11.016>
- Asner, G.P., Martin, R.E., Anderson, C.B., Knapp, D.E., 2015b. Quantifying forest canopy traits: Imaging spectroscopy versus field survey. *Remote Sens. Environ.* 158, 15–27. doi:<https://doi.org/10.1016/j.rse.2014.11.011>
- Asner, G.P., Martin, R.E., Tupayachi, R., Anderson, C.B., Sinca, F., Carranza-Jiménez, L., Martinez, P., 2014. Amazonian functional diversity from forest canopy chemical assembly. *Proc. Natl. Acad. Sci.* 111, 5604 LP-5609.
- Asner, G.P., Wessman, C.A., Bateson, C.A., Privette, J.L., 2000. Impact of Tissue, Canopy, and Landscape Factors on the Hyperspectral Reflectance Variability of Arid Ecosystems. *Remote Sens. Environ.* 74, 69–84. doi:[http://dx.doi.org/10.1016/S0034-4257\(00\)00124-3](http://dx.doi.org/10.1016/S0034-4257(00)00124-3)
- Axelsson, C., Skidmore, A.K., Schlerf, M., Fauzi, A., Verhoef, W., 2013. Hyperspectral analysis of mangrove foliar chemistry using PLSR and support vector regression. *Int. J. Remote Sens.* 34, 1724–1743. doi:10.1080/01431161.2012.725958
- B., P., T., L., E., D.R., J.-L., W., N., G., M., V.M., 2006. Simplifying the interaction of land surfaces with radiation for relating remote sensing products to climate models. *J. Geophys. Res. Atmos.* 111. doi:10.1029/2005JD005952
- Badgley, G., Field, C.B., Berry, J.A., 2017. Canopy near-infrared reflectance and terrestrial photosynthesis. *Sci. Adv.* 3, e1602244. doi:10.1126/sciadv.1602244

- Baktashmotlagh, M., Harandi, M.T., Lovell, B.C., Salzmman, M., 2013. Unsupervised Domain Adaptation by Domain Invariant Projection, in: 2013 IEEE International Conference on Computer Vision. pp. 769–776. doi:10.1109/ICCV.2013.100
- Ballanti, L., Blesius, L., Hines, E., Kruse, B., 2016. Tree Species Classification Using Hyperspectral Imagery: A Comparison of Two Classifiers. *Remote Sens.* . doi:10.3390/rs8060445
- Bareinboim, E., Pearl, J., 2016. Causal inference and the data-fusion problem. *Proc. Natl. Acad. Sci.* 113, 7345 LP-7352.
- Bateson, C.A., Asner, G.P., Wessman, C.A., 2000. Endmember bundles: a new approach to incorporating endmember variability into spectral mixture analysis. *IEEE Trans. Geosci. Remote Sens.* 38, 1083–1094. doi:10.1109/36.841987
- Bernau, C., Riester, M., Boulesteix, A.-L., Parmigiani, G., Huttenhower, C., Waldron, L., Trippa, L., 2014. Cross-study validation for the assessment of prediction algorithms. *Bioinformatics* 30, i105–i112.
- Bioucas-Dias, J.M., Plaza, A., Dobigeon, N., Parente, M., Du, Q., Gader, P., Chanussot, J., 2012. Hyperspectral Unmixing Overview: Geometrical, Statistical, and Sparse Regression-Based Approaches. *IEEE J. Sel. Top. Appl. Earth Obs. Remote Sens.* 5, 354–379. doi:10.1109/JSTARS.2012.2194696
- Bonan, G., 2019. *Climate Change and Terrestrial Ecosystem Modeling*. Cambridge University Press, Cambridge. doi:DOI: 10.1017/9781107339217
- Booth, D.T., Cox, S.E., Berryman, R.D., 2006. Point Sampling Digital Imagery with “Samplepoint.” *Environ. Monit. Assess.* 123, 97–108. doi:10.1007/s10661-005-9164-7
- Borel, C.C., Gerstl, S.A.W., 1994. Nonlinear spectral mixing models for vegetative and soil surfaces. *Remote Sens. Environ.* 47, 403–416. doi:https://doi.org/10.1016/0034-4257(94)90107-4
- Botta, A., Viovy, N., Ciais, P., Friedlingstein, P., Monfray, P., 2000. A global prognostic scheme of leaf onset using satellite data. *Glob. Chang. Biol.* 6, 709–725. doi:10.1046/j.1365-2486.2000.00362.x

- Breiman, L., 2001. Random Forests. *Mach. Learn.* 45, 5–32.
doi:10.1023/A:1010933404324
- Burai, P., Deák, B., Valkó, O., Tomor, T., 2015. Classification of Herbaceous Vegetation Using Airborne Hyperspectral Imagery. *Remote Sens.* . doi:10.3390/rs70202046
- Campolongo, F., Cariboni, J., Saltelli, A., 2007. An effective screening design for sensitivity analysis of large models. *Environ. Model. Softw.* 22, 1509–1518.
doi:https://doi.org/10.1016/j.envsoft.2006.10.004
- Campolongo, F., Saltelli, A., 1997. Sensitivity analysis of an environmental model: an application of different analysis methods. *Reliab. Eng. Syst. Saf.* 57, 49–69.
doi:https://doi.org/10.1016/S0951-8320(97)00021-5
- Castaldi, F., Palombo, A., Santini, F., Pascucci, S., Pignatti, S., Casa, R., 2016. Evaluation of the potential of the current and forthcoming multispectral and hyperspectral imagers to estimate soil texture and organic carbon. *Remote Sens. Environ.* 179, 54–65. doi:https://doi.org/10.1016/j.rse.2016.03.025
- Castaldi, P.J., Dahabreh, I.J., Ioannidis, J.P.A., 2011. An empirical assessment of validation practices for molecular classifiers. *Brief. Bioinform.* 12, 189–202.
doi:10.1093/bib/bbq073
- Chang, C.-I., Heinz, D.C., 2000. Constrained subpixel target detection for remotely sensed imagery. *IEEE Trans. Geosci. Remote Sens.* 38, 1144–1159.
doi:10.1109/36.843007
- Chen, J., Rao, Y., Shen, M., Wang, C., Zhou, Y., Ma, L., Tang, Y., Yang, X., 2016. A Simple Method for Detecting Phenological Change From Time Series of Vegetation Index. *IEEE Trans. Geosci. Remote Sens.* 54, 3436–3449.
doi:10.1109/TGRS.2016.2518167
- Cho, M.A., Debba, P., Mathieu, R., Naidoo, L., Aardt, J. van, Asner, G.P., 2010. Improving Discrimination of Savanna Tree Species Through a Multiple-Endmember Spectral Angle Mapper Approach: Canopy-Level Analysis. *IEEE Trans. Geosci. Remote Sens.* 48, 4133–4142. doi:10.1109/TGRS.2010.2058579
- Concilio, A.L., Loik, M.E., Belnap, J., 2013. Global change effects on *Bromus tectorum*

- L. (Poaceae) at its high-elevation range margin. *Glob. Chang. Biol.* 19, 161–172. doi:10.1111/gcb.12032
- Council, N.R., 2002. *Riparian Areas: Functions and Strategies for Management*. The National Academies Press, Washington, DC. doi:10.17226/10327
- Curran, P.J., 1989. Remote sensing of foliar chemistry. *Remote Sens. Environ.* 30, 271–278. doi:http://dx.doi.org/10.1016/0034-4257(89)90069-2
- Curran, P.J., Dungan, J.L., Peterson, D.L., 2001. Estimating the foliar biochemical concentration of leaves with reflectance spectrometry: Testing the Kokaly and Clark methodologies. *Remote Sens. Environ.* 76, 349–359. doi:https://doi.org/10.1016/S0034-4257(01)00182-1
- Dahlin, K.M., Asner, G.P., Field, C.B., 2013. Environmental and community controls on plant canopy chemistry in a Mediterranean-type ecosystem. *Proc. Natl. Acad. Sci.* 110, 6895 LP-6900.
- Dalponte, M., Bruzzone, L., Gianelle, D., 2008. Fusion of Hyperspectral and LIDAR Remote Sensing Data for Classification of Complex Forest Areas. *IEEE Trans. Geosci. Remote Sens.* 46, 1416–1427. doi:10.1109/TGRS.2008.916480
- Dalponte, M., Coomes, D.A., 2016. Tree-centric mapping of forest carbon density from airborne laser scanning and hyperspectral data. *Methods Ecol. Evol.* 7, 1236–1245. doi:10.1111/2041-210X.12575
- Dashti, H., Glenn, N.F., Spaete, L.P., Ilangakoon, N., 2018. Hyperspectral Imagery from AVIRIS-NG for Sites in ID and CA, USA, 2014 and 2015. doi:10.3334/ornldaac/1533
- Dashti, H., Glenn, N.F., Ustin, S., Mitchell, J.J., Qi, Y., Ilangakoon, N.T., Flores, A.N., Silván-Cárdenas, J.L., Zhao, K., Spaete, L.P., Graaff, M. de, 2019. Empirical Methods for Remote Sensing of Nitrogen in Drylands May Lead to Unreliable Interpretation of Ecosystem Function. *IEEE Trans. Geosci. Remote Sens.* 1–12. doi:10.1109/TGRS.2018.2889318
- Dashti, H., Poley, A., F. Glenn, N., Ilangakoon, N., Spaete, L., Roberts, D., Enterkine, J., N. Flores, A., L. Ustin, S., J. Mitchell, J., 2019. Regional Scale Dryland Vegetation

- Classification with an Integrated Lidar-Hyperspectral Approach. *Remote Sens.* .
doi:10.3390/rs11182141
- David, R., Patricia, H., Karen, E., Susan, G., Juliet, S., Steven, K., Petr, P., Richard, H.,
2007. Riparian vegetation: degradation, alien plant invasions, and restoration
prospects. *Divers. Distrib.* 13, 126–139. doi:10.1111/j.1366-9516.2006.00314.x
- Davidson, E., Lefebvre, P.A., Brando, P.M., Ray, D.M., Trumbore, S.E., Solorzano, L.A.,
Ferreira, J.N., Bustamante, M.M.D., Nepstad, D.C., 2011. Carbon Inputs and Water
Uptake in Deep Soils of an Eastern Amazon Forest. *For. Sci.* 57, 51–58.
- Dawson, T.P., Curran, P.J., North, P.R.J., Plummer, S.E., 1999. The Propagation of
Foliar Biochemical Absorption Features in Forest Canopy Reflectance: A
Theoretical Analysis. *Remote Sens. Environ.* 67, 147–159.
doi:http://dx.doi.org/10.1016/S0034-4257(98)00081-9
- Degerickx, J., Roberts, D.A., Somers, B., 2019. Enhancing the performance of Multiple
Endmember Spectral Mixture Analysis (MESMA) for urban land cover mapping
using airborne lidar data and band selection. *Remote Sens. Environ.* 221, 260–273.
doi:https://doi.org/10.1016/j.rse.2018.11.026
- Deng, C., 2015. Incorporating Endmember Variability into Linear Unmixing of Coarse
Resolution Imagery: Mapping Large-Scale Impervious Surface Abundance Using a
Hierarchically Object-Based Spectral Mixture Analysis. *Remote Sens.* .
doi:10.3390/rs70709205
- Dennison, P.E., Halligan, K.Q., Roberts, D.A., 2004. A comparison of error metrics and
constraints for multiple endmember spectral mixture analysis and spectral angle
mapper. *Remote Sens. Environ.* 93, 359–367.
doi:https://doi.org/10.1016/j.rse.2004.07.013
- Dennison, P.E., Roberts, D.A., 2003. Endmember selection for multiple endmember
spectral mixture analysis using endmember average RMSE. *Remote Sens. Environ.*
87, 123–135. doi:https://doi.org/10.1016/S0034-4257(03)00135-4
- Dietze, M.C., Serbin, S.P., Davidson, C., Desai, A.R., Feng, X., Kelly, R., Kooper, R.,
LeBauer, D., Mantooh, J., McHenry, K., Wang, D., 2014. A quantitative assessment

- of a terrestrial biosphere model's data needs across North American biomes. *J. Geophys. Res. Biogeosciences* 119, 286–300. doi:10.1002/2013JG002392
- Disney, M., 2016. Remote Sensing of Vegetation: Potentials, Limitations, Developments and Applications BT - Canopy Photosynthesis: From Basics to Applications, in: Hikosaka, K., Niinemets, Ü., Anten, N.P.R. (Eds.), . Springer Netherlands, Dordrecht, pp. 289–331. doi:10.1007/978-94-017-7291-4_11
- Doherty, J., 2005. Model Independent Parameter Estimation. fifth edition of user manual. Brisbane, Australia.
- Donnelly, J.P., Naugle, D.E., Hagen, C.A., Maestas, J.D., 2016. Public lands and private waters: scarce mesic resources structure land tenure and sage-grouse distributions. *Ecosphere* 7, e01208. doi:10.1002/ecs2.1208
- Dorji, T., Moe, S.R., Klein, J.A., Totland, Ø., 2014. Plant Species Richness, Evenness, and Composition along Environmental Gradients in an Alpine Meadow Grazing Ecosystem in Central Tibet, China. *Arctic, Antarct. Alp. Res.* 46, 308–326. doi:10.1657/1938-4246-46.2.308
- Dowling, R., Accad, A., 2003. Vegetation classification of the riparian zone along the Brisbane River, Queensland, Australia, using light detection and ranging (lidar) data and forward looking digital video. *Can. J. Remote Sens.* 29, 556–563. doi:10.5589/m03-029
- Dufour, A., Gadallah, F., Wagner, H.H., Guisan, A., Buttler, A., 2006. Plant Species Richness and Environmental Heterogeneity in a Mountain Landscape: Effects of Variability and Spatial Configuration. *Ecography (Cop.)*. 29, 573–584.
- Evans, R.D., Black, R.A., 1993. Growth, Photosynthesis, and Resource Investment for Vegetative and Reproductive Modules of *Artemisia Tridentata*. *Ecology* 74, 1516–1528. doi:10.2307/1940079
- Ewald, M., Aerts, R., Lenoir, J., Fassnacht, F.E., Nicolas, M., Skowronek, S., Piat, J., Honnay, O., Garzón-López, C.X., Feilhauer, H., Van De Kerchove, R., Somers, B., Hattab, T., Rocchini, D., Schmidtlein, S., 2018a. LiDAR derived forest structure data improves predictions of canopy N and P concentrations from imaging

- spectroscopy. *Remote Sens. Environ.* 211, 13–25.
doi:<https://doi.org/10.1016/j.rse.2018.03.038>
- Ewald, M., Aerts, R., Lenoir, J., Fassnacht, F.E., Nicolas, M., Skowronek, S., Piat, J., Honnay, O., Garzón-López, C.X., Feilhauer, H., Van De Kerchove, R., Somers, B., Hattab, T., Rocchini, D., Schmidtlein, S., 2018b. LiDAR derived forest structure data improves predictions of canopy N and P concentrations from imaging spectroscopy. *Remote Sens. Environ.* 211, 13–25.
doi:<https://doi.org/10.1016/j.rse.2018.03.038>
- Fang, Q., Ma, L., Harmel, D.R., Yu, Q., Sima, W.M., Bartling, N.S.P., Malone, W.R., Nolan, T.B., Doherty, J., 2019. Uncertainty of CERES-Maize Calibration under Different Irrigation Strategies Using PEST Optimization Algorithm. *Agron.* .
doi:[10.3390/agronomy9050241](https://doi.org/10.3390/agronomy9050241)
- Farquhar, G.D., von Caemmerer, S., Berry, J.A., 1980. A biochemical model of photosynthetic CO₂ assimilation in leaves of C₃ species. *Planta* 149, 78–90.
doi:[10.1007/BF00386231](https://doi.org/10.1007/BF00386231)
- Feilhauer, H., Asner, G.P., Martin, R.E., 2015. Multi-method ensemble selection of spectral bands related to leaf biochemistry. *Remote Sens. Environ.* 164, 57–65.
doi:[10.1016/j.rse.2015.03.033](https://doi.org/10.1016/j.rse.2015.03.033)
- Fellows, A.W., Flerchinger, G.N., Seyfried, M.S., Lohse, K., 2017. Data for Partitioned Carbon and Energy Fluxes within the Reynolds Creek Critical Zone Observatory [Data Set].
- Feng, W., Guo, B.-B., Wang, Z.-J., He, L., Song, X., Wang, Y.-H., Guo, T.-C., 2014. Measuring leaf nitrogen concentration in winter wheat using double-peak spectral reflection remote sensing data. *F. Crop. Res.* 159, 43–52.
doi:<http://dx.doi.org/10.1016/j.fcr.2014.01.010>
- Fer, I., Kelly, R., Moorcroft, P.R., Richardson, A.D., Cowdery, E.M., Dietze, M.C., 2018. Linking big models to big data: efficient ecosystem model calibration through Bayesian model emulation. *Biogeosciences* 15, 5801–5830. doi:[10.5194/bg-15-5801-2018](https://doi.org/10.5194/bg-15-5801-2018)

- Feret, J.-B., François, C., Asner, G.P., Gitelson, A.A., Martin, R.E., Bidel, L.P.R., Ustin, S.L., le Maire, G., Jacquemoud, S., 2008. PROSPECT-4 and 5: Advances in the leaf optical properties model separating photosynthetic pigments. *Remote Sens. Environ.* 112, 3030–3043. doi:<http://dx.doi.org/10.1016/j.rse.2008.02.012>
- Fisher, J.B., 2009. Canopy nitrogen and albedo from remote sensing: What exactly are we seeing? *Proc. Natl. Acad. Sci.* 106, E16 LP-E16.
- Fisher, R.A., Koven, C.D., Anderegg, W.R.L., Christoffersen, B.O., Dietze, M.C., Farrior, C.E., Holm, J.A., Hurtt, G.C., Knox, R.G., Lawrence, P.J., Lichstein, J.W., Longo, M., Matheny, A.M., Medvigy, D., Muller-Landau, H.C., Powell, T.L., Serbin, S.P., Sato, H., Shuman, J.K., Smith, B., Trugman, A.T., Viskari, T., Verbeeck, H., Weng, E., Xu, C., Xu, X., Zhang, T., Moorcroft, P.R., 2018. Vegetation demographics in Earth System Models: A review of progress and priorities. *Glob. Chang. Biol.* doi:10.1111/gcb.13910
- Fisher, R.A., Muszala, S., Verstein, M., Lawrence, P., Xu, C., McDowell, N.G., Knox, R.G., Koven, C., Holm, J., Rogers, B.M., Spessa, A., Lawrence, D., Bonan, G., 2015. Taking off the training wheels: the properties of a dynamic vegetation model without climate envelopes, CLM4.5(ED). *Geosci. Model Dev.* 8, 3593–3619. doi:10.5194/gmd-8-3593-2015
- Flerchinger, G.N., Fellows, A.W., Seyfried, M.S., Clark, P.E., Lohse, K.A., 2019. Water and Carbon Fluxes Along an Elevational Gradient in a Sagebrush Ecosystem. *Ecosystems*. doi:10.1007/s10021-019-00400-x
- Flerchinger, G.N., Marks, D., Reba, M.L., Yu, Q., Seyfried, M.S., 2010. Surface fluxes and water balance of spatially varying vegetation within a small mountainous headwater catchment. *Hydrol. Earth Syst. Sci.* 14, 965–978. doi:10.5194/hess-14-965-2010
- Flores, A., Masarik, M., Watson, K., 2016. A 30-Year, Multi-Domain High-Resolution Climate Simulation Dataset for the Interior Pacific Northwest and Southern Idaho.
- Forkel, M., Migliavacca, M., Thonicke, K., Reichstein, M., Schaphoff, S., Weber, U., Carvalhais, N., 2015a. Codominant water control on global interannual variability

- and trends in land surface phenology and greenness. *Glob. Chang. Biol.* 21, 3414–3435. doi:10.1111/gcb.12950
- Forkel, M., Migliavacca, M., Thonicke, K., Reichstein, M., Schaphoff, S., Weber, U., Carvalhais, N., 2015b. Codominant water control on global interannual variability and trends in land surface phenology and greenness. *Glob. Chang. Biol.* 21, 3414–3435. doi:10.1111/gcb.12950
- Ganin, Y., Ustinova, E., Ajakan, H., Germain, P., Larochelle, H., Laviolette, F., Marchand, M., Lempitsky, V., 2015. Domain-Adversarial Training of Neural Networks.
- Gao, B.-C., Goetz, A.F.H., 1995. Retrieval of equivalent water thickness and information related to biochemical components of vegetation canopies from AVIRIS data. *Remote Sens. Environ.* 52, 155–162. doi:http://dx.doi.org/10.1016/0034-4257(95)00039-4
- Gao, B.-C., Montes, M.J., Davis, C.O., Goetz, A.F.H., 2009. Atmospheric correction algorithms for hyperspectral remote sensing data of land and ocean. *Remote Sens. Environ.* 113, S17–S24. doi:https://doi.org/10.1016/j.rse.2007.12.015
- Gao, Q., Kang, M., Xu, H., Jiang, Y., Yang, J., 2010. Optimization of land use structure and spatial pattern for the semi-arid loess hilly–gully region in China. *CATENA* 81, 196–202. doi:https://doi.org/10.1016/j.catena.2010.03.002
- George, R., Padalia, H., Kushwaha, S.P.S., 2014. Forest tree species discrimination in western Himalaya using EO-1 Hyperion. *Int. J. Appl. Earth Obs. Geoinf.* 28, 140–149. doi:https://doi.org/10.1016/j.jag.2013.11.011
- Georgescu, M., Miguez-Macho, G., Steyaert, L.T., Weaver, C.P., 2009. Climatic effects of 30 years of landscape change over the Greater Phoenix, Arizona, region: 1. Surface energy budget changes. *J. Geophys. Res. Atmos.* 114. doi:10.1029/2008JD010745
- Ghamisi, P., Höfle, B., Zhu, X.X., 2017. Hyperspectral and LiDAR Data Fusion Using Extinction Profiles and Deep Convolutional Neural Network. *IEEE J. Sel. Top. Appl. Earth Obs. Remote Sens.* 10, 3011–3024. doi:10.1109/JSTARS.2016.2634863

- Glenn, N.F., Neuenschwander, A., Vierling, L.A., Spaete, L., Li, A., Shinneman, D.J., Pilliod, D.S., Arkle, R.S., McIlroy, S.K., 2016. Landsat 8 and ICESat-2: Performance and potential synergies for quantifying dryland ecosystem vegetation cover and biomass. *Remote Sens. Environ.* 185, 233–242. doi:<https://doi.org/10.1016/j.rse.2016.02.039>
- Glenn, N.F., Spaete, L.P., Sankey, T.T., Derryberry, D.R., Hardegree, S.P., Mitchell, J.J., 2011. Errors in LiDAR-derived shrub height and crown area on sloped terrain. *J. Arid Environ.* 75, 377–382. doi:<https://doi.org/10.1016/j.jaridenv.2010.11.005>
- Glenn, N.F., Spaete, L.P., Shrestha, R., Li, A., Ilangakoon, N., Mitchell, J., L, U.S., Qi, Y., Dashti, H., Finan, K., 2017. Shrubland Species Cover, Biometric, Carbon and Nitrogen Data, Southern Idaho, 2014. doi:10.3334/ornl daac/1503
- Global Drylands: A UN system-wide response, 2011.
- Gränsbo, k, Almgren, P., Sjögren, M., Smith J, G., Engström, G., Hedblad, B., Melander, O., 2013. Chromosome 9p21 genetic variation explains 13% of cardiovascular disease incidence but does not improve risk prediction. *J. Intern. Med.* 274, 233–240. doi:10.1111/joim.12063
- Grossman, Y.L., Ustin, S.L., Jacquemoud, S., Sanderson, E.W., Schmuck, G., Verdebout, J., 1996. Critique of stepwise multiple linear regression for the extraction of leaf biochemistry information from leaf reflectance data. *Remote Sens. Environ.* 56, 182–193. doi:[http://dx.doi.org/10.1016/0034-4257\(95\)00235-9](http://dx.doi.org/10.1016/0034-4257(95)00235-9)
- Hakkenberg, C.R., Peet, R.K., Urban, D.L., Song, C., 2018. Modeling plant composition as community continua in a forest landscape with LiDAR and hyperspectral remote sensing. *Ecol. Appl.* 28, 177–190. doi:10.1002/eap.1638
- Hall, F.G., Hilker, T., Coops, N.C., Lyapustin, A., Huemmrich, K.F., Middleton, E., Margolis, H., Drolet, G., Black, T.A., 2008. Multi-angle remote sensing of forest light use efficiency by observing PRI variation with canopy shadow fraction. *Remote Sens. Environ.* 112, 3201–3211. doi:<http://dx.doi.org/10.1016/j.rse.2008.03.015>
- Hall, R.K., Watkins, R.L., Heggem, D.T., Jones, K.B., Kaufmann, P.R., Moore, S.B.,

- Gregory, S.J., 2009. Quantifying structural physical habitat attributes using LIDAR and hyperspectral imagery. *Environ. Monit. Assess.* 159, 63. doi:10.1007/s10661-008-0613-y
- Hancock, S., Armston, J., Hofton, M., Sun, X., Tang, H., Duncanson, L.I., Kellner, J.R., Dubayah, R., 2019. The GEDI Simulator: A Large-Footprint Waveform Lidar Simulator for Calibration and Validation of Spaceborne Missions. *Earth Sp. Sci.* 6, 294–310. doi:10.1029/2018EA000506
- Hansen, N., 2016. *The CMA Evolution Strategy: A Tutorial*.
- Hansen, N., Müller, S.D., Koumoutsakos, P., 2003. Reducing the Time Complexity of the Derandomized Evolution Strategy with Covariance Matrix Adaptation (CMA-ES). *Evol. Comput.* 11, 1–18. doi:10.1162/106365603321828970
- Hawkins, B.A., Field, R., Cornell, H. V, Currie, D.J., Guégan, J.-F., Kaufman, D.M., Kerr, J.T., Mittelbach, G.G., Oberdorff, T., O'Brien, E.M., Porter, E.E., Turner, J.R.G., 2003. ENERGY, WATER, AND BROAD-SCALE GEOGRAPHIC PATTERNS OF SPECIES RICHNESS. *Ecology* 84, 3105–3117. doi:10.1890/03-8006
- Heinz, D.C., Chein-I-Chang, 2001. Fully constrained least squares linear spectral mixture analysis method for material quantification in hyperspectral imagery. *IEEE Trans. Geosci. Remote Sens.* 39, 529–545. doi:10.1109/36.911111
- Heinzel, J., Koch, B., 2011. Exploring full-waveform LiDAR parameters for tree species classification. *Int. J. Appl. Earth Obs. Geoinf.* 13, 152–160. doi:https://doi.org/10.1016/j.jag.2010.09.010
- Herrmann, I., Pimstein, A., Karnieli, A., Cohen, Y., Alchanatis, V., Bonfil, D.J., 2011. LAI assessment of wheat and potato crops by VEN μ S and Sentinel-2 bands. *Remote Sens. Environ.* 115, 2141–2151. doi:10.1016/j.rse.2011.04.018
- Hofer, G., Wagner, H.H., Herzog, F., Edwards, P.J., 2008. Effects of Topographic Variability on the Scaling of Plant Species Richness in Gradient Dominated Landscapes. *Ecography (Cop.)*. 31, 131–139.
- Holben, B.N., 1986. Characteristics of maximum-value composite images from temporal

- AVHRR data. *Int. J. Remote Sens.* 7, 1417–1434. doi:10.1080/01431168608948945
- Homolová, L., Malenovský, Z., Clevers, J.G.P.W., García-Santos, G., Schaepman, M.E., 2013a. Review of optical-based remote sensing for plant trait mapping. *Ecol. Complex.* 15, 1–16. doi:http://dx.doi.org/10.1016/j.ecocom.2013.06.003
- Homolová, L., Malenovský, Z., Clevers, J.G.P.W., García-Santos, G., Schaepman, M.E., 2013b. Review of optical-based remote sensing for plant trait mapping. *Ecol. Complex.* 15, 1–16. doi:10.1016/j.ecocom.2013.06.003
- Hsieh, N.-H., Reisfeld, B., Bois, F.Y., Chiu, W.A., 2018. Applying a Global Sensitivity Analysis Workflow to Improve the Computational Efficiencies in Physiologically-Based Pharmacokinetic Modeling. *Front. Pharmacol.* 9, 588. doi:10.3389/fphar.2018.00588
- Huang, D., Knyazikhin, Y., Dickinson, R.E., Rautiainen, M., Stenberg, P., Disney, M., Lewis, P., Cescatti, A., Tian, Y., Verhoef, W., Martonchik, J. V., Myneni, R.B., 2007. Canopy spectral invariants for remote sensing and model applications. *Remote Sens. Environ.* 106, 106–122. doi:http://dx.doi.org/10.1016/j.rse.2006.08.001
- Huang, J., Ji, M., Xie, Y., Wang, S., He, Y., Ran, J., 2016. Global semi-arid climate change over last 60 years. *Clim. Dyn.* 46, 1131–1150. doi:10.1007/s00382-015-2636-8
- Huang, J., Smola, A.J., Gretton, A., Borgwardt, K.M., Schölkopf, B., n.d. Correcting Sample Selection Bias by Unlabeled Data.
- Huang, Z., Turner, B.J., Dury, S.J., Wallis, I.R., Foley, W.J., 2004. Estimating foliage nitrogen concentration from HYMAP data using continuum removal analysis. *Remote Sens. Environ.* 93, 18–29. doi:10.1016/j.rse.2004.06.008
- Ilangakoon, N.T., Glenn, N.F., Dashti, H., Painter, T.H., Mikesell, T.D., Spaete, L.P., Mitchell, J.J., Shannon, K., 2018. Constraining plant functional types in a semi-arid ecosystem with waveform lidar. *Remote Sens. Environ.* 209, 497–509. doi:https://doi.org/10.1016/j.rse.2018.02.070
- Integrated Rangeland Fire Management, 2016. The Integrated Rangeland Fire Management Strategy Actionable Science Plan.

- Janse, J.H., Scheffer, M., Lijklema, L., Van Liere, L., Sloot, J.S., Mooij, W.M., 2010. Estimating the critical phosphorus loading of shallow lakes with the ecosystem model PCLake: Sensitivity, calibration and uncertainty. *Ecol. Modell.* 221, 654–665. doi:<https://doi.org/10.1016/j.ecolmodel.2009.07.023>
- Jeong, S.G., Mo, Y., Kim, H.G., Park, C.H., Lee, D.K., 2016. Mapping riparian habitat using a combination of remote-sensing techniques. *Int. J. Remote Sens.* 37, 1069–1088. doi:10.1080/01431161.2016.1142685
- Kalacska, M., Lalonde, M., Moore, T.R., 2015. Estimation of foliar chlorophyll and nitrogen content in an ombrotrophic bog from hyperspectral data: Scaling from leaf to image. *Remote Sens. Environ.* 169, 270–279. doi:<http://dx.doi.org/10.1016/j.rse.2015.08.012>
- Karimi, Y., Prasher, S.O., Patel, R.M., Kim, S.H., 2006. Application of support vector machine technology for weed and nitrogen stress detection in corn. *Comput. Electron. Agric.* 51, 99–109.
- Keenan, T.F., Davidson, E.A., Munger, J.W., Richardson, A.D., 2013. Rate my data: quantifying the value of ecological data for the development of models of the terrestrial carbon cycle. *Ecol. Appl.* 23, 273–286. doi:10.1890/12-0747.1
- Kenett, R.S., Shmueli, G., 2015. Clarifying the terminology that describes scientific reproducibility. *Nat. Methods* 12, 699.
- Kim, Y., Knox, R.G., Longo, M., Medvigy, D., Hutyra, L.R., Pyle, E.H., Wofsy, S.C., Bras, R.L., Moorcroft, P.R., 2012. Seasonal carbon dynamics and water fluxes in an Amazon rainforest. *Glob. Chang. Biol.* 18, 1322–1334. doi:10.1111/j.1365-2486.2011.02629.x
- Knyazikhin, Y., Martonchik J., V., Myneni R., B., Diner D., J., Running S., W., 1998. Synergistic algorithm for estimating vegetation canopy leaf area index and fraction of absorbed photosynthetically active radiation from MODIS and MISR data. *J. Geophys. Res. Atmos.* 103, 32257–32275. doi:10.1029/98JD02462
- Knyazikhin, Y., Lewis, P., Disney, M., Mottus, M., Rautiainen, M., Stenberg, P., Kaufmann, R., Marshak, A., Schull, M., Latorre-Carmona, P., Vanderbilt, V., Davis,

- A., Baret, F., Jacquemoud, S., Lyapustin, A., Yang, Y., Myneni, R., 2013. Reply to Ollinger et al.: Remote sensing of leaf nitrogen and emergent ecosystem properties. *Proc. Natl. Acad. Sci.* 110, E2438–E2438. doi:10.1073/pnas.1305930110
- Knyazikhin, Y., Lewis, P., Disney, M.I., Stenberg, P., Möttus, M., Rautiainen, M., Kaufmann, R.K., Marshak, A., Schull, M.A., Latorre Carmona, P., Vanderbilt, V., Davis, A.B., Baret, F., Jacquemoud, S., Lyapustin, A., Yang, Y., Myneni, R.B., 2013a. Reply to Townsend et al.: Decoupling contributions from canopy structure and leaf optics is critical for remote sensing leaf biochemistry. *Proc. Natl. Acad. Sci. U. S. A.* 110, E1075.
- Knyazikhin, Y., Schull, M.A., Stenberg, P., Möttus, M., Rautiainen, M., Yang, Y., Marshak, A., Latorre Carmona, P., Kaufmann, R.K., Lewis, P., Disney, M.I., Vanderbilt, V., Davis, A.B., Baret, F., Jacquemoud, S., Lyapustin, A., Myneni, R.B., 2013b. Hyperspectral remote sensing of foliar nitrogen content. *Proc. Natl. Acad. Sci.* 110, E185 LP-E192.
- Knyazikhin, Y., Schull, M.A., Stenberg, P., Möttus, M., Rautiainen, M., Yang, Y., Marshak, A., Latorre Carmona, P., Kaufmann, R.K., Lewis, P., Disney, M.I., Vanderbilt, V., Davis, A.B., Baret, F., Jacquemoud, S., Lyapustin, A., Myneni, R.B., Latorre C, P., Kaufmann, R.K., Lewis, P., Disney, M.I., Vanderbilt, V., Davis, A.B., Baret, F., Jacquemoud, S., Lyapustin, A., Myneni, R.B., 2013c. Hyperspectral remote sensing of foliar nitrogen content. *Proc. Natl. Acad. Sci. U. S. A.* 110, E185-92. doi:10.1073/pnas.1210196109
- Knyazikhin, Y., Schull, M.A., Xu, L., Myneni, R.B., Samanta, A., 2011. Canopy spectral invariants. Part 1: A new concept in remote sensing of vegetation. *J. Quant. Spectrosc. Radiat. Transf.* 112, 727–735.
doi:http://dx.doi.org/10.1016/j.jqsrt.2010.06.014
- Koetz, B., Morsdorf, F., van der Linden, S., Curt, T., Allgöwer, B., 2008. Multi-source land cover classification for forest fire management based on imaging spectrometry and LiDAR data. *For. Ecol. Manage.* 256, 263–271.
doi:https://doi.org/10.1016/j.foreco.2008.04.025

- Köhler, P., Guanter, L., Kobayashi, H., Walther, S., Yang, W., 2018. Assessing the potential of sun-induced fluorescence and the canopy scattering coefficient to track large-scale vegetation dynamics in Amazon forests. *Remote Sens. Environ.* 204, 769–785. doi:<https://doi.org/10.1016/j.rse.2017.09.025>
- Kottek, M., Grieser, J., Beck, C., Rudolf, B., Rubel, F., 2006. World Map of the Köppen-Geiger climate classification updated. *Meteorol. Zeitschrift* 15, 259–263. doi:[10.1127/0941-2948/2006/0130](https://doi.org/10.1127/0941-2948/2006/0130)
- Kuppel, S., Peylin, P., Chevallier, F., Bacour, C., Maignan, F., Richardson, A.D., 2012. Constraining a global ecosystem model with multi-site eddy-covariance data. *Biogeosciences* 9, 3757–3776. doi:[10.5194/bg-9-3757-2012](https://doi.org/10.5194/bg-9-3757-2012)
- Kvalheim, O.M., Arneberg, R., Bleie, O., Rajalahti, T., Smilde, A.K., Westerhuis, J.A., 2014. Variable importance in latent variable regression models. *J. Chemom.* 28, 615–622. doi:[10.1002/cem.2626](https://doi.org/10.1002/cem.2626)
- La Pierre, K.J., Smith, M.D., 2015. Functional trait expression of grassland species shift with short- and long-term nutrient additions. *Plant Ecol.* 216, 307–318. doi:[10.1007/s11258-014-0438-4](https://doi.org/10.1007/s11258-014-0438-4)
- Laslier, M., Hubert-Moy, L., Dufour, S., 2019. Mapping Riparian Vegetation Functions Using 3D Bispectral LiDAR Data. *Water* . doi:[10.3390/w11030483](https://doi.org/10.3390/w11030483)
- Latorre-Carmona, P., Knyazikhin, Y., Alonso, L., Moreno, J.F., Pla, F., 2014. On Hyperspectral Remote Sensing of Leaf Biophysical Constituents: Decoupling Vegetation Structure and Leaf Optics Using CHRIS–PROBA Data Over Crops in Barrax. *IEEE Geosci. Remote Sens. Lett.* 11, 1579–1583. doi:[10.1109/LGRS.2014.2305168](https://doi.org/10.1109/LGRS.2014.2305168)
- Lepine, L.C., Ollinger, S. V, Ouimette, A.P., Martin, M.E., 2016. Examining spectral reflectance features related to foliar nitrogen in forests: Implications for broad-scale nitrogen mapping. *Remote Sens. Environ.* 173, 174–186. doi:[10.1016/j.rse.2015.11.028](https://doi.org/10.1016/j.rse.2015.11.028)
- Leuning, R., 1995. A critical appraisal of a combined stomatal-photosynthesis model for C3 plants. *Plant. Cell Environ.* 18, 339–355. doi:[10.1111/j.1365-](https://doi.org/10.1111/j.1365-)

3040.1995.tb00370.x

- Levine, N.M., Zhang, K., Longo, M., Baccini, A., Phillips, O.L., Lewis, S.L., Alvarez-Dávila, E., Segalin de Andrade, A.C., Brienen, R.J.W., Erwin, T.L., Feldpausch, T.R., Monteagudo Mendoza, A.L., Nuñez Vargas, P., Prieto, A., Silva-Espejo, J.E., Malhi, Y., Moorcroft, P.R., 2016. Ecosystem heterogeneity determines the ecological resilience of the Amazon to climate change. *Proc. Natl. Acad. Sci.* 113, 793–797. doi:10.1073/pnas.1511344112
- Lewis, D., 2000. Causation as Influence. *J. Philos.* 97, 182–197. doi:10.2307/2678389
- Li, A., Dhakal, S., Glenn, F.N., Spaete, P.L., Shinneman, J.D., Pilliod, S.D., Arkle, S.R., McIlroy, K.S., 2017. Lidar Aboveground Vegetation Biomass Estimates in Shrublands: Prediction, Uncertainties and Application to Coarser Scales. *Remote Sens.* . doi:10.3390/rs9090903
- Li, X., Jia, X., Wang, L., Zhao, K., 2015. On Spectral Unmixing Resolution Using Extended Support Vector Machines. *IEEE Trans. Geosci. Remote Sens.* 53, 4985–4996. doi:10.1109/TGRS.2015.2415587
- Li, X., Liu, X., Liu, M., Wu, L., 2014. Random forest algorithm and regional applications of spectral inversion model for estimating canopy nitrogen concentration in rice. *J. Remote Sens.* 18, 934–945.
- Li, X., Zhang, Y., Bao, Y., Luo, J., Jin, X., Xu, X., Song, X., Yang, G., 2014. Exploring the Best Hyperspectral Features for LAI Estimation Using Partial Least Squares Regression. *Remote Sens.* 6, 6221–6241. doi:10.3390/rs6076221
- Li, Y., Nigh, T., 2011. GIS-based prioritization of private land parcels for biodiversity conservation: A case study from the Current and Eleven Point Conservation Opportunity Areas, Missouri. *Appl. Geogr.* 31, 98–107. doi:https://doi.org/10.1016/j.apgeog.2010.02.006
- Liang, S., 2003. Estimation of Land Surface Biophysical Variables, in: *Quantitative Remote Sensing of Land Surfaces*. John Wiley & Sons, Inc., pp. 246–309. doi:10.1002/047172372X.ch8
- Liao, W., Bellens, R., Pižurica, A., Gautama, S., Philips, W., 2014. Combining feature

- fusion and decision fusion for classification of hyperspectral and LiDAR data, in: 2014 IEEE Geoscience and Remote Sensing Symposium. pp. 1241–1244.
doi:10.1109/IGARSS.2014.6946657
- Liao, W., Pižurica, A., Bellens, R., Gautama, S., Philips, W., 2015. Generalized Graph-Based Fusion of Hyperspectral and LiDAR Data Using Morphological Features. *IEEE Geosci. Remote Sens. Lett.* 12, 552–556. doi:10.1109/LGRS.2014.2350263
- Lo, A., Chernoff, H., Zheng, T., Lo, S.-H., 2016. Framework for making better predictions by directly estimating variables' predictivity. *Proc. Natl. Acad. Sci.* .
- Lo, A., Chernoff, H., Zheng, T., Lo, S.-H., 2015. Why significant variables aren't automatically good predictors. *Proc. Natl. Acad. Sci.* 112, 13892–13897.
- Lokupitiya, E., Denning, A.S., Schaefer, K., Ricciuto, D., Anderson, R., Arain, M.A., Baker, I., Barr, A.G., Chen, G., Chen, J.M., Ciais, P., Cook, D.R., Dietze, M., El Maayar, M., Fischer, M., Grant, R., Hollinger, D., Izaurrealde, C., Jain, A., Kucharik, C., Li, Z., Liu, S., Li, L., Matamala, R., Peylin, P., Price, D., Running, S.W., Sahoo, A., Sprintsin, M., Suyker, A.E., Tian, H., Tonitto, C., Torn, M., Verbeeck, H., Verma, S.B., Xue, Y., 2016. Carbon and energy fluxes in cropland ecosystems: a model-data comparison. *Biogeochemistry* 129, 53–76. doi:10.1007/s10533-016-0219-3
- Longo, M., Knox, R.G., Levine, N.M., Swann, A.L.S., Medvigy, D.M., Dietze, M.C., Kim, Y., Zhang, K., Bonal, D., Burban, B., Camargo, P.B., Hayek, M.N., Saleska, S.R., da Silva, R., Bras, R.L., Wofsy, S.C., Moorcroft, P.R., 2019a. The biophysics, ecology, and biogeochemistry of functionally diverse, vertically- and horizontally-heterogeneous ecosystems: the Ecosystem Demography Model, version 2.2 - Part 2: Model evaluation. *Geosci. Model Dev. Discuss.* 2019, 1–34. doi:10.5194/gmd-2019-71
- Longo, M., Knox, R.G., Medvigy, D.M., Levine, N.M., Dietze, M.C., Kim, Y., Swann, A.L.S., Zhang, K., Rollinson, C.R., Bras, R.L., Wofsy, S.C., Moorcroft, P.R., 2019b. The biophysics, ecology, and biogeochemistry of functionally diverse, vertically- and horizontally-heterogeneous ecosystems: the Ecosystem Demography Model,

- version 2.2 — Part 1: Model description. *Geosci. Model Dev. Discuss.* 2019, 1–53.
doi:10.5194/gmd-2019-45
- M, L.D., W, O.K., G, F.M., E, T.P., C, S.S., J, L.P., Xubin, Z., Zong-Liang, Y., Samuel, L., Koichi, S., B, B.G., G, S.A., 2011. Parameterization improvements and functional and structural advances in Version 4 of the Community Land Model. *J. Adv. Model. Earth Syst.* 3. doi:10.1029/2011MS00045
- Martin, M.E., Plourde, L.C., Ollinger, S.V., Smith, M.-L., McNeil, B.E., 2008. A generalizable method for remote sensing of canopy nitrogen across a wide range of forest ecosystems. *Remote Sens. Environ.* 112, 3511–3519.
doi:10.1016/j.rse.2008.04.008
- Medvigy, D., Clark, K.L., Skowronski, N.S., Schäfer, K.V.R., 2012. Simulated impacts of insect defoliation on forest carbon dynamics. *Environ. Res. Lett.* 7, 45703.
doi:10.1088/1748-9326/7/4/045703
- Medvigy, D., Wofsy, S.C., Munger, J.W., Hollinger, D.Y., Moorcroft, P.R., 2009. Mechanistic scaling of ecosystem function and dynamics in space and time: Ecosystem Demography model version 2. *J. Geophys. Res.* 114, G01002.
doi:10.1029/2008JG000812
- Metcalf, D.B., 2014. A sink down under. *Nature* 509, 566.
- Mielcarek, M., Stereńczak, K., Khosravipour, A., 2018. Testing and evaluating different LiDAR-derived canopy height model generation methods for tree height estimation. *Int. J. Appl. Earth Obs. Geoinf.* 71, 132–143.
doi:https://doi.org/10.1016/j.jag.2018.05.002
- Migliavacca, M., Sonnentag, O., Keenan, T.F., Cescatti, A., O’Keefe, J., Richardson, A.D., 2012. On the uncertainty of phenological responses to climate change, and implications for a terrestrial biosphere model. *Biogeosciences* 9, 2063–2083.
doi:10.5194/bg-9-2063-2012
- Millennium Ecosystem Assessment, 2005. *Ecosystems and Human Well-Being: Desertification Synthesis.*
- Miller, R.F., Chambers, J.C., Pyke, D.A., Pierson, F.B., Williams, C.J., 2013. A review of

fire effects on vegetation and soils in the Great Basin Region: response and ecological site characteristics.

- Miphokasap, P., Honda, K., Vaiphasa, C., Souris, M., Nagai, M., 2012. Estimating Canopy Nitrogen Concentration in Sugarcane Using Field Imaging Spectroscopy. *Remote Sens.* . doi:10.3390/rs4061651
- Mitchell, J.J., Glenn, N., Anderson, M., Hruska, R.C., 2016. Flight Considerations and Hyperspectral Image Classifications for Dryland Vegetation Management from a Fixed-wing UAS. *Environ. Manag. Sustain. Dev.* 5, 41–57.
- Mitchell, J.J., Glenn, N.F., Sankey, T.T., Derryberry, D.R., Germino, M.J., 2012. Remote sensing of sagebrush canopy nitrogen. *Remote Sens. Environ.* 124, 217–223. doi:10.1016/j.rse.2012.05.002
- Mitchell, J.J., Shrestha, R., Spaete, L.P., Glenn, N.F., 2015. Combining airborne hyperspectral and LiDAR data across local sites for upscaling shrubland structural information: Lessons for HypSIRI. *Remote Sens. Environ.* 167, 98–110. doi:https://doi.org/10.1016/j.rse.2015.04.015
- Montgomery, D.R., Dietrich, W.E., 1992. Channel Initiation and the Problem of Landscape Scale. *Science* (80-.). 255, 826 LP-830. doi:10.1126/science.255.5046.826
- Moorcroft, P.R., Hurtt, G.C., Pacala, S.W., 2001. A METHOD FOR SCALING VEGETATION DYNAMICS: THE ECOSYSTEM DEMOGRAPHY MODEL (ED). *Ecol. Monogr.* 71, 557–586. doi:10.1890/0012-9615(2001)071[0557:AMFSVD]2.0.CO;2
- Morris, M.D., 1991. Factorial Sampling Plans for Preliminary Computational Experiments. *Technometrics* 33, 161–174. doi:10.1080/00401706.1991.10484804
- Myneni, R.B., Keeling, C.D., Tucker, C.J., Asrar, G., Nemani, R.R., 1997. Increased plant growth in the northern high latitudes from 1981 to 1991. *Nature* 386, 698–702. doi:10.1038/386698a0
- Narine, L.L., Popescu, C.S., Malambo, L., 2019. Synergy of ICESat-2 and Landsat for Mapping Forest Aboveground Biomass with Deep Learning. *Remote Sens.* .

doi:10.3390/rs11121503

- Neuenschwander, A.L., Magruder, L.A., Tyler, M., 2009. Landcover classification of small-footprint, full-waveform lidar data. *J. Appl. Remote Sens.* 3, 1–13.
- Novick, K.A., Ficklin, D.L., Stoy, P.C., Williams, C.A., Bohrer, G., Oishi, A.C., Papuga, S.A., Blanken, P.D., Noormets, A., Sulman, B.N., Scott, R.L., Wang, L., Phillips, R.P., 2016. The increasing importance of atmospheric demand for ecosystem water and carbon fluxes. *Nat. Clim. Chang.* 6, 1023.
- Okin, G.S., Roberts, D.A., Murray, B., Okin, W.J., 2001. Practical limits on hyperspectral vegetation discrimination in arid and semiarid environments. *Remote Sens. Environ.* 77, 212–225. doi:10.1016/S0034-4257(01)00207-3
- Ollinger, S., Frohking, S., Richardson, A., Martin, M., Hollinger, D., Reich, P., Plourde, L., 2009. Reply to Fisher: Nitrogen–albedo relationship in forests remains robust and thought-provoking. *Proc. Natl. Acad. Sci.* 106, E17 LP-E17.
- Ollinger, S. V., 2011. Sources of variability in canopy reflectance and the convergent properties of plants. *New Phytol.* 189, 375–394. doi:10.1111/j.1469-8137.2010.03536.x
- Ollinger, S. V., Reich, P.B., Frohking, S., Lepine, L.C., Hollinger, D.Y., Richardson, A.D., 2013. Nitrogen cycling, forest canopy reflectance, and emergent properties of ecosystems. *Proc. Natl. Acad. Sci.* 110, E2437–E2437. doi:10.1073/pnas.1304176110
- Ollinger, S. V., Richardson, A.D., Martin, M.E., Hollinger, D.Y., Frohking, S.E., Reich, P.B., Plourde, L.C., Katul, G.G., Munger, J.W., Oren, R., Smith, M.-L., Paw U, K.T., Bolstad, P. V., Cook, B.D., Day, M.C., Martin, T.A., Monson, R.K., Schmid, H.P., 2008. Canopy nitrogen, carbon assimilation, and albedo in temperate and boreal forests: Functional relations and potential climate feedbacks. *Proc. Natl. Acad. Sci.* 105, 19336–19341. doi:10.1073/pnas.0810021105
- Olsoy, P.J., Mitchell, J.J., Levia, D.F., Clark, P.E., Glenn, N.F., 2016. Estimation of big sagebrush leaf area index with terrestrial laser scanning. *Ecol. Indic.* 61, 815–821. doi:https://doi.org/10.1016/j.ecolind.2015.10.034

- Pacheco-Labrador, J., González-Cascón, R., Martín, M.P., Riaño, D., 2014. Understanding the optical responses of leaf nitrogen in Mediterranean Holm oak (*Quercus ilex*) using field spectroscopy. *Int. J. Appl. Earth Obs. Geoinf.* 26, 105–118. doi:<http://dx.doi.org/10.1016/j.jag.2013.05.013>
- Pandit, K., Dashti, H., Glenn, N.F., Flores, A.N., Maguire, K.C., Shinneman, D.J., Flerchinger, G.N., Fellows, A.W., 2019. Optimizing shrub (Sagebrush) parameters to estimate gross primary production of sagebrush-steppe ecosystem using Ecosystem Demography (ED2) model. *Geosci. Model Dev.* Accepted f.
- Pappas, C., Faticchi, S., Leuzinger, S., Wolf, A., Burlando, P., 2013. Sensitivity analysis of a process-based ecosystem model: Pinpointing parameterization and structural issues. *J. Geophys. Res. Biogeosciences* 118, 505–528. doi:10.1002/jgrg.20035
- Patel, N., Kaushal, B., 2010. Improvement of user's accuracy through classification of principal component images and stacked temporal images. *Geo-spatial Inf. Sci.* 13, 243–248. doi:10.1007/s11806-010-0380-0
- Patten, D.T., 1998. Riparian ecosystems of semi-arid North America: Diversity and human impacts. *Wetlands* 18, 498–512. doi:10.1007/BF03161668
- Pellissier, P.A., Ollinger, S. V, Lepine, L.C., Palace, M.W., McDowell, W.H., 2015. Remote sensing of foliar nitrogen in cultivated grasslands of human dominated landscapes. *Remote Sens. Environ.* 167, 88–97. doi:10.1016/j.rse.2015.06.009
- Polley, H.W., Briske, D.D., Morgan, J.A., Wolter, K., Bailey, D.W., Brown, J.R., 2013. Climate Change and North American Rangelands: Trends, Projections, and Implications. *Rangel. Ecol. Manag.* 66, 493–511. doi:<https://doi.org/10.2111/REM-D-12-00068.1>
- Post, H., Vrugt, J.A., Fox, A., Vereecken, H., Hendricks Franssen, H.-J., 2017. Estimation of Community Land Model parameters for an improved assessment of net carbon fluxes at European sites. *J. Geophys. Res. Biogeosciences* 122, 661–689. doi:10.1002/2015JG003297
- Poulter, B., Frank, D., Ciais, P., Myneni, R.B., Andela, N., Bi, J., Broquet, G., Canadell, J.G., Chevallier, F., Liu, Y.Y., Running, S.W., Sitch, S., Van Der Werf, G.R., 2014.

Contribution of semi-arid ecosystems to interannual variability of the global carbon cycle. *Nature* 509. doi:10.1038/nature13376

Pyke, D.A., Chambers, J.C., Pellant, M., Knick, S.T., Miller, R.F., Beck, J.L., Doescher, P.S., Schupp, E.W., Roundy, B.A., Brunson, M., McIver, J.D., 2015. Restoration handbook for sagebrush steppe ecosystems with emphasis on greater sage-grouse habitat—Part 1. Concepts for understanding and applying restoration, Circular. Reston, VA. doi:10.3133/cir1416

Ramoelo, A., Skidmore, A.K., Cho, M.A., Schlerf, M., Mathieu, R., Heitkönig, I.M.A., 2012. Regional estimation of savanna grass nitrogen using the red-edge band of the spaceborne RapidEye sensor. *Int. J. Appl. Earth Obs. Geoinf.* 19, 151–162. doi:http://dx.doi.org/10.1016/j.jag.2012.05.009

Ray, T.W., Murray, B.C., 1996. Nonlinear spectral mixing in desert vegetation. *Remote Sens. Environ.* 55, 59–64. doi:https://doi.org/10.1016/0034-4257(95)00171-9

Renwick, K.M., Fellows, A., Flerchinger, G.N., Lohse, K.A., Clark, P.E., Smith, W.K., Emmett, K., Poulter, B., 2019. Modeling phenological controls on carbon dynamics in dryland sagebrush ecosystems. *Agric. For. Meteorol.* 274, 85–94. doi:https://doi.org/10.1016/j.agrformet.2019.04.003

Richardson, A.D., Keenan, T.F., Migliavacca, M., Ryu, Y., Sonnentag, O., Toomey, M., 2013. Climate change, phenology, and phenological control of vegetation feedbacks to the climate system. *Agric. For. Meteorol.* 169, 156–173. doi:http://dx.doi.org/10.1016/j.agrformet.2012.09.012

Roberts, D.A., Gardner, M., Church, R., Ustin, S., Scheer, G., Green, R.O., 1998. Mapping Chaparral in the Santa Monica Mountains Using Multiple Endmember Spectral Mixture Models. *Remote Sens. Environ.* 65, 267–279. doi:https://doi.org/10.1016/S0034-4257(98)00037-6

Roberts, D.A., Halligan, K., Dennison, P., 2007. VIPER Tools User Manual. Terrain.

Roberts, D.A., Ustin, S.L., Ogunjemiyo, S., Greenberg, J., Dobrowski, S.Z., Chen, J., Hinckley, T.M., 2004. Spectral and Structural Measures of Northwest Forest Vegetation at Leaf to Landscape Scales. *Ecosystems* 7, 545–562.

doi:10.1007/s10021-004-0144-5

Roth, K.L., Roberts, D.A., Dennison, P.E., Alonzo, M., Peterson, S.H., Beland, M., 2015. Differentiating plant species within and across diverse ecosystems with imaging spectroscopy. *Remote Sens. Environ.* 167, 135–151.

doi:<https://doi.org/10.1016/j.rse.2015.05.007>

Roundy, B.A., Aanderud, Z., Young, K., Hulet, A., Bunting, S., 2014. Final Report: Piñon and juniper tree mastication effects in the Great Basin and Colorado Plateau.

Roussel, J.-R., Caspersen, J., Béland, M., Thomas, S., Achim, A., 2017. Removing bias from LiDAR-based estimates of canopy height: Accounting for the effects of pulse density and footprint size. *Remote Sens. Environ.* 198, 1–16.

doi:<https://doi.org/10.1016/j.rse.2017.05.032>

Running, S., Nemani, R., Heinsch, F.A.N.N., Zhao, M., REEVES, M., Hashimoto, H., 2004. A Continuous Satellite-Derived Measure of Global Terrestrial Primary Production. *Bioscience* 54, 547–560. doi:10.1641/0006-3568(2004)054[0547:ACSMOG]2.0.CO;2

Ryu, Y., Berry, J.A., Baldocchi, D.D., 2019. What is global photosynthesis? History, uncertainties and opportunities. *Remote Sens. Environ.* 223, 95–114.

doi:<https://doi.org/10.1016/j.rse.2019.01.016>

Salo, J.A., Theobald, D.M., Brown, T.C., 2016. Evaluation of Methods for Delineating Riparian Zones in a Semi-Arid Montane Watershed. *JAWRA J. Am. Water Resour. Assoc.* 52, 632–647. doi:10.1111/1752-1688.12414

Saltelli, A., Tarantola, S., Campolongo, F., 2000. Sensitivity Analysis as an Ingredient of Modeling. *Stat. Sci.* 15, 377–395.

Santaren, D., Peylin, P., Viovy, N., Ciais, P., 2007. Optimizing a process-based ecosystem model with eddy-covariance flux measurements: A pine forest in southern France. *Global Biogeochem. Cycles* 21. doi:10.1029/2006GB002834

Savitzky, A., Golay, M.J.E., 1964. Smoothing and Differentiation of Data by Simplified Least Squares Procedures. *Anal. Chem.* 36, 1627–1639. doi:10.1021/ac60214a047

- Scanlon, B.R., Keese, K.E., Flint, A.L., Flint, L.E., Gaye, C.B., Edmunds, W.M., Simmers, I., 2006. Global synthesis of groundwater recharge in semiarid and arid regions. *Hydrol. Process.* 20, 3335–3370. doi:10.1002/hyp.6335
- Schimel, D., Schneider, F.D., Participants, J.P.L.C. and E., 2019. Flux towers in the sky: global ecology from space. *New Phytol.* 0. doi:10.1111/nph.15934
- Scott, R.L., Biederman, J.A., Hamerlynck, E.P., Barron-Gafford, G.A., 2015. The carbon balance pivot point of southwestern U.S. semiarid ecosystems: Insights from the 21st century drought. *J. Geophys. Res. Biogeosciences* 120, 2612–2624. doi:10.1002/2015JG003181
- Sellers, P.J., 1987. Canopy reflectance, photosynthesis, and transpiration, II. The role of biophysics in the linearity of their interdependence. *Remote Sens. Environ.* 21, 143–183. doi:http://dx.doi.org/10.1016/0034-4257(87)90051-4
- Seyfried, M., Harris, R., Marks, D., Jacob, B., 2001. Geographic Database, Reynolds Creek Experimental Watershed, Idaho, United States. *Water Resour. Res.* 37, 2825–2829. doi:10.1029/2001WR000414
- Shanmugam, S., SrinivasaPerumal, P., 2014. Spectral matching approaches in hyperspectral image processing. *Int. J. Remote Sens.* 35, 8217–8251. doi:10.1080/01431161.2014.980922
- Silvan-Cardenas, J.L., Corona-Romero, N., 2017. Radiation budget of vegetation canopies with reflective surface: A generalization using the Markovian approach. *Remote Sens. Environ.* 189, 118–131. doi:https://doi.org/10.1016/j.rse.2016.11.019
- Silvan-Cardenas, J.L., Wang, L., 2010. Retrieval of subpixel Tamarix canopy cover from Landsat data along the Forgotten River using linear and nonlinear spectral mixture models. *Remote Sens. Environ.* 114, 1777–1790. doi:http://dx.doi.org/10.1016/j.rse.2010.04.003
- Silvan-Cardenas, J.L., Wang, L., 2008. Sub-pixel confusion–uncertainty matrix for assessing soft classifications. *Remote Sens. Environ.* 112, 1081–1095. doi:https://doi.org/10.1016/j.rse.2007.07.017
- Singh, A., Serbin, S.P., McNeil, B.E., Kingdon, C.C., Townsend, P.A., 2015. Imaging

- spectroscopy algorithms for mapping canopy foliar chemical and morphological traits and their uncertainties. *Ecol. Appl.* 25, 2180–2197. doi:10.1890/14-2098.1.sm
- Smith, B., Prentice, I.C., Sykes, M.T., 2001. Representation of vegetation dynamics in the modelling of terrestrial ecosystems: comparing two contrasting approaches within European climate space. *Glob. Ecol. Biogeogr.* 10, 621–637. doi:10.1046/j.1466-822X.2001.t01-1-00256.x
- Smith, W.K., Biederman, J.A., Scott, R.L., Moore, D.J.P., He, M., Kimball, J.S., Yan, D., Hudson, A., Barnes, M.L., MacBean, N., Fox, A.M., Litvak, M.E., 2018. Chlorophyll Fluorescence Better Captures Seasonal and Interannual Gross Primary Productivity Dynamics Across Dryland Ecosystems of Southwestern North America. *Geophys. Res. Lett.* 45, 748–757. doi:10.1002/2017GL075922
- Smith, W.K., Dannenberg, M.P., Yan, D., Herrmann, S., Barnes, M.L., Barron-Gafford, G.A., Biederman, J.A., Ferrenberg, S., Fox, A.M., Hudson, A., Knowles, J.F., MacBean, N., Moore, D.J.P., Nagler, P.L., Reed, S.C., Rutherford, W.A., Scott, R.L., Wang, X., Yang, J., 2019. Remote sensing of dryland ecosystem structure and function: Progress, challenges, and opportunities. *Remote Sens. Environ.* 233, 111401. doi:https://doi.org/10.1016/j.rse.2019.111401
- Smola, A.J., Schölkopf, B., 2004. A tutorial on support vector regression. *Stat. Comput.* 14, 199–222. doi:10.1023/B:STCO.0000035301.49549.88
- Smolander, S., Stenberg, P., 2005. Simple parameterizations of the radiation budget of uniform broadleaved and coniferous canopies. *Remote Sens. Environ.* 94, 355–363. doi:http://dx.doi.org/10.1016/j.rse.2004.10.010
- Solomons, A.G., Mikhailova, E.A., Post, C.J., Sharp, J.L., 2015. LiDAR-based predictions of flow channels through riparian buffer zones. *Water Sci.* 29, 123–133. doi:https://doi.org/10.1016/j.wsj.2015.11.001
- Spaete, L.P., Glenn, N.F., Derryberry, D.R., Sankey, T.T., Mitchell, J.J., Hardegree, S.P., 2011. Vegetation and slope effects on accuracy of a LiDAR-derived DEM in the sagebrush steppe. *Remote Sens. Lett.* 2, 317–326. doi:10.1080/01431161.2010.515267

- Stavros, E.N., Schimel, D., Pavlick, R., Serbin, S., Swann, A., Duncanson, L., Fisher, J.B., Fassnacht, F., Ustin, S., Dubayah, R., Schweiger, A., Wennberg, P., 2017. ISS observations offer insights into plant function. *Nat. Ecol. & Evol.* 1, 194.
- Stocker, B.D., Zscheischler, J., Keenan, T.F., Prentice, I.C., Seneviratne, S.I., Peñuelas, J., 2019. Drought impacts on terrestrial primary production underestimated by satellite monitoring. *Nat. Geosci.* 12, 264–270. doi:10.1038/s41561-019-0318-6
- Storn, R., Price, K., 1997. Differential Evolution – A Simple and Efficient Heuristic for global Optimization over Continuous Spaces. *J. Glob. Optim.* 11, 341–359. doi:10.1023/A:1008202821328
- Streutker, D.R., Glenn, N.F., 2006. LiDAR measurement of sagebrush steppe vegetation heights. *Remote Sens. Environ.* 102, 135–145. doi:https://doi.org/10.1016/j.rse.2006.02.011
- Stuckens, J., Somers, B., Delalieux, S., Verstraeten, W.W., Coppin, P., 2009. The impact of common assumptions on canopy radiative transfer simulations: A case study in Citrus orchards. *J. Quant. Spectrosc. Radiat. Transf.* 110, 1–21. doi:http://dx.doi.org/10.1016/j.jqsrt.2008.09.001
- Sun, J., Shi, S., Gong, W., Yang, J., Du, L., Song, S., Chen, B., Zhang, Z., 2017. Evaluation of hyperspectral LiDAR for monitoring rice leaf nitrogen by comparison with multispectral LiDAR and passive spectrometer. *Sci. Rep.* 7, 40362.
- Svejcar, T., Boyd, C., Davies, K., Hamerlynck, E., Svejcar, L., 2017. Challenges and limitations to native species restoration in the Great Basin, USA. *Plant Ecol.* 218, 81–94. doi:10.1007/s11258-016-0648-z
- Tian, Y., Hassmiller Lich, K., Osgood, N.D., Eom, K., Matchar, D.B., 2016. Linked Sensitivity Analysis, Calibration, and Uncertainty Analysis Using a System Dynamics Model for Stroke Comparative Effectiveness Research. *Med. Decis. Mak.* 36, 1043–1057. doi:10.1177/0272989X16643940
- Tompalski, P., Coops, N.C., White, J.C., Wulder, M.A., Yuill, A., 2017. Characterizing streams and riparian areas with airborne laser scanning data. *Remote Sens. Environ.* 192, 73–86. doi:https://doi.org/10.1016/j.rse.2017.01.038

- Townsend, P.A., Serbin, S.P., Kruger, E.L., Gamon, J.A., 2013. Disentangling the contribution of biological and physical properties of leaves and canopies in imaging spectroscopy data. *Proc. Natl. Acad. Sci. U. S. A.* 110, E1074.
doi:10.1073/pnas.1300952110
- Trugman, A.T., Fenton, N.J., Bergeron, Y., Xu, X., Welp, L.R., Medvigy, D., 2016. Climate, soil organic layer, and nitrogen jointly drive forest development after fire in the North American boreal zone. *J. Adv. Model. Earth Syst.* 8, 1180–1209.
doi:10.1002/2015MS000576
- Tucker, C.J., Slayback, D.A., Pinzon, J.E., Los, S.O., Myneni, R.B., Taylor, M.G., 2001. Higher northern latitude normalized difference vegetation index and growing season trends from 1982 to 1999. *Int. J. Biometeorol.* 45, 184–190. doi:10.1007/s00484-001-0109-8
- Ustin, S.L., 2013. Remote sensing of canopy chemistry. *Proc. Natl. Acad. Sci. U. S. A.* 110, 804–5. doi:10.1073/pnas.1219393110
- Ustin, S.L., Gitelson, A.A., Jacquemoud, S., Schaepman, M., Asner, G.P., Gamon, J.A., Zarco-Tejada, P., 2009. Retrieval of foliar information about plant pigment systems from high resolution spectroscopy. *Remote Sens. Environ.* 113, Suppl, S67–S77.
doi:https://doi.org/10.1016/j.rse.2008.10.019
- Ustin, S.L., Roberts, D.A., Gamon, J.A., Asner, G.P., Green, R.O., 2004. Using Imaging Spectroscopy to Study Ecosystem Processes and Properties. *Bioscience* 54, 523–534. doi:10.1641/0006-3568(2004)054[0523:U1STSE]2.0.CO;2
- Vanhatalo, K.M., Rautiainen, M., Stenberg, P., 2014. Monitoring the broadleaf fraction and canopy cover of boreal forests using spectral invariants. *J. Quant. Spectrosc. Radiat. Transf.* 133, 482–488. doi:http://dx.doi.org/10.1016/j.jqsrt.2013.09.011
- Vaughn, N.R., Moskal, L.M., Turnblom, E.C., 2012. Tree Species Detection Accuracies Using Discrete Point Lidar and Airborne Waveform Lidar. *Remote Sens.* .
doi:10.3390/rs4020377
- Verma, M., Friedl, M.A., Richardson, A.D., Kiely, G., Cescatti, A., Law, B.E., Wohlfahrt, G., Gielen, B., Roupsard, O., Moors, E.J., Toscano, P., Vaccari, F.P.,

- Gianelle, D., Bohrer, G., Varlagin, A., Buchmann, N., van Gorsel, E., Montagnani, L., Propastin, P., 2014. Remote sensing of annual terrestrial gross primary productivity from MODIS: an assessment using the FLUXNET La Thuile data set. *Biogeosciences* 11, 2185–2200. doi:10.5194/bg-11-2185-2014
- Verstraete, M.M., Pinty, B., Myneni, R.B., 1996. Potential and limitations of information extraction on the terrestrial biosphere from satellite remote sensing. *Remote Sens. Environ.* 58, 201–214. doi:[https://doi.org/10.1016/S0034-4257\(96\)00069-7](https://doi.org/10.1016/S0034-4257(96)00069-7)
- Villarreal, M.L., Van Leeuwen, W.J.D., Romo-Leon, J.R., 2012. Mapping and monitoring riparian vegetation distribution, structure and composition with regression tree models and post-classification change metrics. *Int. J. Remote Sens.* 33, 4266–4290. doi:10.1080/01431161.2011.644594
- Walter-Shea, E.A., J. M. Norman, 1991. Leaf optical properties, in: Myneni, R.B., Ross, J. (Eds.), *Photon-Vegetation Interactions : Applications in Optical Remote Sensing and Plant Ecology*. pp. 229–250.
- Wang, W., Nemani, R., Hashimoto, H., Ganguly, S., Huang, D., Knyazikhin, Y., Myneni, R., Bala, G., 2018. An Interplay between Photons, Canopy Structure, and Recollision Probability: A Review of the Spectral Invariants Theory of 3D Canopy Radiative Transfer Processes. *Remote Sens.* . doi:10.3390/rs10111805
- Wang, Y.-P., Leuning, R., Cleugh, H.A., Coppin, P.A., 2001. Parameter estimation in surface exchange models using nonlinear inversion: how many parameters can we estimate and which measurements are most useful? *Glob. Chang. Biol.* 7, 495–510. doi:10.1046/j.1365-2486.2001.00434.x
- Wang, Z., Wang, T., Darvishzadeh, R., Skidmore, K.A., Jones, S., Suarez, L., Woodgate, W., Heiden, U., Heurich, M., Hearne, J., 2016. Vegetation Indices for Mapping Canopy Foliar Nitrogen in a Mixed Temperate Forest. *Remote Sens.* . doi:10.3390/rs8060491
- Ward, M.D., Greenhill, B.D., Bakke, K.M., 2010. The perils of policy by p-value: Predicting civil conflicts. *J. Peace Res.* 47, 363–375. doi:10.1177/0022343309356491

- Wasser, L., Day, R., Chasmer, L., Taylor, A., 2013. Influence of Vegetation Structure on Lidar-derived Canopy Height and Fractional Cover in Forested Riparian Buffers During Leaf-Off and Leaf-On Conditions. *PLoS One* 8, e54776.
- White, J., Welter, D., Doherty, J., 2019. PEST++: version 4.2.1.
- Wilcox, K.R., Blair, J.M., Smith, M.D., Knapp, A.K., 2015. Does ecosystem sensitivity to precipitation at the site-level conform to regional-scale predictions? *Ecology* 0. doi:10.1890/15-1437
- Williams, R.J., Myers, B.A., Muller, W.J., Duff, G.A., Eamus, D., 1997. LEAF PHENOLOGY OF WOODY SPECIES IN A NORTH AUSTRALIAN TROPICAL SAVANNA. *Ecology* 78, 2542–2558. doi:10.1890/0012-9658(1997)078[2542:LPOWSI]2.0.CO;2
- Wold, S., Sjöström, M., Eriksson, L., 2001. PLS-regression: a basic tool of chemometrics. *Chemom. Intell. Lab. Syst.* 58, 109–130. doi:10.1016/S0169-7439(01)00155-1
- Xu, L., Myneni, R.B., Chapin III, F.S., Callaghan, T. V, Pinzon, J.E., Tucker, C.J., Zhu, Z., Bi, J., Ciais, P., Tommervik, H., Euskirchen, E.S., Forbes, B.C., Piao, S.L., Anderson, B.T., Ganguly, S., Nemani, R.R., Goetz, S.J., Beck, P.S.A., Bunn, A.G., Cao, C., Stroeve, J.C., 2013. Temperature and vegetation seasonality diminishment over northern lands. *Nat. Clim. Chang.* 3, 581–586.
- Xu, X., Li, W., Ran, Q., Du, Q., Gao, L., Zhang, B., 2018. Multisource Remote Sensing Data Classification Based on Convolutional Neural Network. *IEEE Trans. Geosci. Remote Sens.* 56, 937–949. doi:10.1109/TGRS.2017.2756851
- Xu, X., Medvigy, D., Powers, J.S., Becknell, J.M., Guan, K., 2016a. Diversity in plant hydraulic traits explains seasonal and inter-annual variations of vegetation dynamics in seasonally dry tropical forests. *New Phytol.* 212, 80–95. doi:10.1111/nph.14009
- Xu, X., Medvigy, D., Powers, J.S., Becknell, J.M., Guan, K., 2016b. Diversity in plant hydraulic traits explains seasonal and inter-annual variations of vegetation dynamics in seasonally dry tropical forests. *New Phytol.* 212, 80–95. doi:10.1111/nph.14009
- Yan, D., Scott, R.L., Moore, D.J.P., Biederman, J.A., Smith, W.K., 2019. Understanding

the relationship between vegetation greenness and productivity across dryland ecosystems through the integration of PhenoCam, satellite, and eddy covariance data. *Remote Sens. Environ.* 223, 50–62.

doi:<https://doi.org/10.1016/j.rse.2018.12.029>

Yáñez-Rausell, L., Malenovsky, Z., Rautiainen, M., Clevers, J.G.P.W., Lukeš, P., Hanuš, J., Schaepman, M.E., 2015. Estimation of Spruce Needle-Leaf Chlorophyll Content Based on DART and PARAS Canopy Reflectance Models. *IEEE J. Sel. Top. Appl. Earth Obs. Remote Sens.* 8, 1534–1544. doi:10.1109/JSTARS.2015.2400418

Yang, C., Everitt, J.H., Johnson, H.B., 2009. Applying image transformation and classification techniques to airborne hyperspectral imagery for mapping Ashe juniper infestations. *Int. J. Remote Sens.* 30, 2741–2758.

doi:10.1080/01431160802555812

Zhang, K., de Almeida Castanho, A.D., Galbraith, D.R., Moghim, S., Levine, N.M., Bras, R.L., Coe, M.T., Costa, M.H., Malhi, Y., Longo, M., Knox, R.G., McKnight, S., Wang, J., Moorcroft, P.R., 2015. The fate of Amazonian ecosystems over the coming century arising from changes in climate, atmospheric CO₂, and land use. *Glob. Chang. Biol.* doi:10.1111/gcb.12903

Zhang, Y., Zhang, H., Nasrabadi, N.M., Huang, T.S., 2013. Multi-metric learning for multi-sensor fusion based classification. *Inf. Fusion* 14, 431–440.

doi:<https://doi.org/10.1016/j.inffus.2012.05.002>

Zhao, K., Valle, D., Popescu, S., Zhang, X., Mallick, B., 2013. Hyperspectral remote sensing of plant biochemistry using Bayesian model averaging with variable and band selection. *Remote Sens. Environ.* 132, 102–119. doi:10.1016/j.rse.2012.12.026

Zhao, K., Wulder, M.A., Hu, T., Bright, R., Wu, Q., Qin, H., Li, Y., Toman, E., Mallick, B., Zhang, X., Brown, M., 2019. Detecting change-point, trend, and seasonality in satellite time series data to track abrupt changes and nonlinear dynamics: A Bayesian ensemble algorithm. *Remote Sens. Environ.* 232, 111181.

doi:<https://doi.org/10.1016/j.rse.2019.04.034>

Zhi, W., Yuan, L., Ji, G., Liu, Y., Cai, Z., Chen, X., 2015. A bibliometric review on

carbon cycling research during 1993–2013. *Environ. Earth Sci.* 74, 6065–6075.
doi:10.1007/s12665-015-4629-7

Zhou, H.H., Singh, V., Johnson, S.C., Wahba, G., 2018. Statistical tests and identifiability conditions for pooling and analyzing multisite datasets. *Proc. Natl. Acad. Sci.*

APPENDIX A

Supplementary information for chapter 2

SI Text 1. Data collection

Study area. The semi-arid Great Basin (GB) covers 500,000 km² and is considered one of the most imperiled ecosystems in North America by the Department of Interior (Integrated Rangeland Fire Management, 2016). Five sites were selected across the GB for the field study and data collection (Fig. S1). The Reynolds Creek Experimental Watershed (RCEW), Birds of Prey (BoP) and Hollister sites are located in Idaho and the Big Pine (BP) and Lone Pile (LP) sites are located in California on the eastern side of the Sierra Mountains. Elevation in the GB ranges from 400 m to more than 3000 m. The basins, which are located at the lowest elevations, are typically hot and dry while the higher elevations are cool to cold and moist. Annual precipitation across much of the region ranges from 150 to 400 mm. The GB region encompasses a large portion of native sagebrush (*Artemisia tridentata*) community (Miller et al., 2013). Other shrub species common to the area include bitterbrush (*Purshia tridentata*) and rabbitbrush (*Ericameria nauseosa*). The GB has experienced a number of disturbances caused by the invasion of annual grasses such as cheatgrass (*Bromus tectorum* L), and the encroachment of pinyon (*Pinus spp.*) and juniper (*Juniperus spp.*) trees, fire, and extensive grazing (Roundy et al., 2014).

We selected a semi-arid ecosystem as our study area for the following conceptual and technical reasons: (1) recent studies have highlighted the importance of semi-arid ecosystems in the global carbon cycle (Ahlström et al., 2015; Poulter et al., 2014), and further elucidation of vegetation parameters at fine scales in these ecosystems are necessary to investigate cross-scale interactions; (2) It has been suggested that studies conducted in ecosystems with sparse vegetation cover and low LAI might improve our interpretation of interactions between near infrared (NIR) spectroscopy and N (Lepine et al., 2016). LAI in

these ecosystems is not saturated as contrasted to forest ecosystems where reflectance may be insensitive to the variation of LAI and may cause misinterpretation of the interaction between LAI, N, and light, particularly in the NIR region (Yuri Knyazikhin et al., 2013c); and (3) semi-arid ecosystems provide the opportunity to study the impact of canopy background on the estimation of N. Previous related studies have focused on closed canopy systems, yet many ecosystems including savannas shrublands, and tundra, have open canopies with spectral mixing from the canopy background and structure.

Field sampling. Field data sampling was conducted during 2014 and 2015 (Table S1). A total of 147 (10 m × 10 m) plots were collected. Plots were selected based on stratified random sampling. Random locations were generated at each site, and plots that were accessible and representative of the micro-climate gradient (i.e. elevation gradient) were chosen. Moreover, considering the dominance of sagebrush and bitterbrush in the study sites, plots were selected based on the dominant cover of one of these two species. For the plots located in Idaho, the four corners were recorded using a Topcon HiperV RTK GPS (Topcon Positioning System, Inc) and sub-centimeter locations were processed using OPUS (Online Position User Service) and Topcon MAGNET Office software. A Trimble GeoExplorer 7 series GPS (Trimble, Inc) was used to acquire locational data for the plots located in California. At all sites shrub cover was determined along 5 transects running north to south every 2 m starting 1 m in from the corners using the line transect method. For each shrub in the plot, the canopy height and the minor and major widths were recorded. Within each transect, one shrub (in total six shrubs per plot) that was representative of the distribution of the shrub sizes inside the plot, was selected for N and canopy LAI measurements. The location of each individual was recorded using the GPS.

Single-sided leaf area was measured using a Li-COR Biosciences area meter (model LI-2200; Lincoln, Nebraska) and AccuPAR (model LP-80, Decagon Devices Inc., Pullman, WA, USA) for each shrub. Some plots or shrubs were later removed from the analysis due to the high level of noise or technical problems such as instrument failure. In total 119 and 147 plots were used for the analysis of the N and LAI, respectively. Green leaf samples were randomly clipped from different portions of each individual shrub, and these samples were oven-dried at 70° C for 48 hours and ground in a Wiley mill. Foliar N concentration (g N/100 g sample) was measured using a thermo Delta V Plus IRMS coupled to a Costech ECS 4010 elemental analyzer (Stable Isotope Laboratory, Boise State University). The canopy %N was calculated as the mean of the %N of the leaves collected from each individual shrub. The plot %N was calculated as the mean %N from each of the 6 shrubs in each plot. Similarly, the mean of the 6 LAI measurements was used as the plot-level LAI.

Spectral data. Concurrent to field data collection during 2014 and 2015, the airborne AVIRIS-Next Generation (AVIRIS-NG; operated by NASA Jet Propulsion Laboratory) hyperspectral sensor collected overlapping flightlines of hyperspectral imagery (Table S1). In total 44 and 51 flightlines in 2014 and 2015, respectively, were collected over the study areas. The 2014 and 2015 images have a nominal pixel size of 2.6 and 1.6 m, respectively. AVIRIS-NG samples 432 bands of radiance between 350 and 2500 nm at continuous intervals of 5nm. The AVIRIS-NG Level 2 products were converted from radiance to reflectance, orthorectified and corrected for the atmospheric effects using Atmospheric REMoval (ATREM) algorithm (Gao and Goetz, 1995). The 1300-1450 and 1750-2000 nm bands were removed due to the strong influence of atmospheric water

absorption. Bands less than 400 nm were excluded from the analysis due to noise. The resulting 325 bands were used in the study. The mean reflectance of the pixels included in the plots were considered as the plot-level reflectance. Canopy spectral signatures were collected in the field using a FieldSpec Pro Spectroradiometer (ASD Inc., Boulder, CO, USA) for each of the 6 shrubs inside the plot. The ASD spectral resolution is 1nm which includes 2151 spectral bands within 350-2500 nm range. For each representative shrub, five measurements (10 replicates per measurements) were made. The fiber optic, with a field of view (FOV) of 25°, was positioned approximately 25-40 cm above the canopy equating to an approximate FOV of ~11-18 cm diameter. Before each shrub spectral measurement, a standard white panel with known reflectivity was used to normalize the shrub canopy measurements. Measurements were limited to within 2 hours of solar noon under clear sky conditions. Spectral measurements were collected in the lab using a contact probe on the dry leaves laying on a black surface with low reflectivity (less than 5% over the entire spectrum). Noisy bands and bands less than 400 nm and more than 2400 nm were excluded from the leaf scale analysis. The spectral reflectance of the background reflectance was also acquired from a number of plots. The background reflectance ranges from bare soil with no vegetation to soils with dead shrub, litter or biocrusts (further referred to here as soil). Fig. S2 shows the mean reflectance of the dry leaf, canopy, plot, and soil datasets.



Figure S1. Study area, the Great Basin.

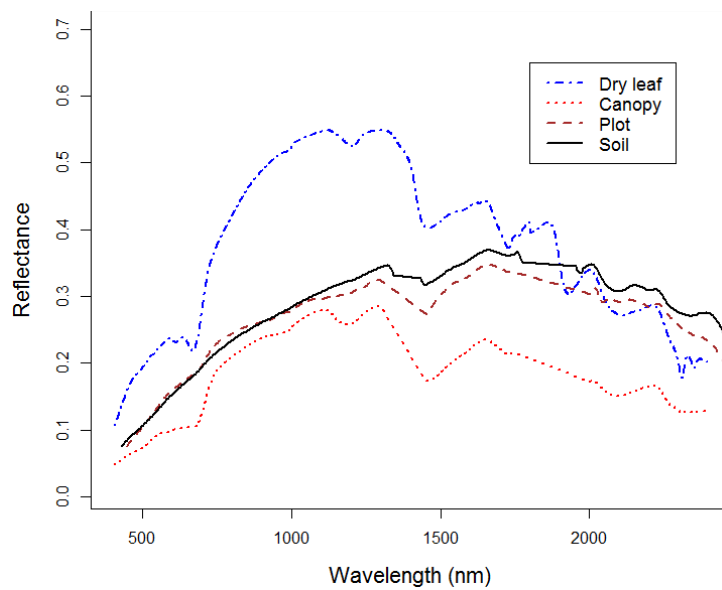


Figure S2. Mean spectra of the dry leaves, canopy and plot-level measurements, and soil.

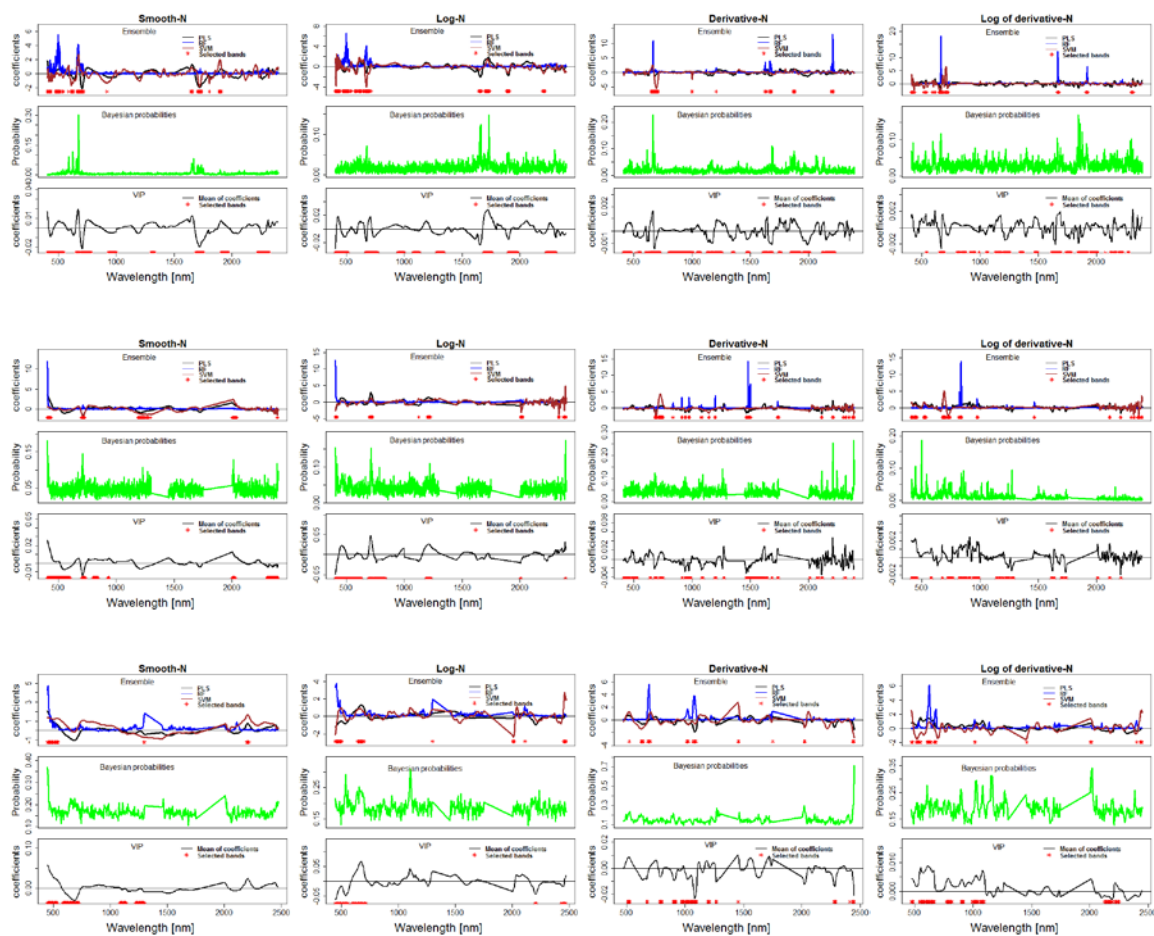


Figure S3. Variable selection for N at leaf (first row), canopy (second row) and plot (third row) scales.

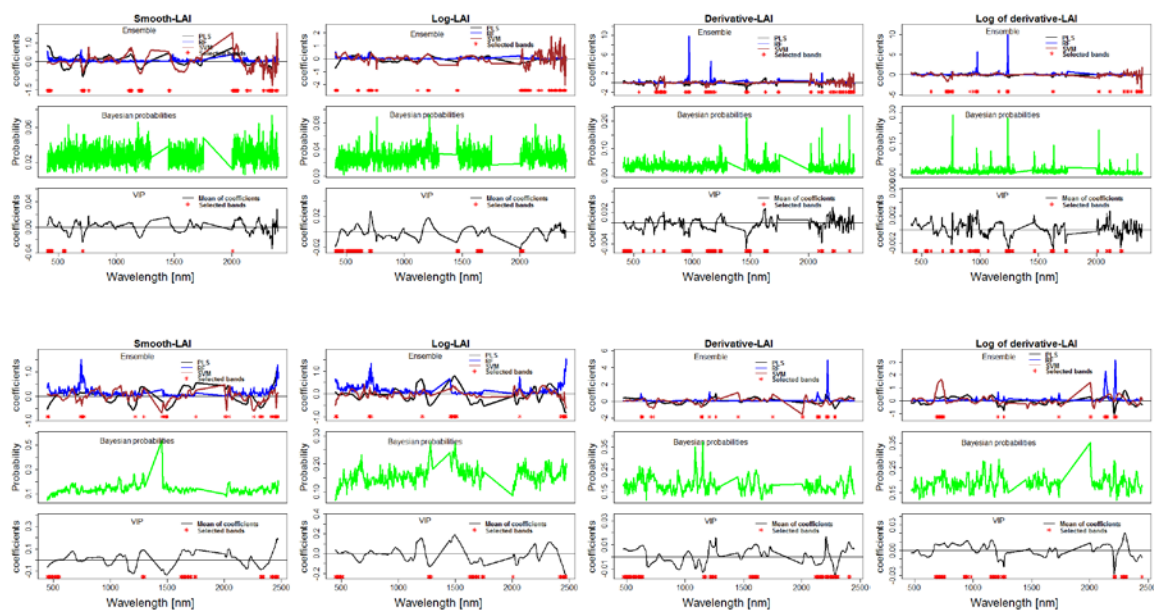


Figure S4. Variable selection for LAI at canopy (first row) and plot (second row) scales.

Table S1. Summary of field data statistics.

Site- year	Time of sampling	AVIRIS-NG acquisition	Number of plots with N measurements	Number of plots with LAI measurements	Mean %N	Std %N	Mean PLA	Std LAI	Mean cover	Std cover
RCEW-2014	Sept - Nov	Sept	20	22	1.70	0.37	1.43	0.51	41.4	16.6
Hollister- 2014	Oct	Sept	16	16	2.01	0.19	0.88	0.28	26.94	9.74
LP-2014	Oct	Nov	10	10	2.16	0.21	2.11	0.27	32.97	12.15
BP-2014	Oct	Sept	22	21	1.66	0.25	1.85	0.30	24.17	16.71
RCEW-2015	May	June	19	26	1.58	0.31	1.41	0.83	25.84	12.12
BoP- 2015	May - June	June	0	19	-----	-----	1.35	0.39	30.56	13.36
LP- 2015	May	June	11	10	2.35	0.25	2.2	0.37	25.78	18.15
BP-2015	May	June	21	23	1.91	0.48	1.84	0.29	31.12	12.10
Total	-----	-----	119	147	1.91	0.29	1.63	0.40	29.54	15.39

Table S2. Comparison of selected bands using Ensemble method and known N absorption bands.

Absorption region ($\pm 40\text{nm}$)	Chemicals	Smoothed	First derivative	Log- transformed	Derivative of log-transformed
430	Chlorophyll-a	✓	×	✓	✓
460	Chlorophyll -b	✓	×	✓	✓
640	Chlorophyll -b	✓	✓	✓	✓
660	Chlorophyll-a	✓	✓	✓	✓
910	Protein	✓	×	×	×
1020	Protein	×	✓	×	×
1510	Protein, nitrogen	×	×	×	
1690	Lignin, starch, protein, nitrogen	✓	✓	✓	✓
1940	Water, lignin, protein, nitrogen, starch, cellulose	✓	×	✓	✓
1980	Protein	×	×	×	×
2060	Protein, nitrogen	×	×	×	×
2130	Protein	×	×	×	×
2180	Protein, nitrogen	×	×	✓	×
2240	Protein	×	×	✓	×
2300	Protein, nitrogen	×	×	×	✓
2350	Cellulose, protein, nitrogen	×	×	×	✓

Table S3. Prediction rate for foliar N at different scales using cross validation.

Scale	Leaf				Canopy				Plot					
	Ensemble		BR		PLS_ref		Ensemble		BR		PLS_ref		Ensemble	
Method	PLS	SVM	RF	Ensemble	PLS	SVM	RF	Ensemble	PLS	SVM	RF	PLS	SVM	RF
Smoothed														
R2	0.63	0.60	0.50	0.63	0.58	0.67	0.71	0.45	0.63	0.62	0.55	0.47	0.52	0.45
CV	16.26	17.79	18.55	15.37	17.09	15.44	14.15	19.13	14.22	16	16.43	16.08	15.63	16.18
Log transformation														
R2	0.60	0.60	0.52	0.59	0.57	0.68	0.69	0.44	0.64	0.63	0.54	0.49	0.52	0.42
CV	16.65	17.21	18.12	15.94	0.17	15.79	15.07	19.40	14.29	15.84	15.62	16.53	15.74	16.87
First derivative														
R2	0.54	0.67	0.69	0.57	0.56	0.59	0.65	0.66	0.60	0.57	0.66	0.45	0.70	0.45
CV	17.71	15.03	14.76	16.38	17.57	16.99	15.58	15.16	15.34	17.18	12.85	16.5	12.47	16.29
Log transformation of first derivative														
R2	0.59	0.72	0.71	0.59	0.57	0.57	0.74	0.70	0.61	0.52	0.58	0.51	0.64	0.46
CV	16.87	14.05	14.03	15.42	17.32	17.54	12.76	14.06	15.06	18.09	14.86	16.03	13.29	16.07

Table S4. Prediction rate for LAI at different scales using cross validation.

Scale	Canopy					Plot				
Method	Ensemble			BR	PLS_ref	Ensemble			BR	PLS_ref
	PLS	SVM	RF			PLS	SVM	RF		
Smoothed										
R2	0.32	0.42	0.13	0.21	0.25	0.39	0.35	0.33	0.34	0.29
CV	34.31	31.85	38.84	34.32	36.20	0.29	32.94	31.61	29.62	0.32
Log transformation										
R2	0.29	0.41	0.13	0.27	0.23	0.35	0.40	0.32	0.41	0.30
CV	35.85	32.51	38.81	33.26	36.55	31.84	31.97	32.68	28.77	32.91
First derivative										
R2	0.33	0.41	0.39	0.38	0.26	0.35	0.42	0.39	0.32	0.34
CV	34.04	31.42	32.50	30.65	35.75	30.29	30.42	29.60	29.98	31.27
Log transformation of first derivative										
R2	0.26	0.48	0.43	0.38	0.27	0.32	0.34	0.37	0.30	0.30
CV	0.35	0.30	31.36	29.91	35.38	33..33	33.09	30.51	30.20	32.34

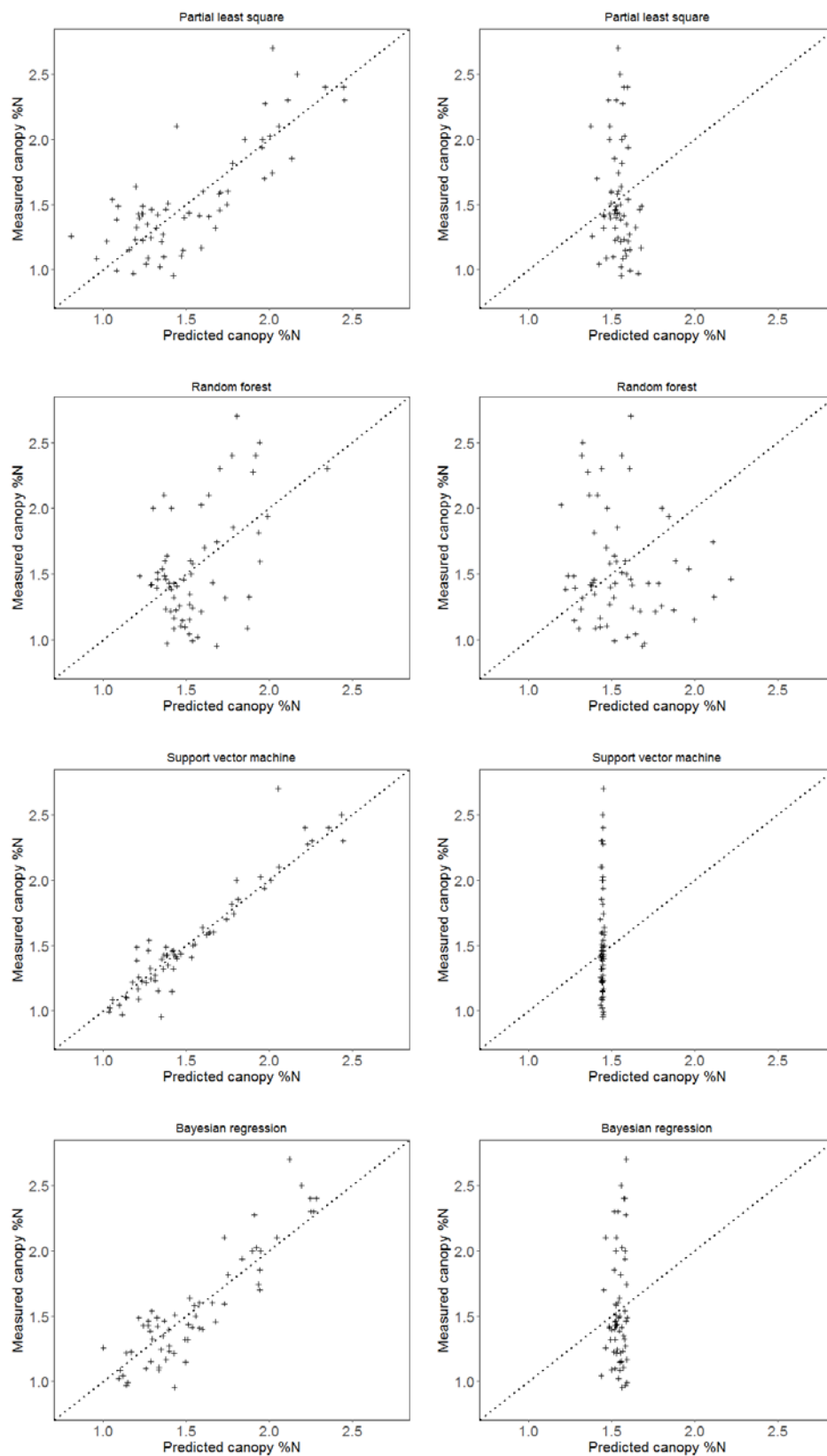


Figure S5. Cross validated predictions before (left column) and after (right column) correction for canopy structure and soil.

Table S5. Cross validation vs leave-one-dataset-out validation.

Plot scale datasets										
Cross validation						Prediction rate on external dataset				
Ensemble			Bayesian	PLS_ref	Ensemble			Bayesian	PLS_ref	
PLS	SVM	RF			PLS	SVM	RF			
BoP-2014										
R2	0.57	0.57	0.53	0.46	0.47	0.32	0	0.05	0	0.33
CV	15.77	15.39	16.01	14.93	16.11	13.97	28.71	34.48	14.09	14.27
B0P-2015										
R2	0.51	0.58	0.62	0.51	0.49	0.43	0.51	0.02	0.37	0.44
CV	14.43	14.67	13.86	13.33	15.06	20.69	19.55	26.16	20.67	0.29
Hol-2014										
R2	0.48	0.60	0.51	0.46	0.42	0.13	0.02	0.12	0	0.15
CV	17.22	15.32	16.61	15.32	17.87	14.43	21.74	12.90	7.90	13.02
LP-2014										
R2	0.42	0.45	0.52	0.42	0.42	0.36	0.43	0.33	0.35	0.36
CV	17.30	17.12	15.79	15.50	16.88	7.86	9.6	8.2	7.71	7.82
LP-2015										
R2	0.43	0.48	0.44	0.37	0.40	0.19	0.04	0	0.09	0.18
CV	16.04	16.61	16.19	15.22	16.59	9.51	14.45	31.75	9.88	9.34
RC-2014										
R2	0.53	0.53	0.54	0.41	0.43	0.56	0.01	0.05	0.47	0.57
CV	15.08	16.76	14.63	14.49	16.03	15.05	24.33	22.47	16.26	15.10
RC-2015										
R2	0.58	0.59	0.55	0.47	0.55	0.15	0.01	0.03	0	0.30
CV	13.63	13.58	14.43	13.38	14.27	27.90	28.64	22.86	25.87	29.61

Additional data sets

- The AVIRIS-NG datasets S1 can be find in (Dashti et al., 2018):
<https://doi.org/10.3334/ORNLDAAAC/1533>
- The field dataset S2 can be find in (Glenn et al., 2017):
<https://doi.org/10.3334/ORNLDAAAC/1503>